PARTICLE EMISSIONS FROM CONSUMER LEVEL 3D PRINTERS

A Dissertation
Presented to
The Academic Faculty

by

Qian Zhang

In Partial Fulfillment
of the Requirements for the Degree
Doctor of Philosophy in the
School of Civil and Environmental Engineering

Georgia Institute of Technology
December 2018

PARTICLE EMISSIONS FROM CONSUMER LEVEL 3D PRINTERS

Approved by:

Dr. Rodney J. Weber, Thesis Advisor
School of Earth & Atmospheric Sciences
Georgia Institute of Technology

Dr. Joe Brown
School of Civil & Environmental Engineering
Georgia Institute of Technology

Dr. Armistead G. Russell, Academic Advisor
School of Civil & Environmental Engineering
Georgia Institute of Technology

Dr. Marilyn S. Black
Chemical Safety
Underwriters Laboratories Inc.

Dr. James A. Mulholland
School of Civil & Environmental Engineering
Georgia Institute of Technology

Date Approved: 10/18/2018

ACKNOWLEDGEMENTS

First, I would like to express my sincere gratitude to my thesis advisor, Dr. Weber, for his guidance and support for my research. I also would like to thank my academic advisor Dr. Russell and the committee members, Dr. Mulholland, Dr. Brown, and Dr. Black, for their suggestion to my research; especially Dr. Black, who has made this project possible and supported me to finish my Ph.D. study. Second, I would like to thank all the collaborators I had worked with, for their expertise and valuable input for my research: Dr. Jenny Wong in Dr. Weber group, Dr. Aika Davis from Underwriters Laboratories Inc., Girish Sharma and Dr. Pratim Biswas from Washington University in St. Louis, and Dr. Michal Pardo and Dr. Yinon Rudich from Weizmann Institute of Science. Third, I would like to thank all the members in Dr. Weber and Dr. Russell groups, for their suggestion on my research and their companions in my daily life. Last but not least, I would like to thank my family and friends, for their support during my doctoral study.

TABLE OF CONTENTS

LIST OF TABLES

LIST OF FIGURES

SUMMARY

As 3D printing technologies becoming popular and available to general public, concerns have been raised on the emissions and potential health impacts of operating 3D printers in indoor environments, such as offices, schools, and residential houses. In this study, a comprehensive research on the particle emissions from consumer level 3D printers was performed. Particle emissions were characterized by applying a standard test method developed for laser printers in an environmental chamber. 3D printer emissions were at comparable level or lower than those from laser printers in general, which varied largely depending on operating conditions. Most of the particles emitted from 3D printers were ultrafine particles in terms of particle number. The factors affecting particle emissions, such as printer brand, print filament material, brand and color, extrusion and build plate temperature, have been systematically investigated. Filament material and extrusion temperature played important roles in particle emissions; acrylonitrile butadiene styrene (ABS) material, which works at a higher extrusion temperature, emitted orders of magnitude more particles than polylactic acid (PLA). In addition, some specific brands of filament emitted much more particles than other brands of the same material in general. To understand particle formation mechanism and contrast emissions associated with different operating conditions, an aerosol dynamic model was used to simulate the steady state particle characteristics during printing. The model was based on the concept that the particles are formed from the gases emitted during the heating of filament, and grow by condensation and coagulation, which happen within a small volume near the extrusion nozzle. This model linked the observed particle concentration

distributions to the model parameters of precursor gas properties, and explained the contrasts among the most important controlling factors. The model results showed the vapor properties differed for different filament brands of ABS, which indicated the particle formation is not associated with ABS polymers, but potentially some additives. Thermophoresis may be a way to remove the newly formed small particles before they are dispersed into surroundings. Particle chemical composition was investigated using both online and offline measurements. The mass spectra of ABS emitted particles were unlike those of the ABS monomers, which was consistent with the model result that the particles are not formed directly from ABS materials, while the mass spectra of PLA emitted particles were similar to the PLA monomer mass spectra. Therefore, the toxicity of particles may not be obtained directly from the raw material and should be investigated separately. Multiple approaches were applied to assess particle toxicity, which included mice exposure, *in vitro* cell viability, cell death type, and intracellular reactive oxygen species (ROS) generation, and a chemical (dithiothreitol, DTT) ROS assay. A consistency among various methods showed that PLA emitted particles induced similar levels of responses at much lower doses than ABS-emitted particles, indicating PLA emitted particles are more toxic on a particle mass basis. However, calculations for the overall exposure showed ABS filaments may be more harmful due to their much higher emissions. Overall, 3D printers are sources of high levels of ultrafine particles, which are potentially harmful for their users. Therefore, the emissions should be regulated and mitigated.

CHAPTER 1. INTRODUCTION

1.1 Fused deposition modeling 3D printers

Three-dimensional (3D) printing (also called additive manufacturing or rapid prototyping) fabricates a product by adding (placing and bonding) layers of material to each other in a predetermined way. The 3D printing technologies can be classified based on the baseline technology or type of raw material input; the most successful commercialized technologies include selective laser sintering (SLS), stereolithography (SLA or SL), and fused deposition modeling (FDM) (Gibson et al. 2010). FDM, also known as fused filament fabrication (FFF), is the most common extrusion-based 3D printing technology. FDM works by heating a filament-shaped thermoplastic material to a semi-liquid state, and then depositing it through an extrusion nozzle onto a moving build place, thus creating a 3D object layer by layer (Bandyopadhyay and Bose 2015). The most commonly used materials are acrylonitrile butadiene styrene (ABS) and polylactic acid (PLA), with various colors; other materials such as nylon, polyethylene terephthalate (PET), high impact polystyrene (HIPS), polypropylene (PP), polycarbonate (PC), and composite materials with metal and wood are also becoming available (Ferdinand et al. 2016; Horvath 2014). The extrusion temperature for various materials ranges from 180 °C to 290 °C; the build plate temperature ranges from room temperature to 110 °C; some printers also require additional adhesion (e.g., tape or glue) on build plates to help mounting the printed layers. ABS is a cost-effective petroleum-based polyamide polymer, which is easy to machine and fabricate, with good resistance to impact and chemicals, excellent machinability, and decent strength and stiffness (Izdebska and Thomas 2016).

PLA operates at a lower extrusion temperature comparing to ABS; it is thermally unstable and not as strong as ABS, but it is compostable and biodegradable, produced from renewable sources (Jamshidian et al. 2010).

3D printers are widely used in various fields, including electronics, medicine and medical sciences, aerospace and defense, automotive and manufacturing industries, consumer products, entertainment and education (Wojtyła et al. 2017; Bandyopadhyay and Bose 2015; Gibson et al. 2010). Unlike industrial-level 3D printers, which are generally large in size, expensive and complex to operate, consumer-level FDM 3D printers are less technologically advanced and easier to operate; in addition, they can be as small as desktop size, affordable and user friendly, thus suitable for entry-level and non-professional users to print 3D objects easily. In addition to the variability of materials and flexibility of custom settings, FDM 3D printers are popular and accessible to the general public. These consumer level FDM 3D printers are mostly found in schools, educational institutions, libraries, design offices and residences (Harrop 2015). Though the working mechanism is the same, the design of printers varies largely. For example, some printers are enclosed while some are not; some printers are capable of printing with multiple materials, or capable of changing settings while some are not.

According to the past experience with photocopiers and laser printers, 3D printers may be potential pollutant sources in indoor environment. Therefore, the application of 3D printers in residences and offices, which are not designed for typical manufacturing, raises concerns of the potential health effects induced by the emissions from 3D printing. Special concern is on the potential health impacts on susceptible population such as children, since FDM 3D printers are widely used in primary schools. Another concern is

the longer-time exposure health impact of individual users and employees, since 3D printing processes usually extend for hours when the operator may stay close to the printer, or the printer may be used frequently.

1.2 3D printer emissions

FDM 3D printing involves heating of thermoplastics. It is known from the commercial extrusion processing of thermoplastics that both particles and volatile organic compounds (VOCs) are emitted (Adams et al. 1999). 3D printing may also emit particle and gas phase pollutants.

A number of studies have reported emissions of particles from consumer level FDM 3D printers using various filament materials. All show significant particle emissions of approximately the same orders of magnitude as other indoor sources, such as laser printers and some cooking processes. The maximum particle number concentrations for ABS material measured during printing ranged from 6×10^3 to 1×10^6 particles/cm^3, with majority of observations in the order of 10^5 particles/cm^3; the particle emission rates for ABS were from 3×10^8 to 2×10^{12} particles/min (Stabile et al. 2017; Zontek et al. 2017; Azimi et al. 2016; Deng et al. 2016; Steinle 2016; Yi et al. 2016; Kim et al. 2015; Stephens et al. 2013). The maximum particle concentrations for PLA materials were from 1×10^3 to 4×10^5 particles/cm^3, with majority of observations in 10^3 to 10^4 particles/cm^3 levels, and the particle emission rates for PLA were 2×10^8 to 4×10^{10} particles/min (Stabile et al. 2017; Zontek et al. 2017; Azimi et al. 2016; Deng et al. 2016; Steinle 2016; Yi et al. 2016; Kim et al. 2015; Stephens et al. 2013). In general, the particle emissions vary within a wide range between different studies, and even within

the same study. However, the overall consistency showed particle emissions from ABS material were generally one to two orders of magnitude higher than those from PLA material. Particle emissions from HIPS and PC materials were at similar levels of the high emitting ABS filaments (Seeger et al. 2018; Azimi et al. 2016). Composite PLA filaments that include wood or copper were found to emit one order of magnitude more particles than pure PLA filaments (Stabile et al. 2017). Emissions from nylon ranged from the levels of average emitting ABS to high emitting ABS (Seeger et al. 2018; Stabile et al. 2017; Azimi et al. 2016). In addition to the different printing conditions like filament material, the reasons for the large variation in particle emissions may also be due to the differences of experimental setup (e.g., chamber versus room environment, air mixing and air exchange rate, measurement instrumentation) and calculation method (e.g. considering particle loss or not). Since the studies were carried out in various ways, the comparison between studies were only on the scale of orders of magnitude. In addition, the existing studies haven't done a systematic characterization on potential affecting factors (e.g. printing conditions like filament material, filament brand, printer brand).

Some research on the properties of the emitted particles have been carried out. The mean sizes of the emitted particles were generally smaller than 100 nm (ultrafine particles) for ABS and PLA filaments (Steinle 2016; Kim et al. 2015), with some ABS and nylon filaments emitting both large amount of ultrafine and fine particles (Seeger et al. 2018). Microscopy analyses showed that individual particles were amorphous but close to spheres, which also could form agglomerates (Zontek et al. 2017; Steinle 2016). The chemical composition of the particles are complex and not clearly known. Carbon and oxygen were the most abundant elements in ABS and PLA emitted particles (Zontek

et al. 2017). Metals like Na, Cu, Cr and Fe were also detected, but were only qualitatively detected or at very low concentrations (Stefaniak et al. 2017b; Steinle 2016). Moreover, the Raman spectra showed that the composition of particles and the corresponding raw filament materials were not alike (Vance et al. 2017). However, the link of particle compositions to particle and VOC emissions was not established, and the mechanism of particle formation has not been systmetically studied.

Various VOC species have also been detected during 3D printing, but the VOC emissions also subject to the variations in experimental setup and measuring methods. Generally considering major emissions, ABS filaments emitted styrene and ethylbenzene, PLA filaments emitted lactide, lactic acid and methyl-methacrylate, and nylon filaments emitted caprolactam (Azimi et al. 2016; Steinle 2016). The total VOC (TVOC, toluene equivalent) emission rates for ABS were 0.6×10^3 to 3.9×10^3 μg/h, for PLA were 0.4×10^3 to 3.6×10^3 μg/h, and the TVOC emission rates for ABS were always higher than those of PLA filaments within the same study (i.e., same experimental setup and method) (Floyd et al. 2017; Azimi et al. 2016; Steinle 2016). TVOC emission rates for HIPS were generally smaller than those of ABS; TVOC emission rates for nylon can range from similar levels of ABS emission rates to 4 times of ABS emission rates (Floyd et al. 2017; Azimi et al. 2016). The VOC and TVOC emission rates ranged largely due to the differences in measurement and calculation methods. Chamber experiments showed that TVOC emission rates for various ABS and PLA filaments operating on 3D printers were lower than those for laser printers (Stefaniak et al. 2017b). However, the finished print objects were found to off-gas VOCs; acetaldehyde and styrene emissions were detected from object printed using ABS (Stefaniak et al. 2017b). Other gases like ozone and

carbon monoxide, nitrogen dioxide, and ammonia were also monitered in chamber studies during 3D printing, while no emission of those species were detected (Stefaniak et al. 2017b; Steinle 2016).

1.3 Potential health impacts of emissions

People in developed countries spend over 80% of their time in indoor environments (e.g., homes, offices, schools, etc.) (Schweizer et al. 2007; Klepeis et al. 2001), thus indoor air quality is important for human health. The adverse health effects induced from poor indoor air quality include sick building syndrome (i.e., temporary eye, nose or throat irritation, skin irritation, cough, wheeze, headache, and fatigue), allergies, asthma, and risk of cancers or other serious respiratory diseases (Hedge 2009). Typical indoor air pollutants include carbon dioxide, carbon monoxide, nitrogen oxides, sulfur oxides, ozone, carbonyls (formaldehyde and acetaldehyde), VOCs and particulates, exposures to which can be via inhalation, ingestion and surface contact (Hedge 2009). Among those concerned pollutants, aldehydes, VOCs and particles have been observed as major emissions from FDM 3D printers.

VOCs are the most prevalent indoor air pollutants, which comprise a large number of compounds. Exposure to VOCs and aldehydes may lead to acute and chronic respiratory effects, neurological toxicity, irritation of eyes, throats and mucous membranes, and lung cancer (Guo et al. 2004; Godish 2001; Tucker 2001; Wallace 2001), especially for young children (Rumchev 2004). Acetaldehyde, benzene, ethylbenzene, formaldehyde, hexane, styrene, toluene, which has been detected during 3D printing (Stefaniak et al. 2017b; Floyd et al. 2017; Azimi et al. 2016), have been listed

as hazardous air pollutants (HAP) by U.S. Environmental Protection Agency (EPA), the concentrations of which could be much higher indoor than outdoor given specific pollutant sources (U.S. EPA 2000). Model analysis showed that some VOC concentrations during 3D printing for high emitting cases can exceed recommended exposure limits in an office environment (Azimi et al. 2017). However, due to the differences of indoor environment (e.g., heating, ventilation, and air conditioning (HVAC) setting, loss to walls), the overall VOC exposure might be at low-levels comparing to some non-regulate guidances (Stefaniak et al. 2017a).

Studies have shown high particle emissions from various indoor sources like laser printers, cooking, burning candles, etc. (Scungio et al. 2017; Bekö et al. 2013; Géhin et al. 2008; He et al. 2007), thus their potential health impacts are gaining more concerns. In addition, both ambient particulate matters (PM) and engineered nanoparticles (NP, less than 100 nm in size) are known to have detrimental health effects based on toxicological and epidemiologic studies (Li et al. 2015, 2016; Costa et al. 2014; Lee et al. 2014). The toxicity of particle emissions from consumer 3D printers is unknown, but of significant concern. Similar to emissions from 3D printing, pyrolysis of high molecular weight polymers is found to emit both gases and particles (Seidel et al. 1991). Studies have shown that inhaling fumes from heated polytetrafluoroethylene will cause extremely high pulmonary toxicity and mortality in rats, and the emitted ultrafine particles were believed to play a crucial role (Oberdörster et al. 2000; Lee and Seidel 1991; Warheit et al. 1990). The toxicity of ultrafine particles is due to their distinct properties of high mobility and large surface areas (Li et al. 2016). They are capable of depositing in all regions of the respiratory tract and can be translocated through the bloodstream to various organs, and

even enter cells and damage organelles (Grass et al. 2010; Li et al. 2003). Therefore, exposures to particles are found to be associated with inflammation (Pardo et al. 2015, 2016), cell death (Peixoto et al. 2017; Deng et al. 2014), and diseases (Collaborators 2016; Brook et al. 2010). In addition, the bulk components comprising ultrafine particles may not be toxic, but the particles may serve as a means to transport hazardous materials adsorbed on their surfaces (Li et al. 2016; Grass et al. 2010; Oberdörster et al. 2005; Salvi and Holgate 1999). Ultrafine particles have been found to be more toxic than larger-sized particles of the same material and dose (Zhang et al. 2003; Donaldson et al. 1998; Oberdörster et al. 1994), and have been shown to induce inflammation and oxidative stress (Hussain et al. 2009; Nel et al. 2006; Li et al. 2003).

A survey on 3D printer users showed induction of high rates of respiratory symptoms (Chan et al. 2017). A personal case study showed redevelopment of asthma when using 3D printers (House et al. 2017). Endothelium-dependent arteriolar dilation impairment was found in rats after exposure by inhalation to 3D printer emissions (Stefaniak et al. 2017a). However, a human exposure study showed no acute inflammatory effect of FDM 3D printing with ABS or PLA materials (Gümperlein et al. 2018). The inconsistency of toxicity results was also found for particles emitted from photocopiers and laser printers. For example, no acute or clinically relevant alterations was found after a single high-level exposure to laser printer emissions (Karrasch et al. 2017), while Pirela et al. (2013, 2016) and Khatri et al. (2013a, 2013b) found particles emitted from laser printers and photocopiers were deleterious to human cell lines, mice and human subjects. Therefore, the toxicity assessment results largely depend on particle properties, experimental subject (e.g. human, animals, or cells), assessing method (e.g. *in*

vivo or *in vitro*, various biomarkers and mechanisms), exposure time and dose (e.g. single exposure versus repetitive exposure) (Johnston et al. 2010b, 2010a; Kroll et al. 2009; Sayes et al. 2007). The existing results revealed the pontential health effects for 3D printer emissions, while more toxicity assessments using multiple methods need to be applied and compared in order to have a broader understanding of the particle emission toxicity.

1.4 Objectives

Though previous studies show emissions of ultrafine and fine particles from consumer level FDM 3D printers, a standard testing and evaluating method is lacking, but essential to understand how printer operation variables drive particle emission and evolution, and to quantitatively compare results between investigations. In this study, we follow an established test protocol developed for characterizing laser printer emissions (BAM 2012), which allows comparison of 3D printer emissions to those of laser printers. Using this method, printer operating conditions, including printer brand, filament material, brand and color, extrusion and built plate temperature, are tested in a systematic manner. Applying an existing test method to 3D printers gives insight for development of a standard test method for 3D printers and provides a database for assessing emission limits. Furthermore, it might provide insights for 3D printer and filament manufacturers to produce low emitting products and develop effective mitigation methods. This part of the work is covered in Chapter 2 of this thesis.

The aerosol dynamic processes leading to the particle formation and the evolution of the particle size distributions observed from FDM 3D printing have never been

systematically investigated, which is important to gain an understanding the properties of emitted particles, and potential mitigation methods. We apply a method of moments aerosol model to simulate steady state particle concentrations recorded during printing, and perform a sensitivity analysis to investigate how model parameters affect the number and size distribution of the emitted particles. In addition, the effects of extrusion nozzle temperature, filament brand, and type of filament material are discussed with association to the model parameters. The model provides conceptual insights on processes and factors leading to particle emissions from FDM 3D printers and points to possible mitigation approaches. This part is discussed in Chapter 3.

The chemical composition and potential toxicity of particles emitted from FDM 3D printers have not been investigated in detail. We analyze the chemical composition of particles emitted from various printing filaments via different methods, and compare it to that of the raw filament materials. Knowing the chemical composition of the particles will help understanding the potential toxicity of them. We further explore the potential toxicity of particles using multiple methods commonly used for particle toxicity assessment, including *in vivo* animal exposure, various *in vitro* cellular assays and a chemical cell-free assay. This part of study provides a comprehensive understanding of 3D printer emitted particle properties and toxicity, by comparing between emissions from different filaments, and by contrasting to toxicity results of ambient aerosol health studies. These topics are presented in Chapter 4.

CHAPTER 2. CHARACTERIZATION OF PARTICLE EMISSIONS FROM CONSUMER FUSED DEPOSITION MODELING 3D PRINTERS

Qian Zhang, Jenny P. S. Wong, Aika Y. Davis, Marilyn S. Black, Rodney J. Weber

Aerosol Sci. Technol. 51(11): 1275-1286. 2017

DOI: 10.1080/02786826.2017.1342029

2.1 Abstract

Particle emissions from multiple fused deposition modeling consumer 3D printers were systematically quantified utilizing an established emission testing protocol (Blue Angel) to allow quantitative exposure assessments for printers operating in different environments. The data are consistent with particle generation from volatilization of the polymer filament as it is heated by the extruder. Typically, as printing begins, a burst of new particle formation leads to the smallest sizes and maximum number concentrations produced throughout the print job. For acrylonitrile butadiene styrene (ABS) filaments, instantaneous concentrations were up to 10^6 #/cm^3 with mean particle sizes of 20 to 40 nm when measured in a well mixed 1 m^3 chamber with 1 air change per hour. Particles are continuously formed during printing and the size distribution evolves consistent with vapor condensation and particle coagulation. Particles emitted per mass of filament consumed (particle yield) varied widely due to factors including printer brand, and type and brand of filament. Higher extruder temperatures result in larger emissions. For

filament materials tested, average particle number yields ranged from 7.3×10^8 to 5.2×10^{10} g^{-1} (approximately 0.65 to 24 ppm), with trace additives apparently driving the large variations. Nanoparticles (diameters less than 100 nm) dominate number distributions, whereas diameters in the range of 200 to 500 nm contribute most to estimated mass. Because 3D printers are often used in public spaces and personal residences, the general public and particularly susceptible populations, such as children, can be exposed to high concentrations of non-engineered nanoparticles of potential toxicity.

2.2 Introduction

The 3D printer market is estimated to have a compounded annual growth rate of 44% (Alto 2015). Among diverse 3D printers on the market, fused deposition modeling (FDM) printers, which heat a filament to semi-liquid state and deposit it to build a 3-dimensional object by layers (Zukas and Zukas 2015) are relatively inexpensive and convenient to use, making them accessible to the general public. The most commonly used filament materials are thermoplastics like acrylonitrile butadiene styrene (ABS) and polylactic acid (PLA) (Ragan 2013). Other types are continuingly becoming available, including polyamide (nylon) and polyethylene terephthalate (PET) (MatterHackers 2015). Desktop sized 3D printers in particular, are often used in educational institutions, public spaces such as libraries, design offices and within homes (Harrop 2015). It is known that the commercial extrusion processing of thermoplastics emits both particles and volatile organic compounds (VOCs) (Adams et al. 1999), and some of the thermal decomposition products are recognized to be toxic (Unwin et al. 2013; Rutkowski and Levin 1986). It follows that FDM 3D printers are potentially hazardous to operate in certain indoor environments. Due to the increasing usage of 3D printers, and past

experience with laser printer emissions, characterization of 3D printer emissions is necessary to assess human exposure and potential health impacts.

A number of studies have investigated particle emissions from consumer FDM 3D printers using multiple filament materials. All show significant emissions of approximate same order of magnitude to other indoor sources, such as laser printers and some cooking processes. A detailed review of nine previous studies is provided in Section 2.7.1 including a summary on their conditions and results (Table 2.2).

Although there is some consistency between studies, comparing particle emissions reported, and factors associated with these emissions, is difficult because no standard testing protocol has been utilized. For example, different testing environments were used, including chambers versus actual workspaces of different dimensions and air supply rates, resulting in different air exchange rates (ACH) and degrees of mixing, all of which can have an effect on the measured emissions. Furthermore, different emission analysis methods have been employed, such as assuming a steady state mass balance, a dynamic mass balance or utilizing a simple box model. Some considered particle losses to surfaces (chamber walls), while others did not. Differing parameters were also used to summarize emissions, such as average or median particle emission rates, which depended on calculation methods and were normalized to print time, mass or length of filament used, and peak or average particle concentrations. Finally, differences in monitoring instrumentation can also limit comparisons since particle size ranges measured also varied. Though all studies show emissions of non-engineered nanoparticles from consumer FDM 3D printers, a standard testing and evaluating method is essential to understand how printer operation variables drive particle emission and evolution, and to

quantitatively compare results between investigators. In this study, we follow the established test protocol developed for characterizing laser printer emissions (BAM 2012), which also allows direct comparison of consumer 3D printer emissions to those of laser printers. Using this method, printer operating conditions, including printer brand, filament type, brand and color, extruder and build plate temperature, were tested in a systematic manner.

2.3 Materials and Methods

2.3.1 Printers and materials tested

Six commercially popular FDM 3D printer brands were tested, referred to as *A* through *F*; their differing properties, including extruder temperature, build plate and configuration design, are listed in . Three kinds of widely used filament materials were tested: ABS, PLA and nylon, all with a diameter of 1.75 mm. Filament material densities were taken to be 1.07 g/cm^3 for ABS, 1.22 g/cm^3 for PLA and 1.13 g/cm^3 for nylon, according to manufacturer Material Safety Data Sheets. Filaments were acquired from differing manufacturers (i.e., sellers) since subtle differences in minor constituents or additives that can vary by manufacturers, but go unreported, may have large effect on emissions. Filament brands are referred to as *a* through *j*. In order to assess the influence of printing conditions on emission, experiments were designed to vary one variable at a time and mainly done on printer *A*, *B*, *C* with filament brand *a* through *e*, which led to 52 combinations of printer brand, filament material, filament brand, filament color and extruder temperature; the rest of the printers and filaments tested were included when comparing overall emissions. Additionally, a set of different objects was printed,

resulting in various print times due to differing object size and shape, filament feed rate and object support setting. Details of all printing combinations tested are shown in Table 2.3.

Table 2.1 Specifications of printers tested in this study.

Printer brand	Extruder temperature (°C)			Build plate	Appearance	
	ABS	PLA	Nylon		Sidewall	Ceiling
A	270	210	243	Heat[a]	No	No
B	n/a	215	n/a	Tape	4	No
C	260	230	n/a	Glue	2	Yes
D	n/a	215	n/a	Tape	1	No
E	230	n/a	n/a	Tape/Heat (110°C)	4	Yes
F	270	210	n/a	Heata	4	Yes

[a] 100 °C for ABS and nylon; 50 °C for PLA

2.3.2 Environmental chamber

A 1 m^3 environmental chamber (1 × 1 × 1 m) of polished stainless steel interior and thermally insulated walls was used in all experiments; it is designed and evaluated following ASTM standard D6670 guidance (ASTM 2013), UL GREENGUARD Certification (UL 2014) and ECMA-328 (ECMA 2015). It is utilized to determine emissions from laser printers following the Blue Angel Method (BAM 2012), which was developed to test the emissions from office equipment with printing functions. Airflow entered and exited the chamber through two stainless steel air distribution manifolds, aerodynamically designed to provide well-mixed conditions inside the chamber. A clean air supply system delivered 16.7 L/min of dried room air free of VOCs and particles via a gas absorption tower and a HEPA filter, resulting in an ACH of 1 hr^{-1}, as recommended

in the Blue Angel Method (BAM 2012). The temperature and relative humidity (RH) inside the chamber were continuously monitored; all experiments were done under dry conditions (RH = 3.0% ± 0.2%) and at near room temperatures (23 ± 1 °C). During experiments, the printer was placed in the middle of the chamber; particle and VOC sampling tubes were connected through sealable sampling ports on the walls and the ceiling of the chamber that extended approximately 10 cm away from the chamber walls and 10 – 20 cm from the printer. (VOC results are not presented in this paper.) All particle sampling lines were conductive (stainless steel or conductive silicon) to minimize electrostatic particle losses. Power and printer control wires were also passed through sealed ports.

2.3.3 Particle measurement instrumentation

Particles were measured online using three instruments. A condensation particle counter (CPC, TSI) measured total number of particles with diameter larger than nominally 7 nm to larger than 3 μm; a scanning mobility particle sizer (SMPS, TSI) spectrometer measured number distributions for particle electrical mobility diameter between 7 and 300 nm and an optical particle counter (OPC, TSI) measured particle number distributions for particle optical diameter of 300 nm to 25 μm. Instrument specifications are shown in Table 2.4. Factory calibrations for inferring particle size from light scattering are used for the OPC. Particle surface area and volume concentrations were calculated from the measured number distributions assuming spherical particles, and mass estimated using the densities of bulk filament materials. Consistency between the CPCs was tested on 3D printer generated particles prior to the printing experiments, see Section 2.7.2 and Figure 2.11. It is noted that both the inferences of particle size by

the SMPS and OPC, and the conversion of number distributions to surface area and mass distributions rely on assuming the particles are spherical. Imaging of 3D printer particles, however, showed this is not the case (Zontek et al. 2017; Steinle 2016). The spherical particle assumption will lead to uncertainties in our analysis, we estimated the particle diameter determined from the SMPS may be biased high by at most 20%, surface area biased low by 30% and mass biased high by 40%. (See Section 2.7.5).

2.3.4 Test protocol

Tests were carried out following the procedures described in BAM (BAM 2012). Before every experiment, the printer to be tested was prepared inside the chamber and then the chamber continuously flushed with clean air to achieve a background total particle concentration below 5 cm^{-3} (CPC) and total mass concentration below 1 $\mu g/m^3$ (SMPS and OPC). To begin the test, particle measurements were started at least 15 min before print started. Before extrusion, a few minutes were required for the printers to initiate (transfer file, find position and heat extruder and build plate if needed), which varied for different printers. Few particles were generated during this process. The printing period discussed hereafter is the time between when extrusion started and then stopped. The particle measurements continued after the print had stopped for at least 2-hrs, or until concentrations returned to near-background level so that wall losses could be inferred.

2.3.5 Data analysis methods

The data analysis methods follow (BAM 2012) based on the sections discussing fine and ultrafine (nanoparticle) particle measurements in emission test chambers. All

calculation methods were applied in the same way for particle number, surface area and mass concentrations. This provides a proven and standardized method for analyzing and reporting emissions, consistent with those used for laser printer emissions (Koivisto et al. 2010; Schripp et al. 2008). Particle emission rates (*PERs*) as a function of print time and total particle emissions (*TP*) from the complete print job were calculated, considering particle losses to surfaces. Details of the calculation methods are provided in Section 2.7.5), along with the statistical methods used to examine the quality of experimental data and to interpret the results.

In addition to these variables, particle yield was developed specifically for 3D printers to evaluate the particle emissions from a specific printer and filament combination. It is defined as the total particles (*TP*) emitted for a given print job, divided by the printed object mass, including object supports (i.e., the mass of filament used for the complete print job). This definition was applied to particle number, surface area and mass emissions.

2.4 Results and Discussion

2.4.1 Particle concentration and size distribution time series and aerosol dynamic processes

In the following analysis we interpret the evolution of the aerosols measured in the chamber as a function of time in terms of known processes expected to be occurring (Figure 2.1). Aerosol dynamic model simulations are needed to actually quantify these processes, but beyond the scope of this paper.

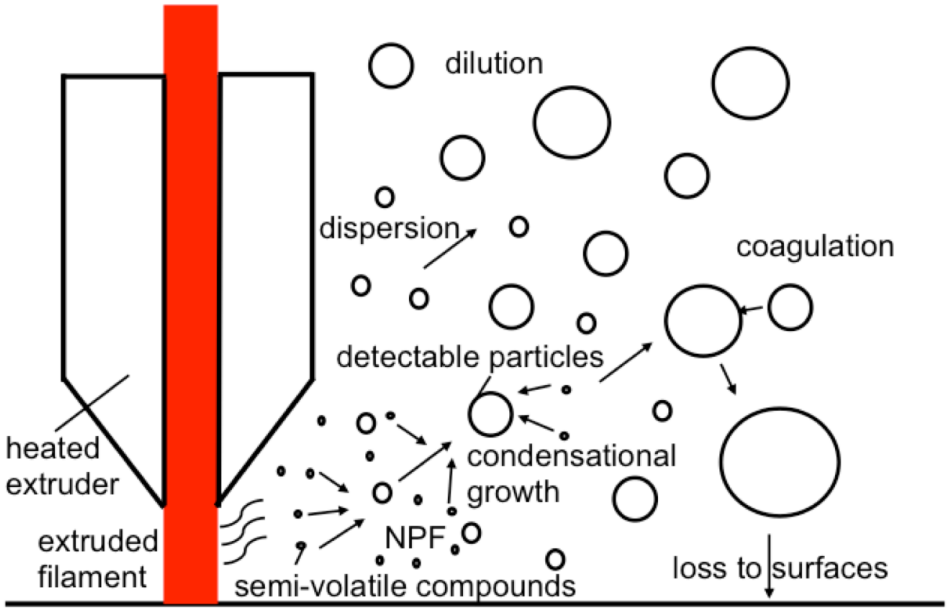

Figure 2.1 Schematic of particle formation, growth and loss processes. NPF is new particle formation resulting from nucleation of emitted semi-volatile vapors.

2.4.1.1 Particle number concentrations

A common feature of 3D printer particle emission profiles is a large jump in number concentrations at the start of the print job, which are typically the maximum number concentrations observed over the entire printing process (Azimi et al. 2016; Steinle 2016; Yi et al. 2016; Kim et al. 2015). This is consistent with new particles generated in the vicinity of the extrusion nozzle due to high concentrations of semi-volatile compounds (SVCs) emitted from the heated filament, which may include semi-volatile organic compounds and other species associated with the bulk filament or additives. Since the concentration of pre-existing particles at the beginning of the process is low (i.e., background room or chamber concentrations) relative to after the printer has been in operation for a period of time, loss of the SVCs by condensation onto pre-existing particles will be low and so these vapor concentrations increase to a point where new

particle formation (NPF) can occur at substantial rates (Figure 2.1). Once formed, these particles rapidly grow and reach detectable sizes (D_p > 7 nm). We have confirmed that this occurred when the printer was operated with ABS with particle-free air introduced into the chamber, or when typical room-air background levels are present at the beginning of the print job (Figure 2.12).

Figure 2.2 and Figure 2.3 show typical print runs using ABS filament for two print job times. Almost immediately once extrusion started, the total particle number concentration and the concentration for 7 – 50 nm particles reach a maximum of about 3.4×10^5 #/cm^3 (Figure 2.2a and b). As more particles are formed and grow, their surfaces can provide an increasing sink for SVCs, lowering the vapor concentrations. This is expected to happen fairly rapidly, (e.g., ~ 5 minutes following the start of extrusion, based on the data) and likely leads to a reduction in NPF, observed as a drop from the initial peak concentrations for the smallest measured particles (Figure 2.2a). As semi-volatile vapors continued to be emitted during printing, NPF is expected to still occur, but at a reduced level since vapors are continuously being scavenged through condensation. Note that not all printers have the same temporal trend as shown in Figure 2.2. An example of a different time series trend for ABS observed can be found in Figure 2.14. The causes of more random concentration variations over the print period are not fully known, but appear to be related to the design of the printer (e.g., open versus closed, etc.).

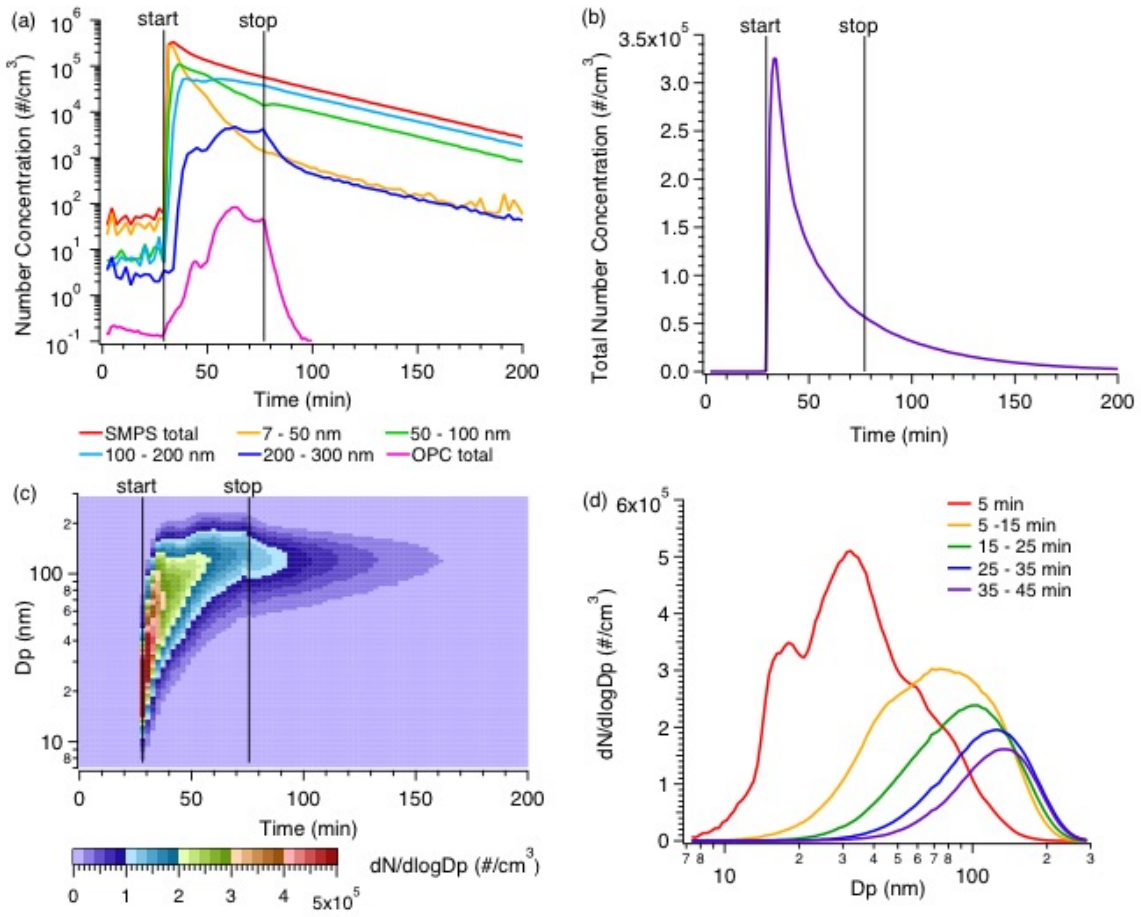

Figure 2.2 Time series of particle number concentrations averaged over various particle size ranges on log scale (a), total particle concentrations on linear scale (b), evolution of size distributions (c) and average particle number distributions during the printing period separated into 5 time intervals (d). The print condition was ABS filament brand *a*, red color, using printer *A*; the printing period was 47 min, identified by the vertical lines.

Ultrafine or nanoparticles (D_p < 100 nm) dominate the number distributions (90%), but their concentrations decrease rapidly during the printing period, especially for 7 – 50 nm particles, whereas larger particles (D_p > 100 nm) gradually increase in concentration (Figure 2.2a). Semi-volatile compounds are expected to be continuously generated from the heated filament at the extruder nozzle or recently deposited filament as printing proceeds, and the new sub-50 nm particles formed at the beginning continue

to grow by vapor condensation. A delay is observed in the appearance of larger particles due to the time needed for particle growth (Figure 2.2a and c). In addition, as number concentrations and particle sizes increase, particle coagulation is expected to become more prevalent. This is also seen in the size distributions in Figure 2.2c and d, where the particle number distributions shift to larger size over time, and the shape of the size distribution in Figure 2.2c resembles the classic banana shape of nucleation-growth-coagulation seen in the ambient atmosphere (Curtius 2006).

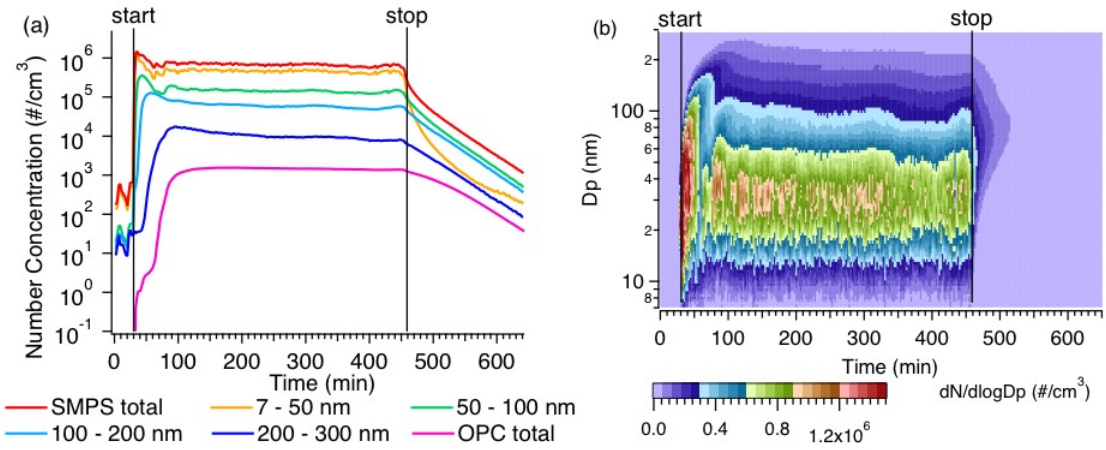

Figure 2.3 Long time print job time series of particle number concentrations (a) and size distributions (b) for ABS filament, brand *d*, green color, on printer *A*; the printing period was 7 hr 4 min, identified by the vertical lines.

While particle formation and growth processes are occurring, due to dilution by continuous clean air exchange, the particles are dispersing as air parcels move away from the extruder; in addition to losses of some fraction of particles to the printer surfaces and the chamber walls, a decay in concentrations in the overall chamber is observed. When the printing job ends, with no source of condensable-vapors, these processes are especially evident as an exponential decay in concentrations toward background levels present before the print started (Figure 2.2 and Figure 2.3).

For shorter print jobs (Figure 2.2), these aerosol dynamic processes may never reach steady state before printing ends, whereas for longer jobs (Figure 2.3), concentrations of various sizes can remain relatively constant after about 1 hr of printing (for this condition), indicating the processes of particle formation, vapor-condensational growth, coagulation and loss reach a steady state. Maximum particle concentrations and the steady state concentrations vary from case to case. Furthermore, the ACH of the testing environment, or forced air cooling by the nozzle, can affect the particle dynamics as the vapors and newly formed particles move away from the extruder nozzle region, changing the relative rates of NPF, condensation, coagulation and loss, in turn affecting particle final sizes and number concentrations.

Most PLA filament runs showed similar concentration profiles as in Figure 2.2, however, the steady state condition (e.g., Figure 2.3) was seldom observed, probably because PLA emitted less SVCs, resulting in lower NPF and growth rates. Thus fewer particles accumulate in a continuously diluting environment and particle concentrations gradually decrease. For some PLA cases, the maximum particle number concentrations were not observed at the beginning of the print, but 10 to 60 min after print started. The difference is likely due to the amount of SVCs emitted near the extruder nozzle and newly-deposited filament (note, emissions from the heated build plate will be discussed below). With much lower condensable SVC concentrations emitted from PLA, it takes longer for the NPF and growth processes to occur and longer times for particles to accumulate. Example time series plots for PLA are shown in Figure 2.15 and Figure 2.16.

Pre-existing room air particles have an effect on PLA aerosol production. When there was a relatively high initial background concentration (~ 10^4 #/cm^3), the pre-

existing particles provided enough surfaces for vapors to condense on, instead of forming new particles. This led to no increase in number concentrations observed throughout the print job, but an increase in mass concentrations (Figure 2.13).

2.4.1.2 Particle surface and mass concentrations

Evolution of the particle surface area and mass concentration distributions for the shorter print run in Figure 2.2 are shown in Figure 2.4. (Plots of surface area and mass concentration time series and size distributions with more details are in Figure 2.17and Figure 2.18). Compared to number concentration profiles, the surface area and mass concentrations both take longer to reach a maximum. The large number of newly formed particles contributes little to surface area or mass, but as printing continues to supply vapors, particle growth by condensation of vapors leads to a rise in surface area and mass concentrations (Note, this also corresponds to a loss in the smallest particle numbers in Figure 2.2a). Near the beginning of the print, nanoparticles (D_p < 100 nm) contributed less than 50% to the total surface area and mass concentrations, and decreased quickly. Instead, 100 – 200 nm particles dominated the surface area concentrations, while for mass slightly larger (D_p ~ 200 nm); particles larger than 300 nm (OPC data) contributed less than 1% to overall surface area and mass due to their low concentrations in this case (Figure 2.17). For longer print times (Figure 2.18), larger particles (D_p > 300 nm, OPC data) contribute more to the overall surface area and mass of emitted particles (~ 6% for surface and ~ 23% for mass), since there is sufficient time for the particles to substantially grow.

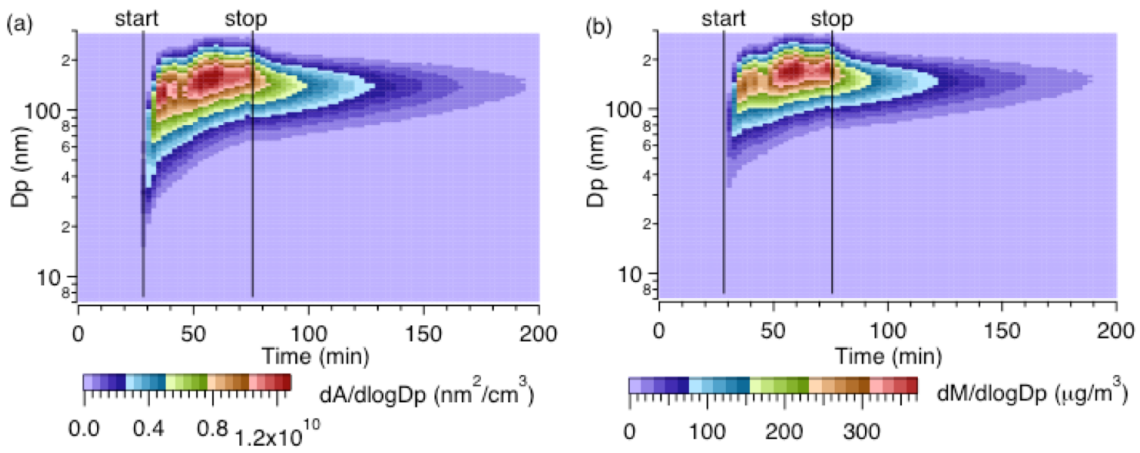

Figure 2.4 Evolution of particle surface area (a) and mass (b) distributions, calculated from number distributions shown in Figure 2.2, assuming spherical particles and a density of 1.07 g/cm^3 (bulk ABS).

It is noteworthy that number distributions have a very different behavior compared to surface area and mass. These differences matter depending on how particle toxicity is viewed, whether it depends on number, surface area or mass concentration.

2.4.2 Emissions as a function of print object and overall particle yields

Three different objects taking approximately 1 hr, 4 hr and 7 hr to print were investigated using the same filament, printer and settings. The particle emissions (*TP*) segregated by different sizes are shown in Figure 2.5. The total number emissions were 1.3×10^{12}, 6×10^{12} and 1.1×10^{13} particles and the total mass emissions were 3.4×10^{2}, 1.6×10^{3} and 2.8×10^{3} μg, respectively. Regarding particle number emissions (Figure 2.5a), about 70% was from particles less than 50 nm and more than 90% was from particles less than 100 nm, consistent with Kim et al. (2015); whereas for mass emissions (Figure 2.5c), more than 80% of the emissions came from particles larger than 100 nm. More than 60% of surface area emissions was from 50 – 200 nm particles (Figure 2.5b),

between number and mass-dominant sizes. Detailed overall emissions from a print job as a function of particle size are shown in Figure 2.19. Ratios of particle emissions separated by size over the total emissions were relatively constant (Figure 2.5), especially comparing between longer print times when aerosol dynamic processes reach steady state.

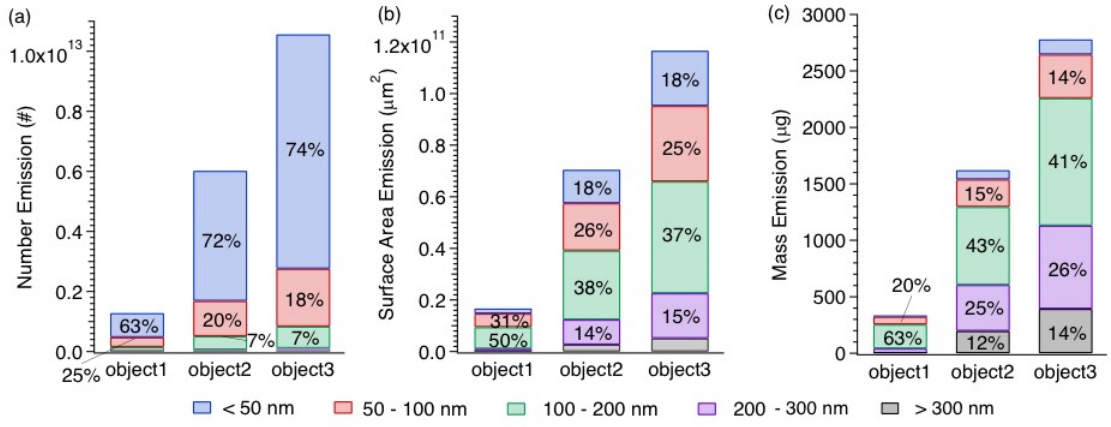

Figure 2.5 Particle number (a), surface area (b) and mass (c) emissions for ABS filament *d* green color on printer *A* for 3 objects taking about 1 hr, 4 hr and 7 hr to print. Each bar indicates the emission (*TP*) from one print object; colors indicate different particle size ranges. Values on the colored bars are the ratios of emissions from such particle size range over total emissions.

To explore the relationship between overall emission and print object further, 11 objects of different sizes and shapes were printed. Object mass varied from 6 g to more than 130 g, corresponding to number emissions from approximately 10^{11} to 10^{13} particles. A fairly linear relationship between total particle emissions and print object mass was observed (Figure 2.20), with the small amount of variability due to print object shape. The slope of the regression fit gives the yield; total particle emission from printing an object over mass of filament consumed, or mass of printed object. To simplify the determination of yields, in the following we estimate yields from each print job by the

ratio of *TP* over object mass. Ratios give fairly similar yields to those calculated by slopes, with uncertainty below 20%.

One could also use print time to determine yield (*TP/time*, i.e. emission rate), which is related to yield normalized by object mass depending on filament feed rate. However, this might lead to some uncertainties since for a similar object mass, different printers have different filament feed rates. Also a more complex object can take longer time to print than a simpler one. In these cases, yields normalized to print time will underestimate emissions. Because of these issues, in this study, all emissions were normalized to object mass. Yields can also be determined for any particle size range and emission parameter. Once the yield has been established for a given printer-filament combination, it can be used to estimate overall emissions for any object printed under that condition. Specific parameters that affect 3D printer particle yields are now compared.

2.4.3 Factors that may influence particle emissions

Filament color, filament brand, printer brand and filament material may affect particle emissions. Detailed results of all these various comparisons can be found in Section 2.7.10, here we provide a summary of findings.

Experiments were designed to investigate the factors controlling particle emissions, including printer brand (*A, B, C*), filament brand (*a, b, c, d, f*) and filament color (red and white). For ABS a 4 × 2 × 2 full factorial design was applied and for PLA a 3 × 3 × 2 full factorial design was applied, using overall print job particle number yield (*TP*/object mass) as the dependent variable. A three-way analysis of variance test was used to determine the dominate factors influencing particle number yields amongst

filament color, filament brand and printer brand for a given filament material. For ABS, both printer brand and filament brand had statistically significant effects on emissions ($p < 0.0001$), while filament color did not. In addition to these main effects, there was an interaction effect combining printer brand and filament brand ($p < 0.0001$), demonstrated by the impact on particle emissions from filament brand also depending on printer brand. ABS filament brand had the largest effect, where filament brand *d* (a high emitter) contributed a large part of this difference. Printer brand had the second most significant effect, while filament color only had a minor effect. For PLA, printer brand contributed more to emission variation than filament brand and filament color, however, the effects of all factors were not statistically significant. Observation results are in Section 2.7.10.1 to Section 2.7.10.3; Table 2.5 shows the particle number yields, surface area yields, mass yields and particle sizes grouped by printer-filament combinations.

The type of filament material used often depends on how the print object will be utilized. Many printers can only run a certain type of filament material, whereas some can run multiple types of material. When only changing filament material and controlling all other conditions (however extruder temperature is associated with material), significant differences on particle number yields from ABS versus PLA were observed (Section 2.7.10.4). Overall, ABS number yields were 3 to 10^4 times of that of PLA yields for a given printer brand and filament brand, the variation depended on printer brand. (Note, that some PLA filaments with substantial levels of additives can have much higher particles emissions).

Since the formation of particles from FDM 3D printers is mainly linked to emissions of SVCs from the heated plastics, higher extruder temperatures should produce

higher SVC emissions and hence aerosols that are formed. When the same object was printed using ABS brand *d* on printer *A* at varying extruder temperatures, an exponential relationship tended to fit extruder temperatures and particle number yields (Figure 2.6). (Adams et al. 1999) found a similar trend for particulate emissions from commercial polypropylene processing, a process similar to FDM 3D printing where heated plastic resins (204 – 318 °C) are extruded from a die. This exponential trend likely reflects the relationship between vapor pressure of components in the filament that produce particles and temperature, since particles are formed from emitted vapors. Extruder temperature could provide a unifying explanation for many of the differences in observed emissions from different printer brands and filament materials. In Figure 2.6, comparing ABS brand *d* on printer *A* and printer *C* (dark green bars), the printer with higher extruder temperature emitted more particles, which was also true for other ABS brands (light green bars) on the two printers. No strong relationship between extruder temperature and emissions was found for the PLA tested (blue bars). In terms of particle size, average particle GMDs over the print period decreased when extruder temperature increased (Figure 2.25). When extruder temperature is high, more SVCs are generated thus forming more small particles by nucleation. At lower extruder temperatures, the nucleation rates from SVCs are lower and more vapors may condense on the formed particles increasing particle size. Therefore, reducing extruder temperature as much as feasible could be the easiest way to reduce overall emissions. Take printer *A* in this study as an example, the default extruder temperature was 270 °C for ABS. The printer appeared to work well even at 220 °C and particle number yields were reduced by a factor of ~ 6. Another way

to reduce particle emissions is to use materials that have lower melting temperatures, as demonstrated by generally lower emissions for PLA.

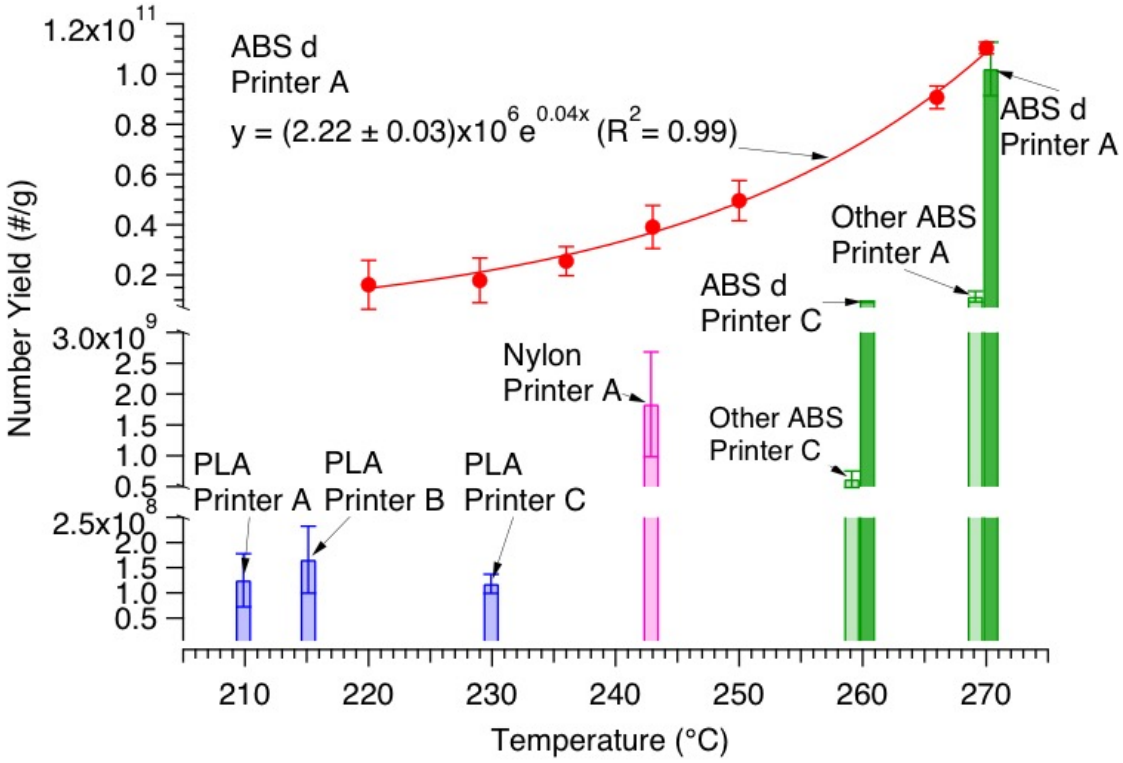

Figure 2.6 Average particle number yields for ABS, PLA and nylon filaments on various printers as a function of extruder temperature. The red circles represent ABS *d* filament on printer *A* at various extruder temperatures, with an exponential curve fitting in red line. The bars represent PLA (blue), nylon (pink) and ABS (green) filaments on various printers. Error bars are the standard error of the mean for repeated measurements.

Another potential source of SVCs might be a heated build plate where the printed object is attached, designed to minimize object warping during printing. It was found that the heating build plate did not significantly increase particle number emissions, but did increase particle sizes (Section 2.7.10.6). These results are consistent with expected aerosol dynamics. Heating the build plate may produce SVCs through contact with the printed layers. While the plate temperature (100 °C for ABS) is much lower than the

extruder (270 °C), and the emitted vapors are not confined to a small region as for the extruder nozzle and fresh emitted plastic, the vapors do not reach concentrations to form new particles, but can condense on the existing particles, leading to increase in particle sizes and thus mass yields. The effect of heating build plate for PLA was not significant; probably because the build plate temperature for PLA was too low (50 °C) to generate significant concentrations of vapors, consistent with low vapor emissions (i.e., particle emissions) from PLA in general due to lower extruder temperatures.

An overall summary of particle emissions for the filament materials tested is shown in Figure 2.7. ABS yield range covered that of nylon but was wider, though the median of ABS yield was an order of magnitude higher than nylon, mainly driven by one unusually high emitting ABS filament brand. There was large uncertainty between different PLA runs, a high emitting PLA was equivalent to ABS, but overall, PLA yield was more than two orders of magnitude lower than ABS. Some emissions from PLA were too low to be detected (maximum particle concentration less than 10 #/cm^3 during print with background concentration less than 1 #/cm^3 before print), which was never observed for ABS or nylon. The corresponding median mass yields for PLA, ABS and nylon were 0.02, 20.1 and 7.7 μg/g respectively. For particle size, the average geometric mean diameters (GMDs) for the print period are shown in Figure 2.8. GMDs for nylon and some ABS prints were larger than 100 nm, but all PLA prints produced particles smaller than 100 nm. A summary breaking down emissions into categories of filament brand and color, printer brand, and build plate heating is shown in Figure 2.26. To summarize the factors that control the emissions, filament material was the most important factor, which contributes in general 2 order of magnitude difference in particle

number yields. Filament brand is the second most important factor, in this study, one high emitter was found for ABS and one for PLA, which had one to two order of magnitude larger number yields than regular filaments. This result shows that some minor unknown constituents can have a very large effect on emissions. For ABS, printer brand had a larger effect than filament color, while it was the opposite for PLA; however, these effects were much smaller than that of filament brand. Build plate heating had even smaller effect on number yield.

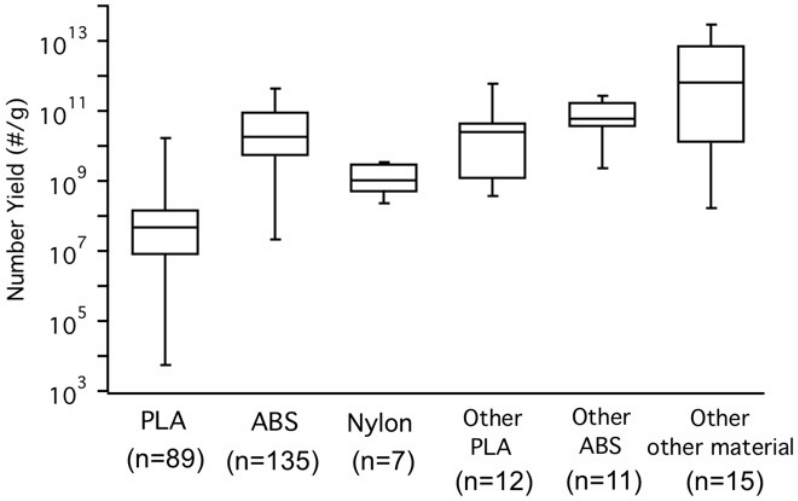

Figure 2.7 Particle number yields for various printer and filament combinations in this study (PLA, ABS and Nylon) and other published work on 3D printers (Other PLA, Other ABS and Other other material) (Stabile et al. 2017; Azimi et al. 2016; Steinle 2016; Yi et al. 2016; Kim et al. 2015). The lines in the boxes indicate the medians; the top and bottom of the boxes indicate the 75% and 25% quartiles; the top and bottom of whiskers indicate the maximum and minimum values. *n* indicates the number of data points.

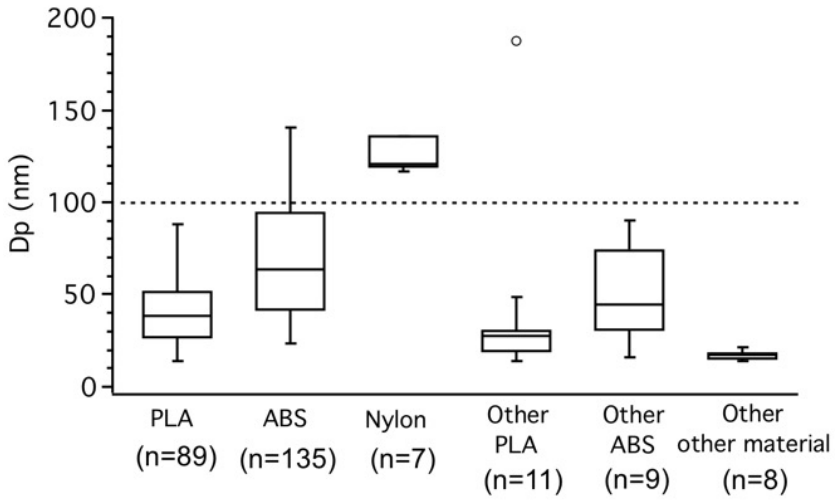

Figure 2.8 Average geometric mean diameters (GMDs) of particles throughout the print period for materials tested in this study (PLA, ABS and Nylon), compared to averaged mean or mode (most frequent) diameters from previous studies (Other PLA, Other ABS and Other other material) (Stabile et al. 2017; Steinle 2016; Yi et al. 2016; Kim et al. 2015; Stephens et al. 2013). The lines in the boxes indicate the medians; the top and bottom of the boxes indicate the 75% and 25% quartiles; the top and bottom of whiskers indicate the maximum and minimum, except the one outlier for other PLA. *n* indicates the number of data points.

2.4.4 Overall synthesis and perspectives

The particle number yields of previous studies (including 10 printers and 33 filaments, references listed in figure caption) and this study are compared in Figure 2.7. All previous studies have reported number yields ranging from 10^8 to 10^{13} #/g, although there are large uncertainties in conversion of reported data to yields, due to differences in experimental settings and data analyses methods. Our results were overlapping with the previous studies except for some PLA. In other studies, when short print times were applied, the average emission rates were dominated by number concentration peaks near the start of the print job, resulting in larger number yields compared to this study. The

range of average GMD during the printing period was comparable to previous studies, except for nylon (Figure 2.8).

Figure 2.9 and Figure 2.10 roughly compare FDM 3D printer particle emissions to that reported for laser printers (which follow a different printing protocol). Average emission rates for all studies were in the range of 10^8 – 10^{12} #/min (excluding some of our PLA results, which were lower). The range for maximum particle concentrations observed during a print job was 10^3 – 10^6 #/cm^3 (again excluding some PLA cases). Overall, the particle emissions from FDM 3D printers are comparable to laser printers in terms of particle number concentrations.

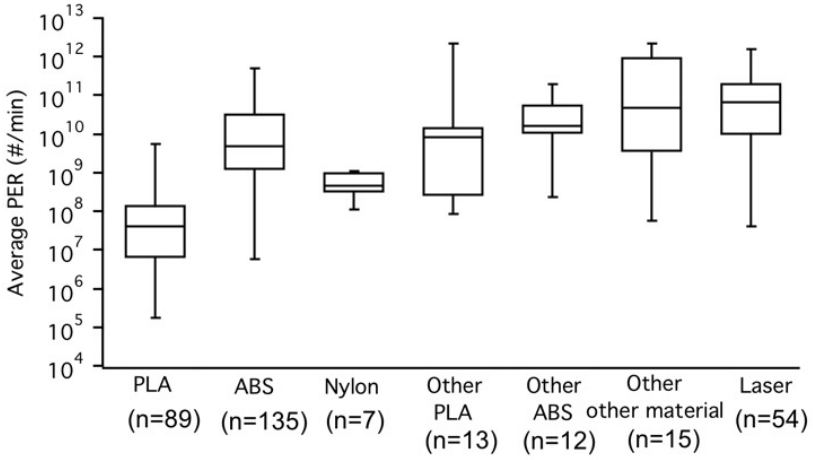

Figure 2.9 Average particle number emission rates (*PERs*) during printing period for various materials tested in this study (PLA, ABS and Nylon) and previous studies (Other PLA, Other ABS and Other other material) (Azimi et al. 2016; Stabile et al. 2017; Steinle 2016; Yi et al. 2016; Kim et al. 2015; Stephens et al. 2013), compared to laser printers (Laser) (He et al. 2007; Koivisto et al. 2010; Salthammer et al. 2012; Scungio et al. 2017). The lines in the boxes indicate the medians; the top and bottom of the boxes indicate the 75% and 25% quartiles; the top and bottom of whiskers indicate the maximum and minimum values. *n* indicates the number of data points.

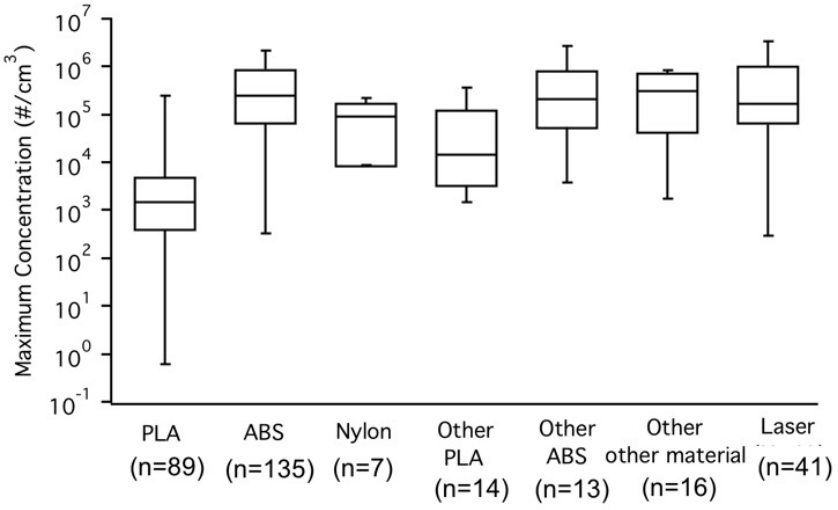

Figure 2.10 Maximum particle number concentrations including all experiments (see Table 2.3) during print period for various materials tested in this study (PLA, ABS and Nylon), and previous studies on 3D printers (Other PLA, Other ABS and Other other material) (Azimi et al. 2016; Deng et al. 2016; Kim et al. 2015; Stabile et al. 2017; Steinle 2016; Stephens et al. 2013; Yi et al. 2016; Zontek et al. 2017), compared to laser printers (Laser) (Byeon and Kim 2012; Koivisto et al. 2010; Morawska et al. 2009; Schripp et al. 2008; Wensing et al. 2008; Uhde et al. 2006). The lines in the boxes indicate the medians; the top and bottom of the boxes indicate the 75% and 25% quartiles; the top and bottom of whiskers indicate the maximum and minimum values. *n* indicates the number of data points.

To allow more quantitative comparisons between various studies, establishment of a standard test method is critical. Here we have followed the Blue Angel Method (BAM 2012), which was developed for laser printers. This established method could be the bases for developing a test protocol for consumer 3D printers. Based on our findings we recommend using yield as the parameter to evaluate emissions and to compare among diverse printer-filament combinations. A standard print time or print object mass is also recommended so that the emissions are not dominated by the initial burst in particle numbers or non-uniform emission profiles observed for some printers. A list of suggestions for a standard testing protocol inspired from the Blue Angel Method is given in Section 2.7.11.

Since a very small mass fraction (on orders of ppm) of the filament might dictate the particle emissions, which was observed as high emitting filaments in this study for both ABS and PLA, the properties of bulk filament will not provide insight on overall printer emissions. It would seem reasonable to test (and manufactures possibly publish) emissions from the material filaments are composed of as a function of temperature. An industry acceptable standard test could be developed, which would remove all variability associated with running the filaments on different printers operating under different user selected conditions and environments.

2.5 Summary

FDM 3D printers emit large quantities of non-engineered nano or ultrafine particles. The maximum instantaneous particle number concentration in our test chamber exceeded 10^6 #/cm^3 and the maximum particle number emission rate was 10^{11} #/min. Most particles generated were typically smaller than 100 nm. Differences in emissions primarily depend on the extruder temperature, which can largely account for differences between filament material and printer brand. Other conditions such as filament color and build plate temperature have smaller effects. Filament brand, likely through differences in trace components in the bulk material, can also have a substantial effect on emissions. A standardized testing and data analysis method is needed to allow comparisons between various research results and the setting of acceptable emission standards. The potential toxicity of these particles to humans is largely unknown and should be tested since particle composition may substantially differ from that of the bulk filament.

2.6 Acknowledgement

This work was funded by Underwriters Laboratories, Inc.

2.7 Supplemental Information

2.7.1 Review of previous studies on Fused Deposition Modeling (FDM) 3D printer particle emissions

Stephens et al. (2013) measured size-resolved ($11.5 < D_p < 116$ nm, where D_p is particle diameter) and total ultrafine particle (UFP, $D_p < 100$ nm) concentrations in an office environment with five same-model 3D printers operating with PLA or ABS filaments. They estimated UFP emission rates for ABS of approximately 1.9×10^{11} #/min and 2.0×10^{10} #/min for PLA.

Kim et al. (2015) tested two different printers running ABS and two different PLA (PLA1 and PLA2) filaments in a chamber with filtered air. They reported emission rates of 1.6×10^{10} #/min for ABS and $4.3 - 4.9 \times 10^{8}$ #/min for PLA. By sampling particles between 10 and 420 nm, ABS and PLA1 produced more than 96% UFPs, whereas PLA2 emitted 88% of particles larger than 100 nm. The particle mass collected on polycarbonate filters during printing was much higher for PLA2 (142 $\mu g/m^3$) than the other two filaments (below 5 $\mu g/m^3$).

Zhou et al. (2015) tested fine particles emitted from desktop 3D printers running with ABS in a clean room. The size of the particles emitted was below 10 μm, with higher concentrations for smaller size particles. Besides, the further the measurement was from the printer, the higher concentration measured.

Steinle (2016) tested one printer operating with ABS and PLA filaments in a chamber, and found the average particle (7 – 400 nm) emission rate for PLA was ~ one order of magnitude higher than that for ABS. Steinle also reported the particles were mainly volatile since emission rates decreased by 97% for PLA and 79% for ABS when passed through a thermodesorber operated at 230 °C. Experiments in office settings found ~ 5% increase in particle concentrations (background concentration 2200 #/cm^3) when printing with PLA for 165 min in a 180 m^3 well-ventilated room, while for the same print, 2 times increase in concentrations (background concentration 1200 #/cm^3) was found in a 30 m^3 room with natural ventilation.

Azimi et al. (2016) tested 16 combinations of 5 printers and 9 filament materials in a chamber with filtered air and found the range of median particle (10 nm – 1 μm) emission rates was ~ 10^8 – 10^{11} #/min for all combinations. In general, ABS had the highest emission rates and PLA had the lowest, with other materials in between. They also reported that printers with the highest built plate temperature had the highest emission rates, while no strong relationship was found between extruder temperature and particle emissions; however, the comparisons were between complex printer and filament combinations. They tested two different print objects taking similar print time and found the shape of the print object didn't significantly change the magnitude of emission rates. In addition, a printer enclosure did not significantly reduce emission rates.

Yi et al. (2016) tested one printer using ABS and PLA in a chamber with filtered air. Significant differences in particle sizes and total particle emissions between 4 ABS colors were found when controlling for other conditions, while no significant differences were found for 4 PLA colors. Generally PLA emitted smaller particles than ABS (by 30

nm in mean size) and more than 99% of the particles emitted from PLA were less than 100 nm, while for ABS 58% – 75% were smaller than 100 nm. Printing with a complete though loose-fitting cover reduced the total particle number emissions by a factor of 2 and increased the particle sizes by 1.3 times for ABS.

Deng et al. (2016) tested the effect of extruder temperature and filament feed rate by printing the same object on a printer in a clean room. Average particle concentrations increased by about an order of magnitude for a 20 °C increase in extruder temperature for both ABS and PLA. For a given temperature, 60 mm/s filament feed rate gave higher particle concentrations throughout the printing period compared to 30 and 90 mm/s for both ABS and PLA, while not as high impact as extruder temperature. At a given temperature and feed rate, ABS tended to emit more particles than PLA.

Stabile et al. (2017) compared particle emission as functions of extruder temperature and filament material by printing the same object on a printer in a room using 10 filaments and various extruder temperatures. They found particles emitted from all filaments were UFPs and the modes (most frequent size) of particles were 10 – 30 nm. Higher extruder temperatures led to higher emission rates. At the same temperature, pure PLA had the lowest emission rates; wood and copper filled PLA and copolyester filaments had the highest, while nylon, flexible PLA, and polyurethane were in between. They also considered lung alveolar surface area doses, which followed the same trends.

Zontek et al. (2017) showed the particle number concentration from printing with PLA in a well-ventilated room was ~ 10^3 #/cm^3; while it was ~ 10^4 #/cm^3 for ABS in a poorly ventilated room. They also found that the > 99% of the particles measured were

UFPs. The particles emitted from PLA and ABS were both mixture of individual and aggregated particles composed of carbon, oxygen and various metallic elements.

Table 2.2 Summary of previous studies.

	Test environment	Measurements	Printer (extruder /platform temp.) (°C)	Filament materials	No. of objects tested	Particle size mode (mean) (nm)	Maximum (mean) concentration (#/cm^3)	Average emission rate (#/min)	Notes
Stephens et al. (2013)	45 m^3 room Close door Background ~ 10^4 #/cm^3	SMPS (10–420nm)	2 (200/18) 3 (220/118) All identical printers	PLA ABS	2	48.7 36.5–48.7 All particles < 150 nm	3.1×10^4 (9.7×10^3) 1.4×10^5 (2.8×10^4)	2.0×10^{10} 2.0×10^{11}	2 PLA together 2 PLA and 3 ABS together
Kim et al. (2015)	1 m^3 acryl chamber Filtered air Background~ 4×10^3 #/cm^3 ACH=0.56hr^{-1}	SMPS (10–420nm) DustTrak (0.1–15 μm) Filter (mass)	A (250) A (210) B (220)	ABS (red) PLA1 PLA2	1	(32.6) (27.9) (188.2)	2.7×10^6 (1.7×10^6) 1.7×10^5 (5.2×10^4) 3.6×10^5 (4.6×10^4)	1.6×10^{10} 1.7×10^{11} #/g 4.9×10^8 3.8×10^9 #/g 4.3×10^8 3.9×10^9 #/g	Assumed all particles passed through the sampling filter or sampling tube
Zhou et al. (2015)	60 m^3 clean room	Grimm 1109 (0.25 – 32 μm)	1 (220) 2 (220) identical printers	ABS (green) ABS (white and green)	1	0.265 μm	25 40		The further from printer, the higher concentration measured
Azimi et al. (2016)	3.6 m^3 stainless steel chamber with stainless steel mixing fan Filtered air ACH = 1 hr^{-1}	CPC (10nm–1μm)	A (200/110) A (200/110) B (230) C (230/100) D (240/110) D (190/45) D (240/100) D (230/65) D (200/65) D (200/65) D (270/110) D (235/65) D (240/60)	ABS1 (white) PLA1 (red) PLA2 (white) ABS2 (blue) ABS1 (red) PLA1 (red) HIPS (black) Nylon (semitransparent) Laybrick (white) Laywood (brown) Polycarbonate (transparent) PCTPE (semitransparent) T-Glase (transparent	2		8.6×10^5 1.5×10^3 2.1×10^3 2.6×10^5 9.0×10^5 3.1×10^3 9.0×10^5 8.7×10^4 1.8×10^3 2.3×10^3 7.7×10^5 4.0×10^5 	1.7×10^{10} 9.2×10^7 1.3×10^8 1.7×10^{10} 9.4×10^{10} 9.6×10^7 3.6×10^9 2.5×10^8 5.9×10^7 8.8×10^7 4.8×10^{10} 2.3×10^{10} 	Dynamic mass balance with particle losses; Heating of platform increased particle emissions.

	Test environment	Measurements	Printer (extruder /platform temp.) (°C)	Filament materials	No. of objects tested	Particle size mode (mean) (nm)	Maximum (mean) concentration (#/cm^3)	Average emission rate (#/min)	Notes
				red) ABS1 (white)			7.9×10^5	5.0×10^9	
			E (230/110) w/o enclosure				7.7×10^5 5.1×10^5	5.8×10^{10} 4.4×10^{10}	
Steinle (2016)	85L acrylic glass chamber w/. a small fan Filtered air ACH = 16 hr^{-1}	Filter and TEM (UFPs & occupational aerosols) ICPOES (metal) ASM (0.18–20μm)	1	ABS (yellow)	1	60 – 90	1.6×10^4 (1.1×10^4)	2.4×10^8 2.4×10^9 #/g	Particle emissions increased after 7 month of usage of printer; Trace metals (Fe, Zn) found in particles; Particles are mainly volatile.
				PLA (yellow)	5	20 – 30	1.1×10^5 (8.9×10^4)	2.1×10^9 1.7×10^{10} #/g	
	180 m^3 room Open door ACH = 2 hr^{-1}	EDB (7 – 400 nm)		PLA (yellow)	1		2.7×10^3 (1.7×10^3)		
	30 m^3 room Close door			PLA (yellow)	1	> 100 nm, amorphous, agglomerate	3.3×10^3 (3.2×10^3)		
Yi et al. (2016)	500 L stainless steel chamber Filtered air Background ~ 500 #/cm^3 ACH = 3 hr^{-1}	P-Trak (0.02–1μm) OPC (0.3– >20μm) ELPI (0.024–9.38 μm) SMPS (14.6–660 nm) NanoScan SMPS (0.01-0.36 um) DustTrack (mass) External Surface area concentration monitor	1 (230/110) (215)	ABS (red) (blue) (natural) (black) PLA (true red) (ocean blue) (transparent blue) (army green)	2	(70) (79) (70) (45) (28) (28) (30) (32) SMPS data	3.0×10^5	5.2×10^{10} #/g 2.8×10^{10} #/g 6.2×10^{10} #/g 3.8×10^{10} #/g 3.9×10^{10} #/g 3.4×10^{10} #/g 4.8×10^{10} #/g 3.9×10^{10} #/g SMPS data	Cover of printer reduced total particle emissions and increased particle mean size
Deng et al. (2016)	8 m^3 room Background < 5 #/cm^3 Monitors in another room ACH = 0.1hr^{-1}	CPC (2.5 nm –1 μm)	1 (200/110) (220/110) (240/110) (180/60) (200/60) (220/60)	ABS (red) PLA (black)	1		5.6×10^3 8.1×10^4 2.2×10^5 3.7×10^3 5.3×10^3 3.1×10^4		60 mm/s feed rate emitted more particles compared to 30 and 90 mm/s

	Test environment	Measurements	Printer (extruder /platform temp.) (°C)	Filament materials	No. of objects tested	Particle size mode (mean) (nm)	Maximum (mean) concentration (#/cm^3)	Average emission rate (#/min)	Notes
Stabile et al. (2017)	40 m^3 room Close door Background $0.2–3\times10^4$ #/cm^3 ACH=0.22hr^{-1}	CPC (> 4 nm) Dusktrak (PM_1, $PM_{2.5}$, PM_{10}) SMPS (6–220 nm) Nanoparticle surface area monitor	1 (220, 230, 240) (220, 230, 240) (230, 240) (220, 230, 240) (210, 220, 230, 240) (240) (220, 230, 240) (220, 230, 240) (230, 240) (230, 240)	Pure PLA Wood PLA Wood PLA2 Copper PLA Bamboo PLA Flex PLA Copolyester Carbon copolyester Nylon Ninjaflex	1	20 – 30 No super-micron particles for all filaments	$0.5–4.9\times10^4$ $1.5–9.3\times10^4$ $7.0–9.5\times10^5$ $3.6–6.7\times10^5$ $0.3–9.5\times10^5$ 2.4×10^4 $0.9–5.6\times10^5$ $1.1–4.8\times10^5$ $1.3–1.4\times10^4$ $1.8–5.8\times10^4$	$0.7–1.0\times10^{10}$ $0.6–2.6\times10^{11}$ $1.9–2.8\times10^{12}$ 2.0×10^{12} $1.7\times10^{10}–2.7\times10^{12}$ 4.2×10^{10} $0.2–1.6\times10^{12}$ $0.2–1.2\times10^{12}$ $1.4–1.6\times10^{11}$ $0.7–1.4\times10^{11}$	Emissions increased when temperature increased
Zontek et al. (2017)	10m×10m×6m laboratory, ACH = 20 hr^{-1} 3m×9m×6m room, ACH = 1.8 hr^{-1}	CPC (0.01 to >1 um) SMPS (3 - 300 nm) OPS (300 nm - 10 μm) TEM ATR-FTIR EDAX	A (180-230) B (213)	PLA ABS	1 1	Inside enclosure (30.5); outside (16.3)	3.3×10^3 Inside enclosure 2×10^5; outside 3×10^3		Enclosure reduced ~ 95% number and mass concentrations; Particles have irregular shapes

SMPS (scanning mobility particle sizer); CPC (condensation particle counter); OPC (optical particle counter); ASM (Aerosol Spectrometer); EDB (Electrical Diffusion Battery); TEM (transmission electron microscope); ELPI (electrical low-pressure impactor); OPS (optical particle sizer); ATR-FTIR (attenuated total reflectance Fourier transform infrared spectroscopy); EDAX (energy dispersive analysis of X-rays)

2.7.2 Experimental design

Table 2.3 Printer-filament combinations tested in this study.

Material	Printer brand	Extruder temperature (°C)	Build plate temperature (°C)	Filament brand	Color	No. of object model
ABS	A	270	100	a	Red, white	3
	A	270	100	c	Red, white	3
	A	270	100	d	Red, white	3
	A	270	100	d	Green	3
	A	270	100	d	Blue	6
	A	270	100	d	Yellow	11
	A	270	100	f	Red, white	3
	A	266	100	d	Yellow, blue	1
	A	250	100	d	Yellow, blue	1
	A	243	100	d	Yellow, blue	1
	A	236	100	d	Yellow, blue	1
	A	229	100	d	Yellow, blue	1
	A	220	100	d	Yellow, blue	1
	A	270	No heating	a	Red	1
	A	270	No heating	d	Red	1
	C	260	No heating	a	Red, white	3
	C	260	No heating	c	Red, white	3
	C	260	No heating	d	Red, white	3
	C	260	No heating	f	Red, white	3
	E	230	110	g	Green, white	2
	F	270	100	j	White	2
PLA	A	210	50	b	Red, white	3
	A	210	50	c	Red, white	3
	A	210	50	f	Red, white	3
	A	210	No heating	c	Red	1
	B	215	No heating	b	Red, white	3
	B	215	No heating	c	Red, white	3
	B	215	No heating	f	Red, white	3
	C	230	No heating	b	Red, white	3
	C	230	No heating	c	Red, white	3
	C	230	No heating	f	Red, white	3
	D	215	No heating	h	White	2
	D	215	No heating	i	Gray	2
	F	210	50	j	Nature	2
Nylon	A	243	100	e	Nature	3

2.7.3 Instrumentation

Table 2.4 Specifications of aerosol instrumentation used in this study.

Instrumentation	Condensation particle counter (CPC)	Scanning mobility particle sizer (SMPS)	Optical particle counter (OPC)
Model	3022A, TSI Inc.	electrostatic classifier 3080, differential mobility analyzer 3081, water CPC (WCPC) 3785, TSI Inc.	AeroTrak 9306-01, TSI Inc.
Measurement	Number concentration	Number distribution	Number distribution
Particle size	7 nm to > 3 μm	7-300 nm (103 channels)	0.3-25 μm (6 channels)
Sample interval	2 seconds	135 seconds	60 seconds
Software	Aerosol Instrument Manager, TSI Inc.		TrakPro Lite, TSI Inc.

2.7.4 Tests on the consistency between CPCs

The accuracy of the two CPCs routinely operated in the tests (TSI WCPC 3785 and TSI CPC 3022A) was verified by comparing with an ultrafine condensation particle counter (UCPC, TSI 3025A) having a lower size detection limit when measuring particle emissions from the 3D printer side by side. When particle number concentrations were below 2×10^4 #/cm^3 and the CPCs operated mainly in single particle count mode (± 10% uncertainty), the WCPC agreed with the UCPC (Figure 2.11a), while the 3022A CPC was approximately 40% higher (Figure 2.11b). However, it was found that when concentrations exceeded approximately 10^4 #/cm^3, the 3022A CPC readings jumped by ~ a factor of 2 due to switching to photometric count mode, resulting in higher measurement uncertainty (± 20%). Due to the high concentration of particles in the experiments, an advantage of the SMPS is that the associated WCPC was generally

always in single particle count mode since only particles in small size bins are counted, instead of all particles at once. Therefore in this study, integrated SMPS number distributions were mostly used to provide total number concentrations. This also provided consistency between the number, surface area and mass distributions. However for cases when particle concentrations were low (total particle number concentrations less than ~ 1000 #/cm^3, which can occur for PLA filament tests), the SMPS didn't perform as well due to low counting statistics, making the integrated total concentrations and calculated surface area and mass distributions highly uncertain. In these cases, 3022A CPC data (adjusted to agree with the UCPC data according to Figure 2.11b) was used to report total particle number emissions.

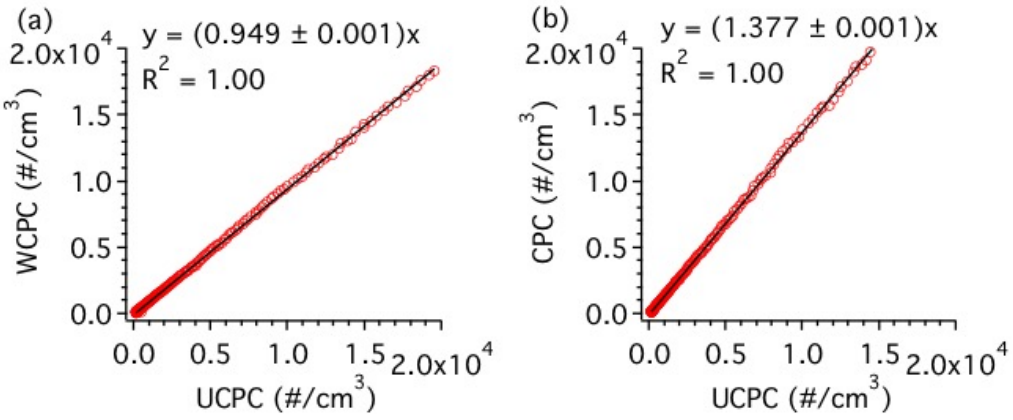

Figure 2.11 Consistency between WCPC and UCPC (a) and between CPC and UCPC (b) respectively. The print condition was printer *A* with ABS filament brand *a* white. Circles are data points; lines are linear regression fits with zero intercept.

2.7.5 Data analysis methods

2.7.5.1 Particle concentrations (C_p)

C_p can refer to particle number, surface area or mass concentrations, for size-resolved or total concentrations. Particle number concentrations reported by the CPC (D_p > 7 nm) were averaged over nominally 1 min to smooth the data. For the SMPS and OPC, which provided concentrations as a function of size, surface area and volume distributions were determined from measured number distributions assuming spherical particles. Mass concentrations were determined from calculated volume concentrations assuming particle density of the bulk filament materials. Total concentrations of all sizes were calculated assuming a single size for each bin, and then integrated over the instrument's measurement range.

It is noted that electron micrographs of 3D printer particles show they are amorphous or agglomerates (Steinle 2016), indicating the spherical particle assumption can lead to errors in surface area and mass concentration calculations, as well as the particle sizing of the SMPS and OPC measurements. We estimated the uncertainties with spherical particle assumptions and did not attempt to correct the data since we have insufficient data on particle shape and porosity that can affect aerodynamic drag and actual surface area. We note that these assumptions are common to all published work on 3D printer emissions involving particle sizing. Zontek et al. (2017) TEM images showed single particles were irregular, but close to spheres. As a worst-case scenario, we assumed all particles of various sizes are agglomerates composed of spherical primary particles. Based on the study of Zelenyuk et al. (2006), the dynamic shape factor for polystyrene latex sphere agglomerates was ~ 1.2 for 3 to 10 primary particle agglomerates, compared to 1 for single spheres. Since the 3D printer particles are a mixture of individual particles and agglomerates of different sizes, by assuming all

particles are agglomerates we estimate a maximum electrical mobility diameter sizing bias of 20% for the SMPS (actual electrical mobility diameters up to 20% smaller than what we reported assuming spherical particles). We did not consider sizing errors for the OPC since these larger particles generally make minor contributions to overall emissions, and OPC is based on optical properties. Ku and Maynard (2005) found that the particle surface areas from an SMPS measurement (spherical assumption for sizing and calculation of surface area from number concentrations) agreed with TEM-inferred surface areas for spherical and fractal-like particles smaller than nominally 100 nm. In other studies for particle sizes of 20 to 400 nm, SMPS surface area measurements were 15% biased low (Asbach et al. 2009) to 30% biased low (Ntziachristos et al. 2007) compared to nanoparticle surface area monitors. The conversion of number distributions to mass distributions by an SMPS using a particle density of 1 g/cm^3 was biased 30% high (Shi et al. 1999), compared to mass collected on a filter. Also, the effective density for agglomerates can be much lower than the bulk material density (Charvet et al. 2015), which will add to uncertainties for mass estimations. We estimated the effective density of the 3D printer particles with a dynamic shape factor of 1.2 to be ~ 0.7 of the filament bulk density. Combining these effects lead to an overall bias of 40% high when converting number distributions to mass distributions.

2.7.5.2 Particle loss coefficient (β)

Particles removed from the air in the chamber due to transport out of the chamber associated with the continuous air exchange, instrument sampling and loss to the walls were calculated based on the exponential decay of particles after printing stopped. It was

assumed that the particle loss rates were constant and applied for both the printing period and post-printing period and calculated by:

$$\beta = \frac{ln\left({}^{C_1}/_{C_2}\right)}{t_2 - t_1} \quad (1)$$

where t_1 (s) is at least 5 min after the end of the print phase and t_2 (s) is at least 25 min after t_1. C_1 (#/cm^3) and C_2 (#/cm^3) are the corresponding particle concentrations. The unit for β is s^{-1} for number concentration.

2.7.5.3 Particle emission rate (*PER*)

Particle emission rates as a function of time are calculated using C_p (corrected with β) based on a mass balance and is given by:

$$PER = V_c\left(\frac{C_p(t) - C_p(t - \Delta t)exp(-\beta \cdot \Delta t)}{\Delta t\ exp(-\beta \cdot \Delta t)}\right) \quad (2)$$

where V_c (cm^3) is the volume of the chamber and Δt (s) is the time interval between two successive data points. Unit for *PER* is #/s for number concentration.

2.7.5.4 Total particle emission (*TP*)

Total particle emissions for the complete print job were calculated by integrating particle concentrations over the emission period, which was determined from the C_p and *PER* curve:

$$TP = V_c \left(\frac{\Delta C_p}{t_{stop} - t_{start}} + \beta \cdot C_{av} \right) \left(t_{stop} - t_{start} \right) \quad (3)$$

where t_{start} is the time when C_p begins to increase; t_{stop} is when *PER* remains steady (below 10% of the maximum of *PER* over at least the next 10 min); ΔC_p (#/cm^3) is the difference in C_p between t_{stop} and t_{start}; C_{av} (#/cm^3) is the arithmetic average of C_p between t_{start} and t_{stop}. Unit for *TP* is # for number concentration.

2.7.5.5 Statistics

Statistical methods were used to examine the quality of experimental data and to interpret the results. The sample population (*n*) for each experimental condition was four, unless noted. A Dixon's Q test was applied to determine whether an outlier should be rejected, using a 95% confidence interval. One-way analysis of variance (ANOVA) was used to determine if a difference existed between the means of several independent groups. The Student's t-test was used for determining if the two data sets are different. Factorial ANOVA was used to investigate the main effects and the interaction effects of multiple variables. The *p* value was 0.05 for all statistical tests.

2.7.6 Effect of initial background particle concentrations on particle emissions

The room air initial condition in this study was (5.4 ± 2.9) × 10^4 #/cm^3 in number concentration, 432 ± 128 μm^2/cm^3 in surface area and 5.23 ± 1.21 μg/m^3 in mass (SMPS data); typical indoor environments (Fromme 2012).

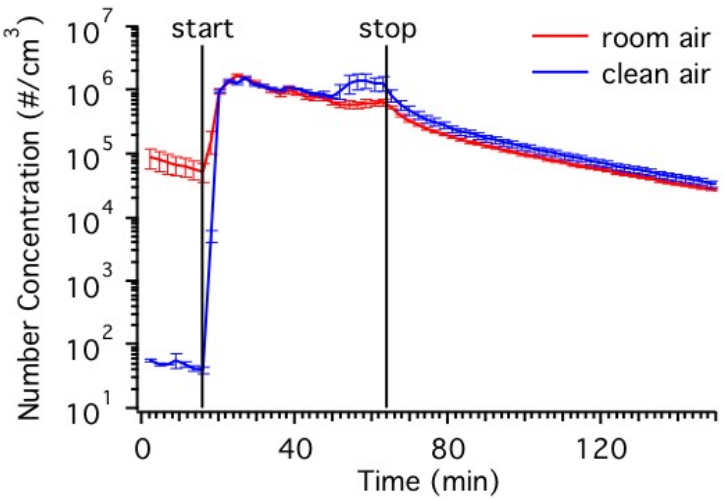

Figure 2.12 Time series of particle number concentrations when particle-free air versus room air was introduced into the chamber before print started. The printing condition in both cases was red ABS filament brand *d* on printer *A*, printing time was 44 min, identified by the vertical lines. Error bars are standard error of the mean.

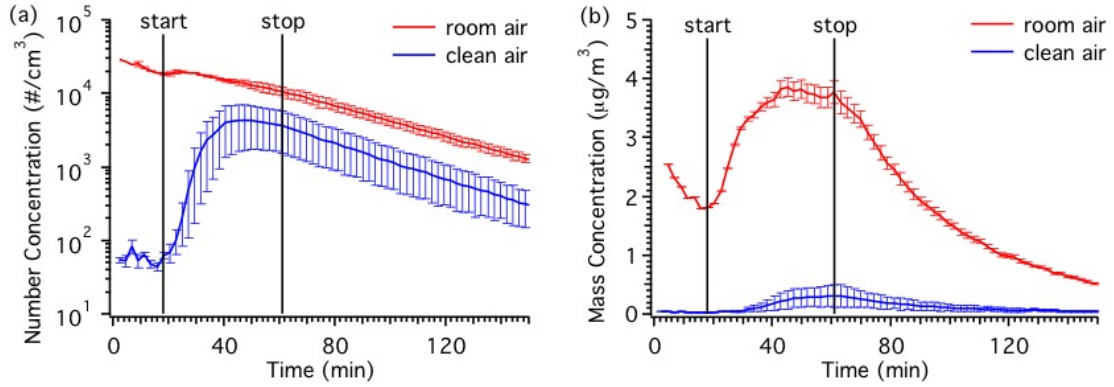

Figure 2.13 Time series of particle number concentrations when particle-free air versus room air was introduced into the chamber before print started. The printing condition in both cases was red PLA filament brand *c* on printer *A*, printing time was 44 min, identified by the vertical lines. Error bars are standard error of the mean.

2.7.7 Aerosol dynamics

A differing time series trend was found for a specific printing condition using ABS (Figure 2.14), the maximum number concentration occurred at the end of printing

and the growth of particles was only apparent at the beginning of print period. However, it was found that the *TP* from printing the same object stay relatively the same and was largely independent of the variation of aerosol changes observed during the printing period.

The increase in particle number concentrations at the start of the print for PLA was typically hundreds particles cm^{-3} (Figure 2.15a), and most of the particles emitted were smaller than 50 nm. Since PLA filaments tend to emit less vapors, and generate less particles, the background noise becomes more apparent (Figure 2.15b); this is especially true for surface area (Figure 2.15c) and mass concentrations (Figure 2.15d). The increase of particle surface area and mass were even less than the background because large particles, though fewer in numbers, contribute much more to surface area and mass concentrations. Particle concentrations and size distributions didn't reach a steady state throughout the printing period. A high emitting PLA brand was found having a different particle concentration and evolution behavior from regular PLA (Figure 2.16), which was caused by the additives other than bulk PLA material.

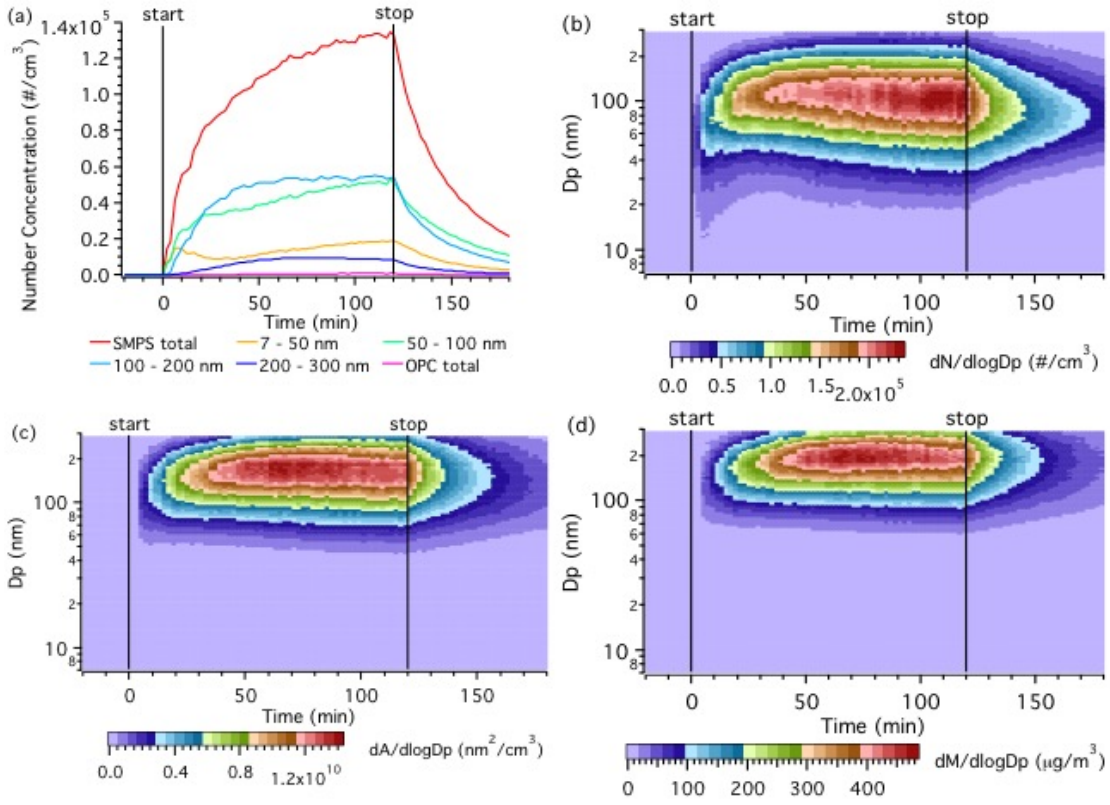

Figure 2.14 An example of a differing aerosol concentration trend during print. The print condition was printer *E*, filament ABS brand *g* green color. (a) is the time series of particle number concentrations grouped by particle sizes. The print time was 2 hr, indicated by vertical lines. (b) (c) and (d) are particle number, surface area and mass concentration distributions measured by the SMPS.

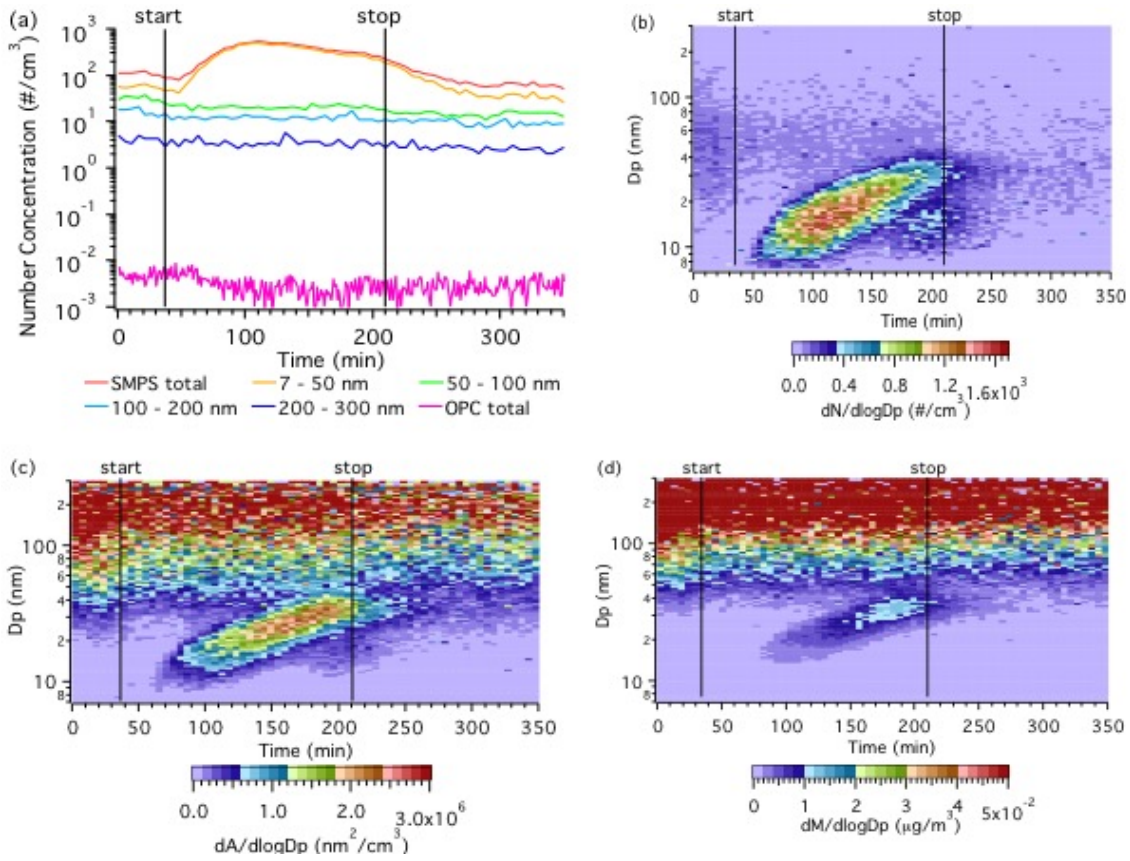

Figure 2.15 Example of aerosol dynamics of PLA filament (printer *A* filament brand *c* white color, 3-hr print). (a) is the time series of particle number concentrations grouped by particle sizes. (b) (c) and (d) are particle number, surface area and mass concentration distributions measured by the SMPS.

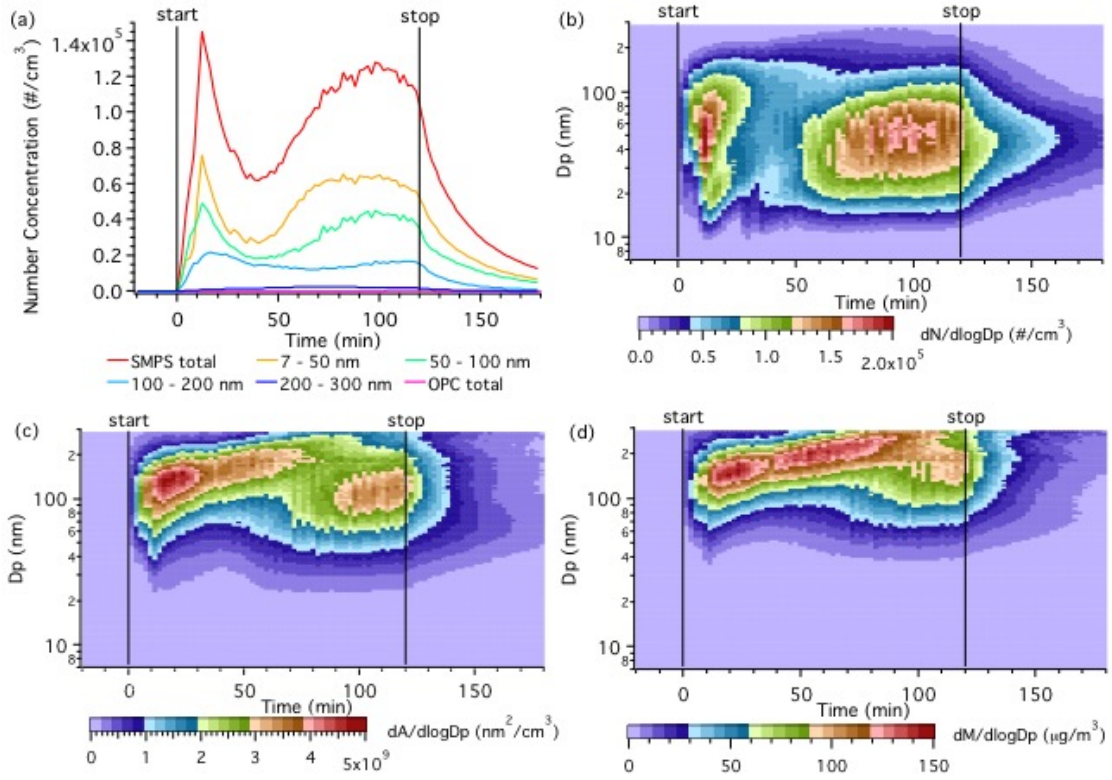

Figure 2.16 Example of aerosol dynamics of a high emitting PLA filament (printer *D* with PLA brand *i* grey color, 2-hr print). (a) is the time series of particle number concentrations grouped by particle sizes. (b) (c) and (d) are particle number, surface area and mass concentration distributions measured by the SMPS.

2.7.8 Size distributions for particle surface area and mass

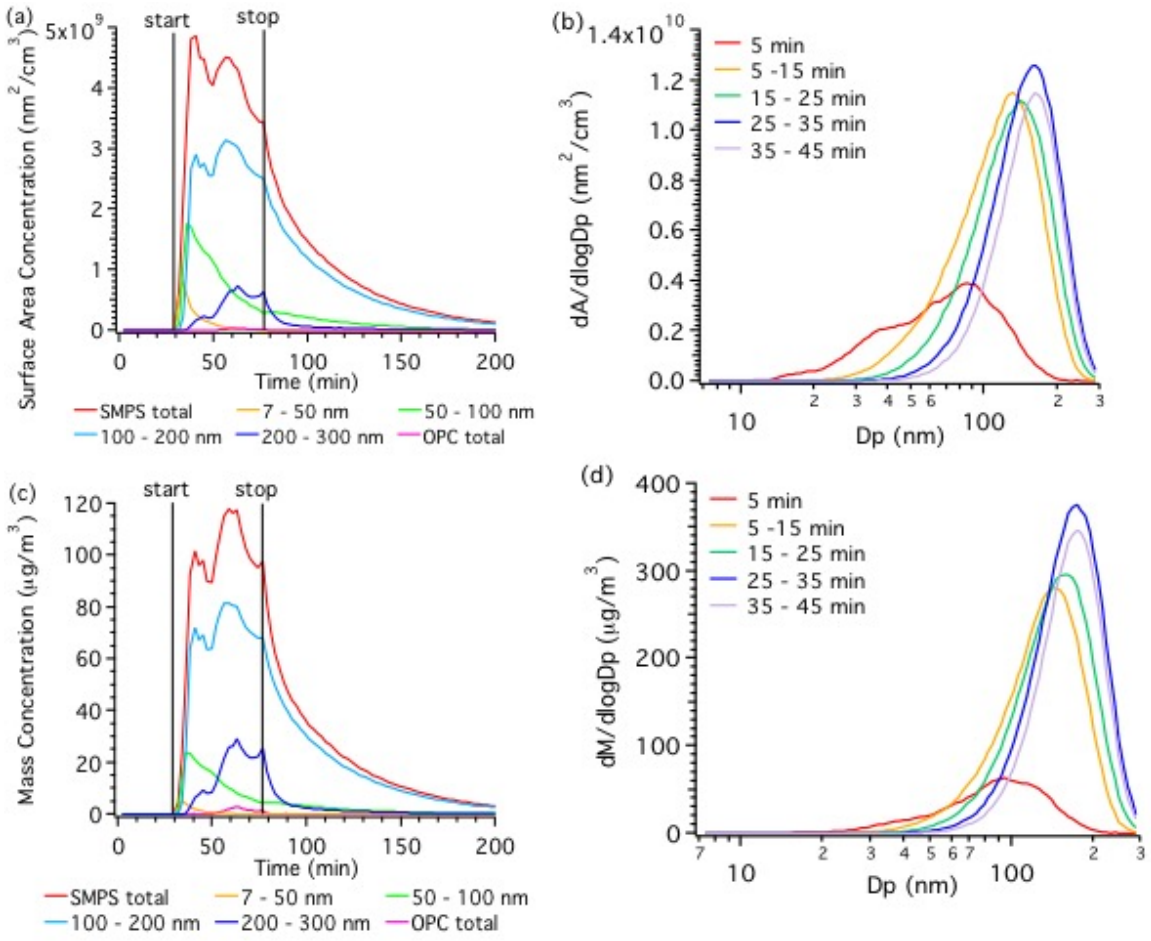

Figure 2.17 Time series of particle surface area concentrations averaged over various particle size ranges (a) and average particle surface area distributions for 5 time intervals during printing period (b) for ABS filament brand *a* red color on printer *A*; and the corresponding mass concentrations (c) and size evolution (d) for the same print. The print time was 47 min identified by the vertical lines.

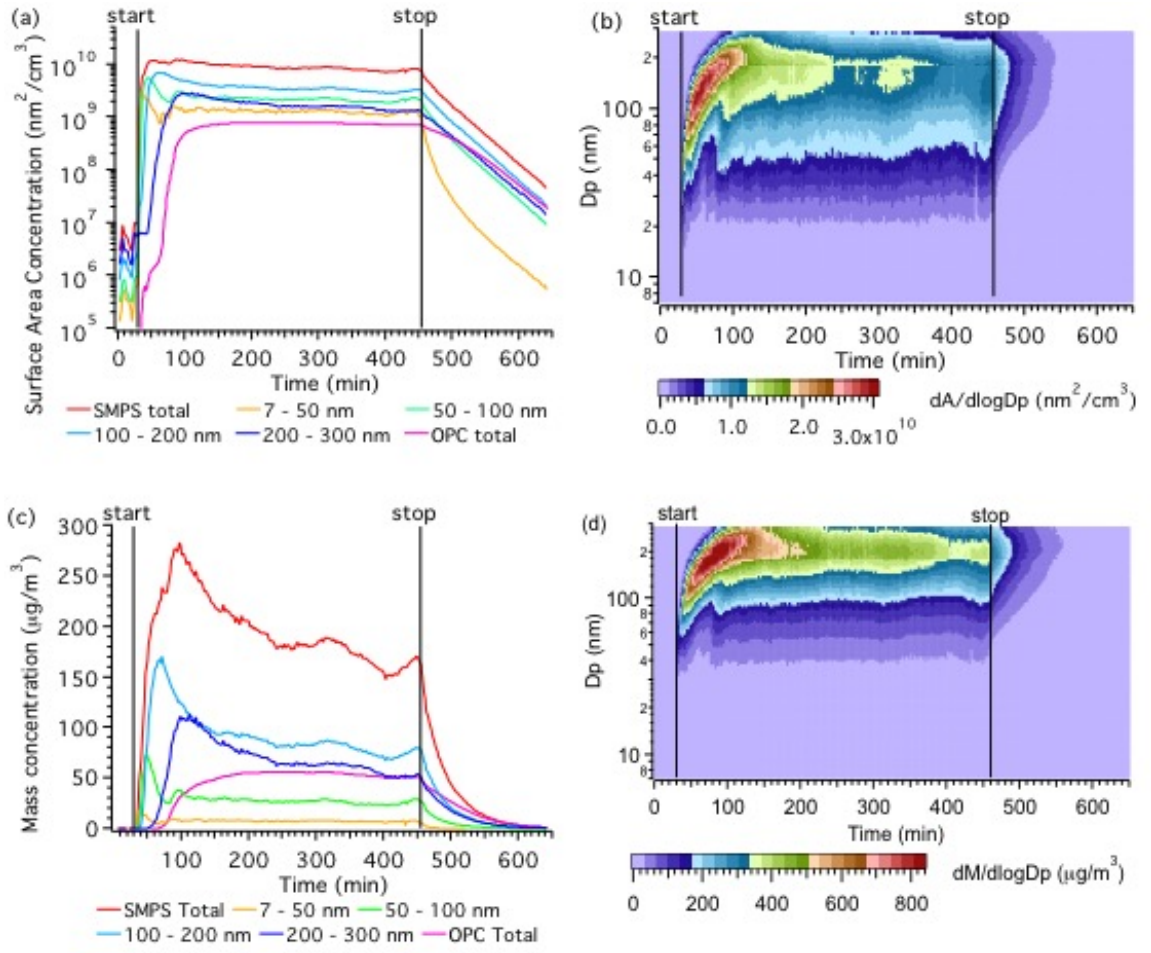

Figure 2.18 Long print job time series of particle surface area concentrations (a) and size distributions (b) for ABS filament brand *d* green color on printer *A*; and the corresponding mass concentrations (c) and size evolution (d) for the same print. The print time was 7 hr 4 min identified by the vertical lines.

2.7.9 Average particle emissions and loss rates as a function of particle size

The average particle emission rates for a complete print job, and the loss rates calculated from the post-printing decay period for 7 nm to 10 µm particles are shown in Figure 2.19. For the particle number emission rates, the trends were similar to what has been observed for other particle generating processes, such as cooking activities and pyrolysis cleaning of oven within homes (Géhin et al. 2008). In terms of numbers, particles had largest emission rates were in 20 – 40 nm size range for both the short and

long print jobs. In terms of surface area and mass, for the short print, the largest emission rates were for 60 – 100 nm particles; given longer time, the maximum emission rates appeared when particles were about 200 nm. Particle loss rates as a function of size were scattered for the 1 hr print job, but for the 7 hr print (Figure 2.19b), the loss rates decreased as particle sizes increased from 20 – 100 nm, because smaller particles are more likely to diffuse to surfaces and coagulate with larger pre-existing particles to be removed.

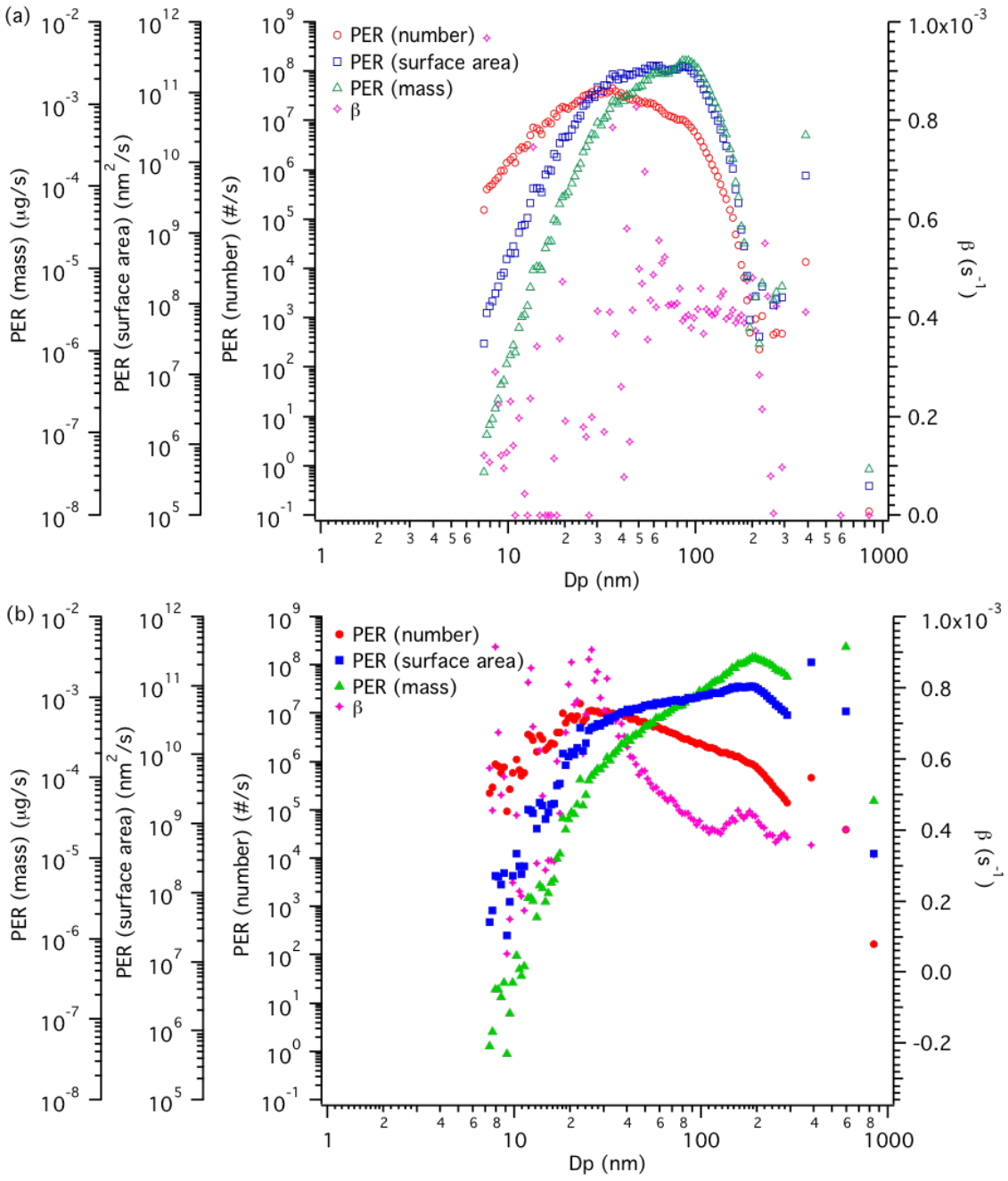

Figure 2.19 Average *PERs* for particle number, surface area and mass concentrations, and the particle loss rates as a function of particle size for the 1 hr print (a) and the 7 hr print (b) discussed in Figure 2.2 and Figure 2.3.

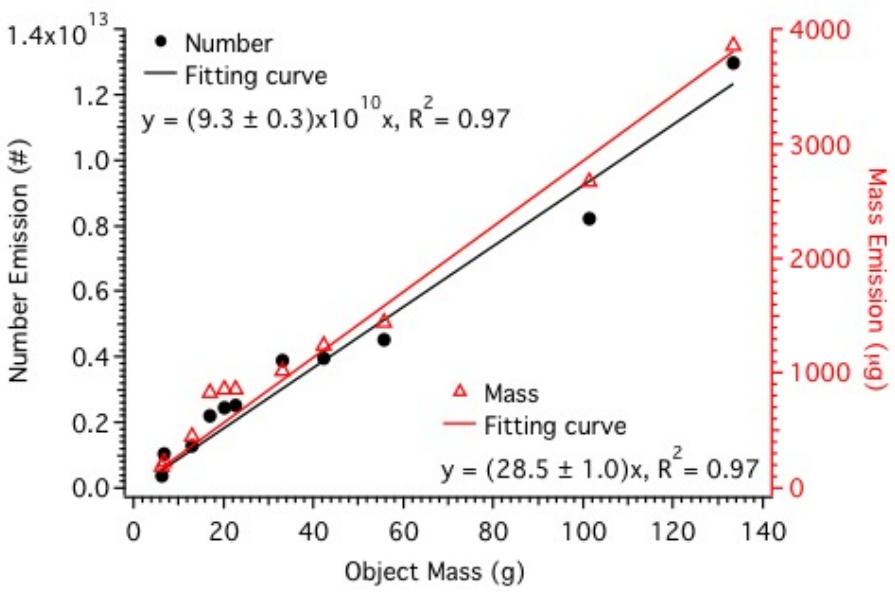

Figure 2.20 Particle number and mass emissions for various print objects as a function of object mass, fitted by linear regression. Variability in the data is due to the minor effect of differences in print object shape.

2.7.10 Factors influencing particle emissions

2.7.10.1 Filament color

Five ABS filaments of different colors (white, yellow, red, green and blue) from the same manufacturer (brand *d*) were used on printer *A* under the same operation conditions. A comparison of average yields for each color is shown in Figure 2.21. There was no statistically significant difference in yields between colors. In term of particle sizes, the difference between geometric mean diameters (GMDs) of the average distribution over the print period was not significant either. This was also found to be true for other filament brands; no statistical differences were found between particle number yields or particle sizes when comparing white and red ABS filaments for brand *a*, *c* or *f* on printer *A* and printer *C* respectively. Also for PLA, no differences were found for

number yields or particle sizes for the 9 combinations of brand *b*, *c*, *f* PLA (red versus white) on printer *A*, *B* and *C*.

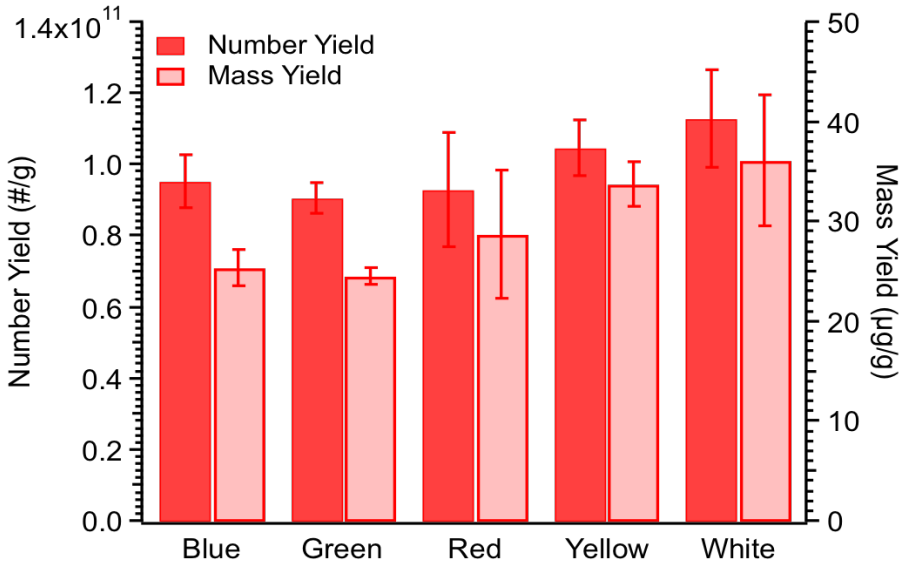

Figure 2.21 Particle number and mass yields for various colors of ABS filament *d* on printer *A*. Error bars are standard error of the mean. Difference between the 5 color data sets was not statistical significant (p = 0.69 for number yield and 0.12 for mass yield).

2.7.10.2 Filament brand

In one case filament brand had a large effect on particle emissions. Four different ABS filaments were obtain from different companies (brands *a*, *c*, *d*, *f*) and were used on printer *A*. Brand *d* had significantly higher average number yields (order of 10^{11} #/g) than the others tested brands (~ 10^{10} #/g), whereas no significant difference between the other brands was observed (Figure 2.22). The high emitter (brand *d*) produced smaller particles. The average GMD for brand *d* was 41 ± 1 nm, approximately half of that of the other brands (97 ± 18 nm) (Table 2.5), among which no statistical significant difference in GMD was found. Similar results were found when applying these four filaments on

printer *C*. This *d* filament likely produced significantly more semi-volatile compounds, resulting in a much higher NPF rate near the extruder nozzle, leading to more small newly formed particles. Three PLA brands (*b*, *c*, *f*) were tested on printer *A*, *B* and *C* respectively, no high emitter (like ABS brand *d*) was detected and the yields from different filament brands were overlapping and there was no significant difference among the particle sizes emitted from different filament brands. However a high PLA emitter (brand *i*) was found when operating on printer *D*, which emitted one order of magnitude more particles than regular PLA filaments, and will be included in the overall emission comparisons.

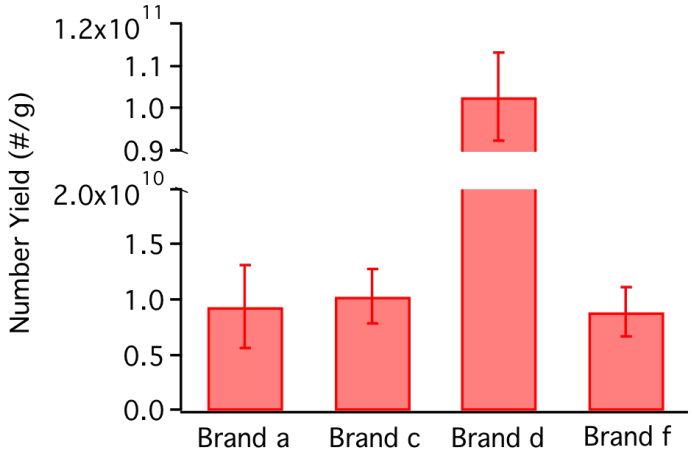

Figure 2.22 Average particle number yields for various ABS filament brands on printer *A*; each bar indicates a filament brand. Error bars are standard error of the mean.

2.7.10.3 Printer brand

The same ABS filament was run on two printers, *A* and *C*. Average number yield for printer *A* was 17 times that of printer *C* (Figure 2.22). However, no differences in particle sizes were found (GMD values shown in Table 2.5). The concentration profile

during printing also differed. Possible reasons for the observed differences between these printers include: (1) filament feed rate (0.23 ± 0.03 g filament/min for printer *A*, the one with higher emissions, compared to 0.14 ± 0.02 g filament/min for printer *C*); (2) extruder temperature; (3) build plate temperature and (4) deposition surfaces (i.e., enclosure). See for details. For PLA, there was no statistically significant difference among the number yields for different printers, and the mean number yield was ~ 10^8 #/g considering all printers tested.

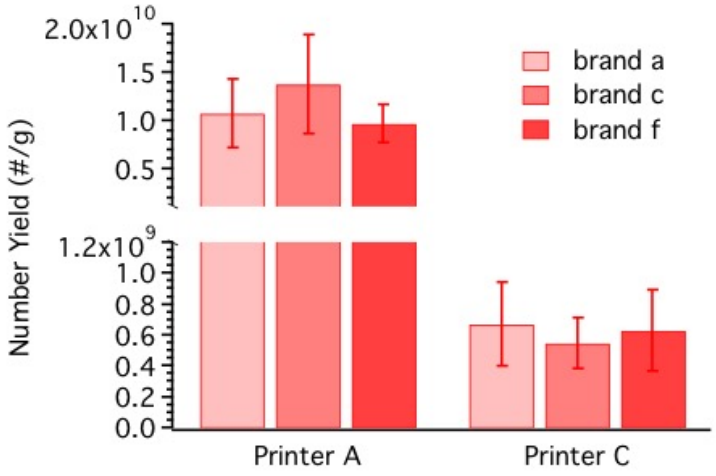

Figure 2.23 Average particle number yields for various ABS filament brands on printer *A* and *C* respectively; each bar indicated a filament brand. Error bars are standard error of the mean.

2.7.10.4 Filament material

When controlling for all print conditions except filament material (associated with extruder temperature), we found the average number yield of ABS was 72 times of that of PLA for printer *A* running filament brand *c* (Figure 2.24). Similar results were found for printer *A* running filament brand *f* (ABS ~ 10^4 times of PLA), and printer *C* running

filament brand *c* (ABS ~ 9 times of PLA) and brand *f* (ABS ~ 3 times of PLA), thus the difference appears to be due to filament material.

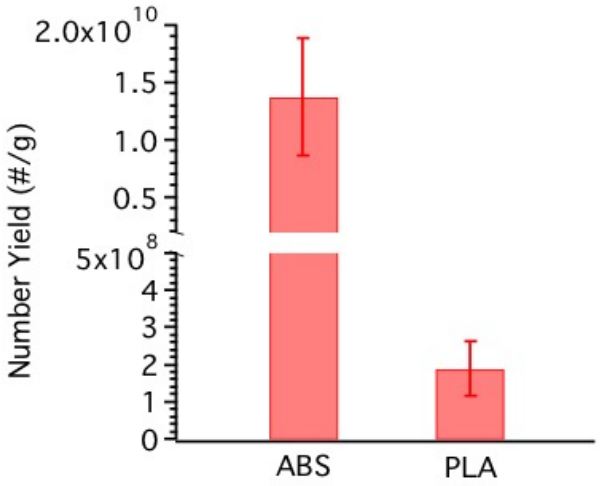

Figure 2.24 Particle number yields for brand *c* ABS and PLA filament on printer *A*. Error bars are standard error of the mean.

Table 2.5 Average particle number, surface area and mass yields and average GMDs for specific printer-filament combinations (e.g., number yield = number *TP*/object mass). The first letter of notation in Combination (column 1) indicates printer brand and the second letter indicates filament brand. All data were based on 8 replicates (4 red and 4 white), for low emitting PLA cases, number yield calculated from CPC data was used; the data not qualified to calculate surface area and mass emissions were removed, with ^{*n} indicating the numbers of replicates of these cases.

Combination	Number yield (#/g)	Surface area yield (μm^2/g)	Mass yield (ppm)	Average GMD (nm)
Aa (ABS)	$(1.08 \pm 0.35) \times 10^{10}$	$(3.69 \pm 0.70) \times 10^{8}$	16.49 ± 2.80	98.6 ± 3.5
Ac (ABS)	$(1.38 \pm 0.51) \times 10^{10}$	$(5.13 \pm 0.82) \times 10^{8}$	25.51 ± 1.96	90.4 ± 9.1
Ad (ABS)	$(1.02 \pm 0.11) \times 10^{11}$	$(1.43 \pm 0.18) \times 10^{9}$	35.01 ± 4.38	40.7 ± 0.5
Af (ABS)	$(9.71 \pm 1.94) \times 10^{9}$	$(6.13 \pm 0.99) \times 10^{8}$	27.45 ± 3.59	103.0 ± 5.8
Ca (ABS)	$(6.72 \pm 2.70) \times 10^{8}$	$(2.19 \pm 1.22) \times 10^{7}$	0.59 ± 0.35	92.0 ± 5.2
Cc (ABS)	$(5.48 \pm 1.68) \times 10^{8}$	$(1.19 \pm 0.40) \times 10^{7}$	0.41 ± 0.15	118.3 ± 10.5
Cd (ABS)	$(9.45 \pm 0.79) \times 10^{9}$	$(2.49 \pm 0.24) \times 10^{8}$	6.13 ± 0.55	66.0 ± 2.4
Cf (ABS)	$(6.36 \pm 2.66) \times 10^{8}$	$(2.10 \pm 0.87) \times 10^{7}$	0.80 ± 0.24	99.2 ± 6.4
Ab (PLA)	$(3.43 \pm 3.22) \times 10^{8}$ ^{*7}	2.70×10^{6} ^{*1}	$8.1 \times 10\text{-}3$ ^{*1}	16.8 ± 1.5 ^{*3}
Ac (PLA)	$(2.02 \pm 0.78) \times 10^{8}$ ^{*7}	$(5.28 \pm 2.00) \times 10^{6}$ ^{*4}	1.00 ± 0.04 ^{*4}	38.9 ± 5.8 ^{*7}
Af (PLA)	$(7.60 \pm 4.15) \times 10^{5}$ ^{*7}			63.2 ± 11.3 ^{*3}
Bb (PLA)	$(4.99 \pm 2.67) \times 10^{7}$	$(8.34 \pm 4.41) \times 10^{5}$ ^{*4}	$(4.5 \pm 2.3) \times 10^{-3}$ ^{*4}	50.6 ± 7.6 ^{*6}
Bc (PLA)	$(4.43 \pm 4.16) \times 10^{8}$ ^{*7}	$(5.36 \pm 5.07) \times 10^{6}$ ^{*6}	$(6.1 \pm 2.3) \times 10^{-3}$ ^{*6}	49.5 ± 4.9 ^{*7}
Bf (PLA)	$(2.92 \pm 1.63) \times 10^{8}$	$(1.89 \pm 0.93) \times 10^{6}$ ^{*7}	0.02 ± 0.01 ^{*7}	35.4 ± 4.0 ^{*7}
Cb (PLA)	$(5.18 \pm 3.49) \times 10^{7}$			27.9 ± 5.7 ^{*7}
Cc (PLA)	$(4.09 \pm 1.49) \times 10^{7}$ ^{*7}	$(1.26 \pm 0.98) \times 10^{5}$ ^{*5}	$(1.7 \pm 1.5) \times 10^{-3}$ ^{*3}	31.2 ± 4.1 ^{*7}
Cf (PLA)	$(1.60 \pm 0.24) \times 10^{8}$	$(1.81 \pm 0.42) \times 10^{5}$ ^{*7}	$(8.7 \pm 2.8) \times 10^{-4}$ ^{*4}	28.1 ± 3.1
Ae (Nylon)	$(1.86 \pm 0.86) \times 10^{9}$	$(9.53 \pm 3.83) \times 10^{7}$	5.26 ± 2.50	129.4 ± 3.2

2.7.10.5 Extruder temperature

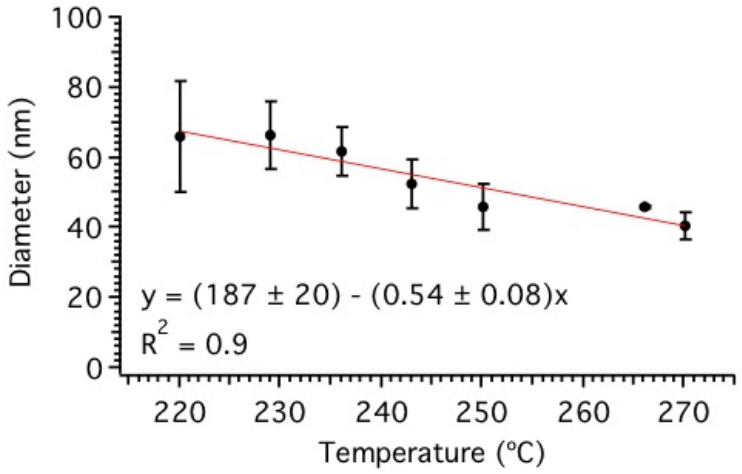

Figure 2.25 Average GMDs of particles over printing period for ABS filament *d* on printer *A* at various extruder temperatures. Error bars are standard error of the mean. A linear fitting is shown in the red line.

2.7.10.6 Build plate heating

The same object was printed using the same filament on printer *A* with build plate heating on and off with three replicates for each condition. For ABS brand *d*, the difference of average particle number yields between heating on and off was not statistically significant. However, the difference in GMDs averaged over the complete print job was significant ($p = 0.02$), with heating generating larger particles (GMD = 50 ± 1 nm) versus without heating (GMD = 44 ± 2 nm). Similarly, for ABS brand *a*, the difference between particle number emissions was not statistically significant while the difference between particle sizes was ($p = 0.01$), with GMD 57 ± 6 nm for heating and 39 ± 3 nm for not heating. Correspondingly, the mass yields increased 54% to 1.5 times compared to not heating for brand *d* and *a*. The effect of build plate heating for PLA filament brand *c* was minor; there was no difference for number yields or particle GMDs.

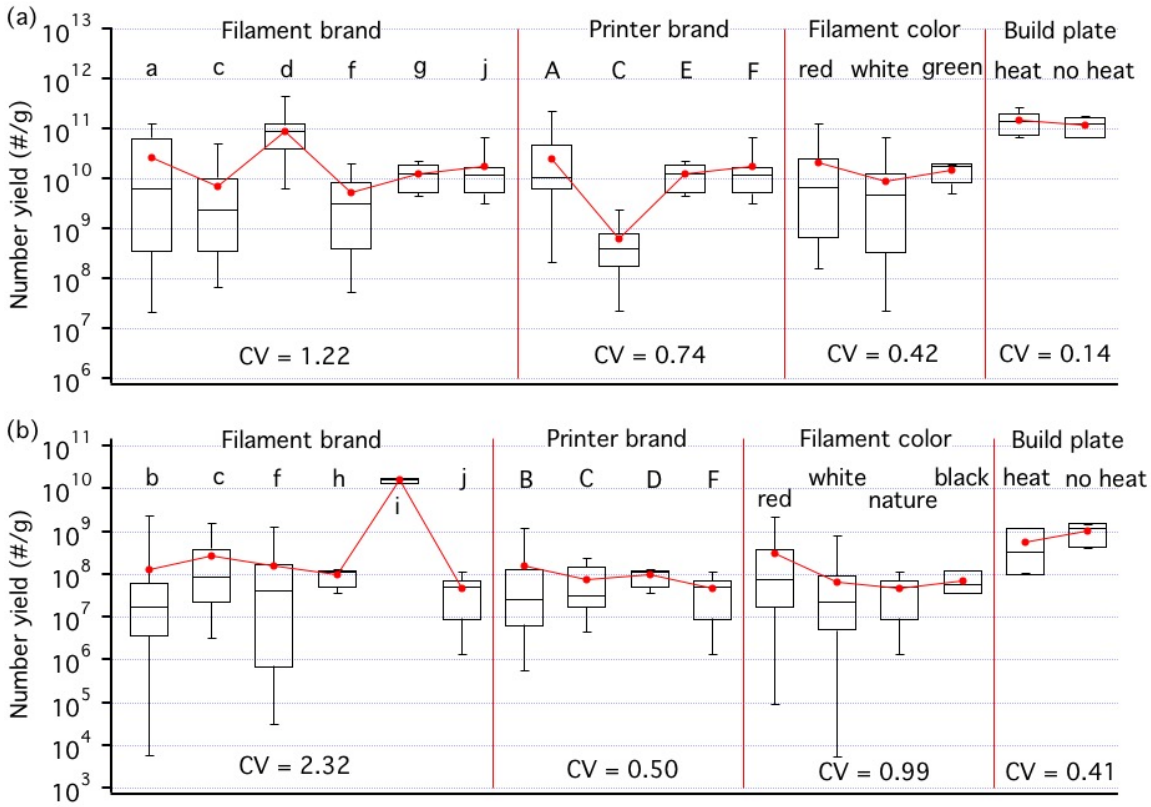

Figure 2.26 Summary of number yields for ABS (a) and PLA (b) grouping by different print conditions. Each box plot includes the data point for the corresponding condition, the line inside the box indicates the median, the top and bottom of the box indicates the 75% and 25% percentile, the top and bottom of the whisker indicates the maximum and minimum values. Each marker on top of the box plot is the mean of that data set. Coefficient of variance (CV) of each group is shown in values.

2.7.11 Suggestions for consideration in developing FDM 3D printer testing protocol

In order to compare various test results and to establish a standard testing method of consumer FDM 3D printer emissions, we suggest the following aspects to be considered:

- A 1 m^3 chamber of conducting material supplied with particle and vapor free air at 1 air change per hour is recommended. Room temperature and dry conditions

(low RH) within the chamber may serve as a standard environment. The performance of the chamber including air mixing and chamber leakage should be tested according to standards.

- Online particle measurement instrumentation are needed depending on research interest; instrumentation measuring size distributions for several nanometer to ~ 20 μm size range are recommend, which cover all potential particle sizes and give information of surface area and mass emissions as well (e.g., a combination of SMPS (7 – 300 nm) and OPC (0.3 – 25 μm). Total sample flow rate must not exceed inlet flow rate to the chamber (16.7 L/min for a 1 m^3 chamber and air exchange of 1 volume per hour).
- Printers to be tested should be located in the middle of the chamber; sampling tubes made of conducting materials connected into the chamber through sealable ports and located some distance from the walls (e.g., ~ 10 cm).
- Particle concentration sampling should include pre-print, print and post-print periods (see Section 2.3.4). Tests with printer malfunctions should be aborted and redone.
- Print time of 2-hrs is recommend to allow concentrations to reach steady state so that the emission is not dominated by the nucleation process at the beginning.
- Data analysis is suggested to follow BAM (2012) (see Section 2.7.5); yield should be reported as the total emissions (*TP*) divided by print object mass.
- 3 duplicates are recommended for each printer-filament combinations.

CHAPTER 3. INVESTIGATING PARTICLE EMISSIONS AND AEROSOL DYNAMICS FROM A CONSUMER FUSED DEPOSITION MODELING 3D PRINTER WITH A LOGNORMAL MOMENT AEROSOL MODEL

Qian Zhang, Girish Sharma, Jenny P. S. Wong, Aika Y. Davis, Marilyn S. Black, Pratim Biswas, Rodney J. Weber

Aerosol Sci. Technol.

DOI: 10.1080/02786826.2018.1464115

3.1 Abstract

Particle emissions from consumer fused deposition modeling 3D printers have been reported previously, however the complex processes leading to observed aerosols have not been investigated. We measured particle concentrations and size distributions between 7 nm and 25 μm emitted from a 3D printer under different conditions in an emission test chamber. The experimental data was combined with a moment lognormal aerosol dynamic model to better understand particle formation and subsequent evolution mechanisms. The model was based on particles being formed from nucleation of unknown semi-volatile compounds emitted from the heated filament during printing, which evolve due to condensation of emitted vapors and coagulation, all within a small volume near the printer extruder nozzle. The model captured observed steady state particle number size distribution parameters (total number, geometric mean diameter and

geometric standard deviation) with errors nominally within 20%. Model solutions provided a range of vapor generation rates, saturation vapor pressures and vapor condensation factors consistent with measured steady state particle concentrations and size distributions. Vapor generation rate was a crucial factor that was linked to printer extruder temperature and largely accounted for differences between filament material and brands. For the unknown condensing vapor species, saturation vapor pressures were in the range of 10^{-3} to 10^{-1} Pa. The model suggests particles could be removed by design of collection surfaces near the extruder tip.

3.2 Introduction

Fused deposition modeling (FDM) is the most common extrusion-based 3D printing technology in which a filament is heated to a semi-liquid state and deposited on a build plate in layers to construct a three-dimensional object (Zukas and Zukas 2015). FDM printers are popular with the general public due to their low-cost and ease of operation. These printers are found in small-scale manufacturing spaces, design offices, schools, libraries, and personal residences (Berman 2012; Gibson et al. 2010). It is known that commercial extrusion processing and degradation of thermoplastics produce both particles and volatile organic compounds (VOCs) (Adams et al. 1999), some of which are toxic (Yoon et al. 2010; Rutkowski and Levin 1986). Concerns over potential hazardous exposures from 3D printer emissions have been raised since some are used in spaces not designed for manufacturing. Most concerning is susceptible population exposure, such as children. These concerns follow a similar pattern to those relating to photocopier and laser printer emissions (Khatri et al. 2013a; Pirela et al. 2013). A number of studies have

characterized emissions of gases and particles from FDM 3D printers to help assess exposure levels.

Studies have shown that the types and concentrations of VOCs emitted are linked to filament material. For example, considering just major emissions, ABS (acrylonitrile butadiene styrene) filaments emit styrene and ethylbenzene, PLA (polylactic acid) filaments emit lactide and methyl-methacrylate, and nylon filaments emit caprolactam (Azimi et al. 2016; Steinle 2016). Stefaniak et al. (2017b) found that a 3D printer gave a much lower emission rate than laser printers tested in the same chamber. Analysis suggested that some VOC concentrations from 3D printers can exceed recommended exposure limits (Azimi et al. 2017), resulting in potential adverse respiratory effects (Chan et al. 2017).

For particles, previous studies have reported a wide range of particle emissions that depended on filament material, printer type and operating conditions. Some of the variability between studies was also due to differences in testing conditions, measurement approaches and emission calculation methods. Maximum particle number concentrations measured during printing ranged from 10^3 to 10^6 particles/cm^3 and depended on printer and filament properties (Stabile et al. 2017; Zontek et al. 2017; Azimi et al. 2016; Deng et al. 2016; Steinle 2016; Yi et al. 2016; Kim et al. 2015; Stephens et al. 2013). Emitted particles were often less than 100 nm in diameter (Stabile et al. 2017; Steinle 2016; Yi et al. 2016; Kim et al. 2015; Stephens et al. 2013). Average particle emission rates ranged from 10^7 to 10^{12} particles/min (Stabile et al. 2017; Azimi et al. 2016; Steinle 2016; Yi et al. 2016; Kim et al. 2015; Stephens et al. 2013), comparable to emissions from laser

printers (He et al. 2007), for which a standard test method and suggested emission thresholds have been developed (BAM 2012; UL 2014).

Zhang et al. (2017) discussed the potential aerosol dynamic processes leading to particle formation and the observed evolution of the particle size distributions from FDM 3D printing; Vance et al. (2017) also discussed the potential sources that might lead to particle formation based on their chemical analysis. However, the particle formation mechanism and processes involved have never been systematically investigated. Here we apply a method of moments model to simulate steady state particle concentrations recorded during printing. We perform a sensitivity analysis to investigate how each model parameter affects the number and size distribution of the emitted particles. Comparisons are then made between the steady state model solutions to data from specific printer runs to investigate the effect of extrusion nozzle temperature, filament brand (ABS from different manufacturers) and type of filament material (ABS vs. nylon) on the model parameters. The model provides conceptual insights on processes and factors leading to particle emissions from FDM 3D printers and to possible mitigation techniques.

3.3 Methods

3.3.1 Chamber experiment

Details of our systematic chamber measurements to characterize and identify the main variables affecting particle emissions from FDM 3D printers can be found in Zhang et al. (2017). In these studies, experiments were carried out using a 1 m^3 (1 × 1 × 1 m) stainless steel chamber with the printer in the center and sampling tubes extending

approximately 10 cm away from the chamber inner walls. Particle and VOC free air at room temperature (23 ± 1 ºC) and low relative humidity (3.0% ± 0.2%) was supplied to the chamber at an air exchange rate of 1 hr^{-1} (16.7 L/min). The design of the chamber and clean air supply system followed the criteria of ASTM standard D6670 (ASTM 2013), ECMA-328 standard (ECMA 2015) and UL GREENGUARD Certified method (UL 2014). The procedures to measure the air exchange rate and wall losses, and to evaluate the chamber airtightness and air mixing characteristics, also followed the above standards. Particles were measured from at least 15 min before print started until 2-hr after printing stopped. Aerosol measurement instrumentations included a condensation particle counter (CPC, TSI), a scanning mobility particle sizer (SMPS, TSI) and an optical particle counter (OPC, TSI) providing both total particle number concentrations and particle size distributions over the diameter range of 7 nm to 25 μm (7 – 300 nm for SMPS and 0.3 – 25 μm for OPC both with a time interval of 2 min).

Table 3.1 Specific print conditions for the selected tests.

Test notation	ABS(*a*)270	ABS(*d*)270	ABS(*d*)243	Nylon243
Material	ABS	ABS	ABS	Nylon
Filament brand	*a*	*d*	*d*	*e*
Filament color	Red	Red	Red	Natural
Extruder temperature	270°C	270°C	243°C	243°C

Four contrasting experimental results were chosen from a large number of emission tests (n = 231) (Zhang et al. 2017) for model analysis. Conditions for each test are shown in Table 3.1. The four tests were selected to cover factors that influence emissions: filament brand, extrusion temperature and filament material. In all cases the

filaments were 1.75 mm in diameter and all run on the same printer (printer *A* in) with a build plate temperature of 100 ºC and print time of ~ 7 hr printing the same object (a house). Although PLA is a commonly used material and its emissions have been reported (Zhang et al. 2017), it was not modeled in this study since particle concentrations from PLA never reached steady state during the printing periods on the tested printer. The method of moments model used is based on observed steady state concentrations.

3.3.2 Model description

The method of moments provides predictions of integrated particle characteristics with more computational efficiency than a fully coupled aerosol transport and dynamic model (Yu et al. 2008; Barrett and Webb 1998; Brock and Oates 1987; Frenklach and Harris 1986). An advantage is that it tracks the lower-order moments of the distribution without knowing the details of the distribution, which is accomplished by arranging the moment governing equations in a closed form (McGraw 1997) so that they can be solved by computationally efficient numerical techniques. Assumptions must be made to achieve closed forms (Hulburt and Katz 1964). Here we assumed a lognormal aerosol size distribution (Yu and Liu 2016), as the shape of the measured distributions were close to lognormal. This increases the computational efficiency, but is less accurate (Seigneur et al. 1986). A lognormal aerosol moment model is useful to predict poly-disperse particles properties in multi-dimensional multi-species aerosol flows (Brown et al. 2006). Our model is based on a lognormal moment method developed for simulating aerosol dynamics in aerosol reactors where the product aerosols are non-uniform (Pratsinis 1988; Pratsinis et al. 1986). This model has been shown to be able to capture the particle size distribution characteristics through comparisons to known exact solutions for certain

limiting cases. The method is applicable for modeling aerosol dynamics in complex systems when detailed particle distribution information is not required (Pratsinis 1988), which is the case for 3D printer particle emissions since the integral properties of the particles (i.e., total particle concentration and mean particle size) are important when considering emission levels and standards.

3.3.2.1 Control volume

The model was applied to a control volume where the vapors were emitted and aerosol dynamic processes of vapor nucleation resulting in new particle formation, vapor condensation onto existing particles and particle–particle interactions through coagulation were assumed to happen simultaneously. Outside of this control volume, it was assumed that the particles were simply diluted into the whole chamber domain without further aerosol dynamic processes occurring. Air was assumed to be advected through the control volume by the cooling fan attached to the printer extruder assembly.

The model assumed vapors are emitted from the hot filament, which includes the filament immediately exiting the extruder nozzle and the filament that was just recently deposited on the heated build plate or object being constructed. Therefore, the dimensions of the control volume were determined by the amount of filament recently extruded and expressed by a number of factors (Figure 3.1). The width (b) was arbitrary set at 0.1 cm, which was approximately the width of the filament being extruded from the nozzle. The length of the control volume (x) was the effective length of the extruded filament. In the following study, we set an arbitrary value (50 cm) to simplify the model (i.e., eliminate a variable). With a filament diameter of 0.1 cm and length of 50 cm, the bottom of the

control volume was 5 cm^2, which was modeled to consist of recently extruded filament that is emitting vapors (e.g., this would be equivalent to printing a 2.23 by 2.23 cm square plane that emits vapors at the bottom of the control volume). In addition, we assumed the vapor emissions to be constant, which was reasonable given the small area and time to print compared to the overall printing period (i.e., emissions not effected by print shape, cooling of filament, etc.). The height of the control volume (h_{av}) was calculated as a function of the length of the control volume and speed of air forced past the extruder tip by the cooling fan (see Section 3.8.1 for equations). The simulation time was the time for vapor molecules to diffuse from the build plate (or layers) to the upper boundary layer (see Section 3.8.1 for equations).

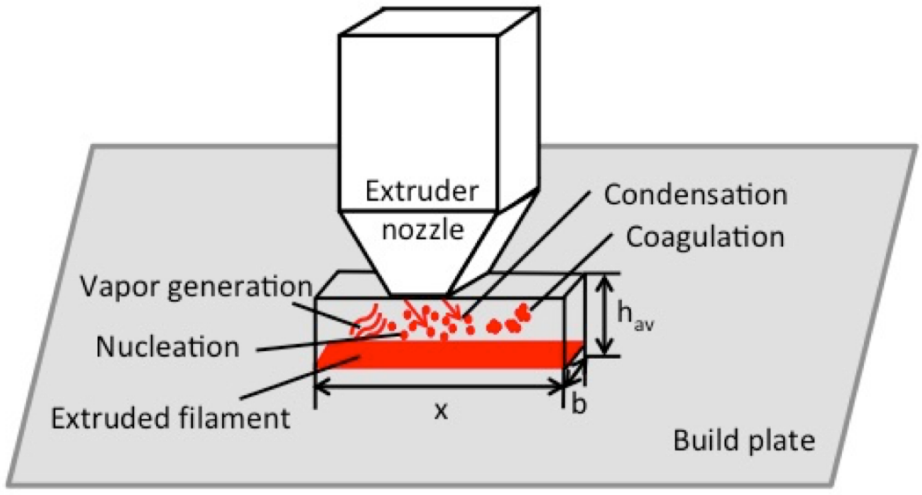

Figure 3.1 Schematic of the control volume located just below the 3D printer extrusion nozzle and aerosol dynamic processes that are modeled within the control volume. The variable *x* is the length of the control volume defined by the effective length of extruded filament; h_{av} is the height of the control volume; *b* is the width of the control volume, which is set at 1 mm.

3.3.2.2 The lognormal moment model

We focused on the particle formation and growth including nucleation, condensation/evaporation and coagulation within the control volume. The following simplifying assumptions were made: 1) There were no external processes at or across the boundaries of the control volume (Whitby and McMurry 1997). 2) Particle losses to the chamber surfaces were neglected since loss rates were factors of 10^{-4} – 10^{-2} the typical emission rates; the loss coefficients due to deposition on surfaces were generally less than 10^{-4} s^{-1} calculated from the post-printing exponential decay curves in chamber experiments, while the calculated average particle emission rates (*PER*s, see (Zhang et al. 2017) were 10^{7} to 10^{11} #/s. 3) Particles were chemically homogeneous and no chemical reactions that would change the vapor properties over time were considered; i.e., the semi-volatile gases that condense to form new particles or add mass to pre-existing particles were directly emitted from the heated filament, or if formed in the gas phase the reactions were rapid and the product concentrations directly proportional to emitted parent VOCs. 4) The temperature in the control volume was uniform, constant and equal to the average between the chamber (ambient) temperature and the extruder nozzle temperature.

In this study, the lognormal method of moments was used to solve the general dynamic equation (GDE) for aerosol processes, including new particle formation (NPF), particle growth by condensation (or shrinkage by evaporation) and coagulation (Friedlander 2000) by converting the GDE to closed form expressions for the moments (see Section 3.8.2 for details). The key parameters of a lognormal distribution (total number concentration (N), geometric mean diameter (D_{pg}) and geometric standard deviation (σ_g)) are related to the first three moments of the distribution. The governing

differential equations for the lognormal volume moment model were written in a dimensionless form in terms of moment change rates (Biswas 1989; Pratsinis 1988). Here we only show the key equations and parameters, detailed explanation of the equations and the variables can be found in Section 3.8.2.

The 0^{th} moment (i.e., total particle number concentration, N) is affected by nucleation and coagulation and its rate of change is

$$\frac{dN'}{d\theta} = I' - \xi N'^2 \tag{4}$$

where N' is the dimensionless particle number concentration (N); θ is the dimensionless residence time; I' is the dimensionless nucleation rate, which is related to saturation ratio ($S = P/P_s$, where P is the partial vapor pressure and P_s is the saturation vapor pressure at a given temperature); ξ is the dimensionless coagulation coefficient, which is related to identifiers of the particle size distributions (D_{pg} and σ_g).

The first moment (i.e., particle volume concentration) is affected by nucleation and condensation, and its rate of change is

$$\frac{dV}{d\theta} = I'k^* + f\eta(S-1)N' \tag{5}$$

where V is the dimensionless aerosol volume concentration; k^* is the number of monomers in the critical size nucleus; f is a condensation factor used to correct condensation coefficients for multiple-vapor effects; η is the dimensionless condensation coefficient and is related to particle size distributions.

The second aerosol volume moment is affected by nucleation, condensation and coagulation, and its rate of change is

$$\frac{dV_2}{d\theta} = I'k^{*2} + 2f\epsilon(S-1)V + 2\zeta V^2 \tag{6}$$

where V_2 is the dimensionless second aerosol volume moment; ϵ and ζ are the dimensionless condensation and coagulation coefficients (associated with particle size distributions).

A vapor monomer balance is necessary to solve the governing equations since nucleation and condensation both relate to the properties of vapors (P_s, R and f).

$$\frac{dS}{d\theta} = R' - I'k^* - f\eta(S-1)N' \tag{7}$$

where R' is the dimensionless form of vapor generation rate (R).

The differential equations Eq. (4 – 7) were solved using the VODE solver in Python. In this study, due to the complexity of vapor components in the control volume, and because the specific chemical species forming particles were unknown, it was difficult to predict the particle concentrations and size distributions from the initial conditions. Instead, the model can provide a possible range of parameters that could lead to the observed steady-state aerosol profiles, where particle number concentrations and size distributions remained relatively stable. In the following we report possible ranges of key parameters based on the model results and compare them between specific printer

runs. The goal is to provide insight on how particles are formed from consumer FDM 3D printers.

3.4 Results and Discussion

3.4.1 Experimental results from four contrasting printer runs

For the four different printer runs modeled in this study, the total particle number concentrations (N) and geometric mean diameters (D_{pg}) measured in the chamber during the printing period are shown in Figure 3.2. Only SMPS data (particle electrical mobility diameters between 7 nm and 0.3 μm) are shown and used in the model since large particles (OPC data) contributed less than 1% to the total particle number emissions (Figure 2.3). A general consistency was seen in the total particle concentration time trends for the four runs. At the beginning of the print (i.e., filament extrusion began), the particle concentrations jumped to the maximum ($2 \times 10^5 - 1 \times 10^6$ particles/cm^3) corresponding with the minimum D_{pg} (~ 20 nm). Total number concentrations then rapidly decreased while particle size increased. After ~ 30 minutes to 2 hrs of printing (depending mainly on filament material), the total number concentrations, as well as particle sizes, reached a steady state, and maintained relatively steady values until printing finished. Once finished, from then on there was an approximate exponential decay in particle number concentrations, mainly due to dilution by the continual addition of clean air into the chamber and some particle loss to surfaces. (Note the observed increase in mean size may be due to preferential loss of the smallest particles to surfaces and coagulation between small and large particles). Figure 3.2 and Table 3.2 show that ABS brand *d* produced the most particles with the smallest average size, when operated

under typical and reduced extrusion temperatures; with the lower extrusion temperature resulting in less total particle numbers, but of similar sizes. The less emitting ABS filament (*a*) produced smaller particle numbers, but of larger sizes. Nylon had even lower particle number emissions and larger mean sizes compared with ABS. These differences are believed to be driven by differences in the properties and concentration of the unknown condensable semi-volatile vapors emitted from the heated filament, which are dependent on the extrusion temperature and the filament composition itself, as would be expected if the vapor source is simply evaporation from the filament. These contracts can be explored with the model.

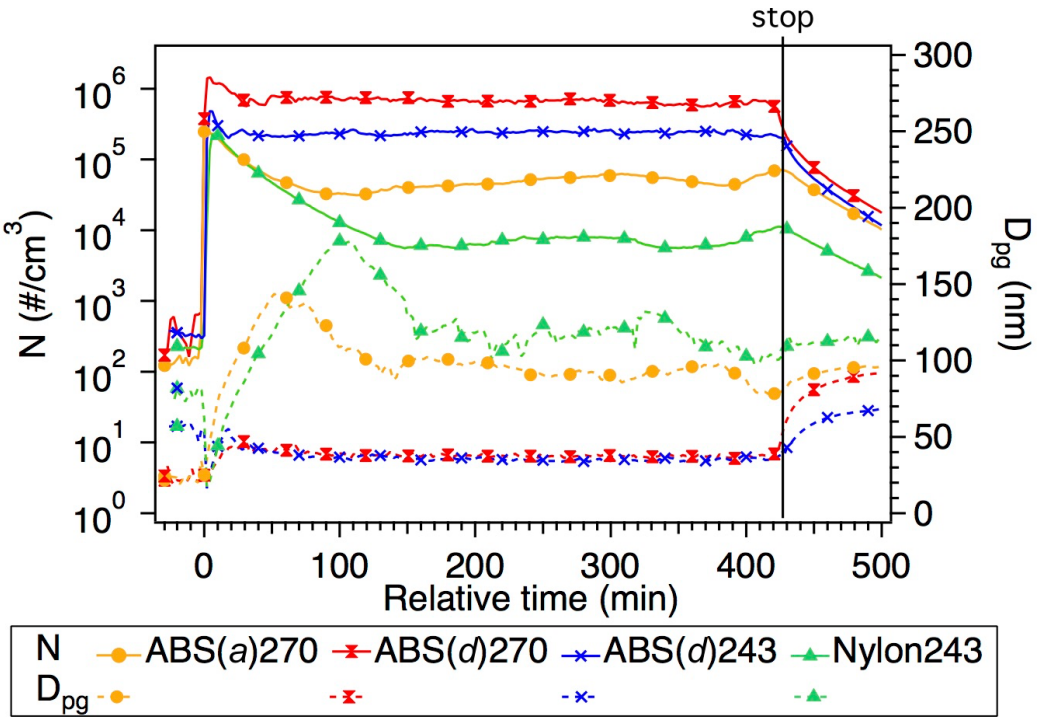

Figure 3.2 Total particle number concentrations (*N*) and geometric mean diameters (D_{pg}) measured in chamber experiments. Time zero on the x-axis indicates the beginning of the print run. The vertical line indicates the time when printing stopped. The notation is filament material (*filament brand*) extruder temperature.

Table 3.2 Measured steady state conditions and model simulation results.

	ABS(*a*)270[a]	ABS(*d*)270	ABS(*d*)243	Nylon243
Measurement at steady state				
N (#/cm^3)	4.92×10^4	6.97×10^5	2.39×10^5	7.65×10^3
D_{pg} (nm)	94.2	38.2	35.7	116
σ_g	2.04	2.03	2.22	1.93
Model simulations at steady state				
N (#/cm^3)	4.96×10^4	6.98×10^5	2.35×10^5	7.32×10^3
D_{pg} (nm)	84.8	38.2	36.4	118
σ_g	1.87	2.34	2.18	1.54
Error (%) = (model – measurement)/measurement × 100%				
N (#/cm^3)	0.84	0.16	-2.01	-4.39
D_{pg} (nm)	-10.0	0.10	1.95	1.99
σ_g	-8.16	15.2	-2.02	-20.2
Model results				
P_s (Pa)	0.001	0.1	0.1	0.01
R (#/m^3/s)	3.24×10^{22}	1.85×10^{23}	3.42×10^{22}	5.64×10^{21}
f	0.75	0.01	0.01	0.14

[a] Notation is filament material (*filament brand*) extruder temperature.

Figure 3.3 shows the average particle size distributions during the steady-state period, and their corresponding lognormal fits. It can be seen that the particle size distributions were generally lognormal.

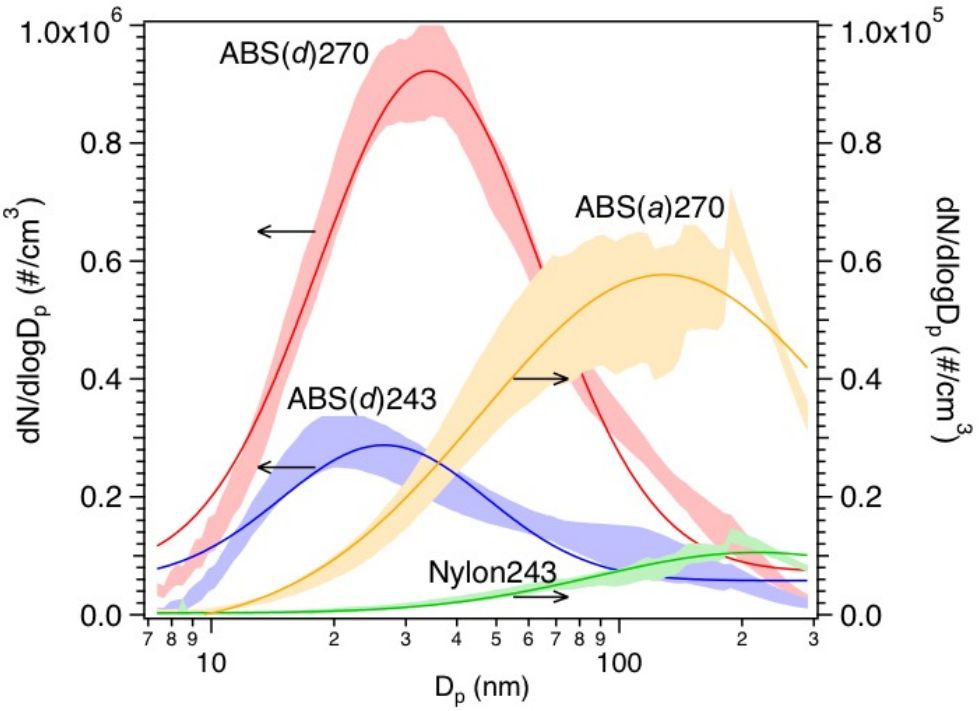

Figure 3.3 Average particle size distributions at steady state, the shaded areas are the mean values with one standard deviation; the lines are the corresponding lognormal fittings. The notation is filament material (filament brand) extruder temperature. ABS(*d*)270 and ABS(*d*)243 refer to the left y-axis, the rests refer to the right y-axis.

From these observed particle emission time series trends, the following dynamic processes appear to be involved in the production of aerosols. The observed initial burst of small particles as printing starts, when few particles existed in the chamber or the control volume (total particle concentration < 700 particles/cm^3), is consistent with NPF of some fraction of the emitted vapors. These condensing vapors, referred to here as semi-volatile compounds (SVCs) might be semi-volatile organic compounds (SVOCs) or other compounds associated with the bulk polymer or trace additives in the filament. SVC supersaturated conditions leading to NPF could be reached in the control volume at the beginning of the printing due to vapor emissions with little loss onto pre-existing

particles and cooling as the air moves away from the hot filament (Warren and Seinfeld 1984).

Once NPF has occurred and particles are present in the control volume, the SVCs continually being emitted during printing can be lost by condensation onto the pre-existing particles. This would lower supersaturation levels, lowering NPF rates, or even ending it. With lower NPF rates, total particle concentrations would decrease, as seen in the time series following the initial NPF burst (Figure 3.2). At the same time, in the control volume particles become larger due to condensation and particle coagulation. All the while dilution is occurring due to background air in the chamber being forced through the control volume. At some point these processes produce steady-state aerosol size distributions in the overall chamber.

At steady state, the processes that decrease particle number concentration (i.e., coagulation, dilution and deposition) balance with NPF that increases particle number concentration. At the same time, the processes that increase particle size (i.e., condensation and coagulation) balance with NPF that produces smaller size particles. This view of processes is consistent with differences observed in the four contrasting printer runs shown in Figure 3.2, resulting from differences in the emitted SVC concentrations and properties. Factors that contribute to the contrasting observations are explored with the model.

PLA is a commonly used filament, but not modeled here since it had a very different profile. An example is shown in Figure 3.6. In general, the steady state condition was seldom observed for PLA. This might be because PLA filaments tend to be

heated to lower temperatures than many other filament materials (210 °C) and may produce SVCs that are less likely to condense. (In one case, PLA with an additive (Zhang et al. 2017) did produce significant particles, indicating that additives versus the bulk filament material can affect particle emissions).

3.4.2 Model results

Based on the governing equations, the steady state particle number concentration and size distribution are interrelated to the properties of the vapors that condense (i.e., SVCs), including vapor generation rate (R), saturation vapor pressure (P_s) and the condensation factor (f). Parameters related to coagulation were not specifically quantified since they were coupled within the differential equations. Model input parameters included R, f, T, P_s and x, outputs were the lognormal particle size distribution parameters N, D_{pg} and σ_g. To estimate the steady state conditions, the effective length of the control volume (x) was set at 50 cm and temperature as the average of the printer extruder and chamber temperatures. Because the properties of actual condensational vapors were unknown, exact solutions for particle concentrations cannot be obtained with the model. Instead we derived a range of solutions by changing one variable at a time while holding the other variables constant. The modeled steady state results were then compared with the observation data. For each printer run, the best-fit solution was selected and the results are discussed below. Best fit was defined as when differences in the model outputs and experimental data were minimized; i.e., the average of the absolute values of the errors of the steady state particle distribution characteristics (N, D_{pg} and σ_g) was minimum. There was generally a single best solution for each printer run (see Section 3.8.4.1 for details), we also investigated the solution with a slightly higher average error,

but do not present the results here. The simulation results and errors are shown in Table 3.2. In general, the model simulation was able to capture the particle characteristics at steady state; the absolute errors were low, < 5% for N, < 10% for D_{pg} and < 21% for σ_g, indicating that the model can reasonably simulate the aerosol dynamic processes that produce particles from the FDM 3D printer we tested.

3.4.2.1 Sensitivity analysis: Parameters that affect particle emissions

A sensitivity analysis was used to explore how the model free parameters, R, f and P_s, are related to predicted properties of the steady state size distributions. These results were not linked to any specific filament or printer operating conditions, except that the extruder nozzle temperature was 270 °C. In this analysis one parameter was varied while the other two were held fixed. Considering the computational demand, the sensitivity analysis was not carried out over all possible values in the ranges for every parameter, but was limited to selected values (see Section 3.8.4.2). The summarized results are shown in Figure 3.4, detailed figures can be found in Section 3.8.4.2. The temperature was 420 K and the effective length was 50 cm; the dependent variables were steady state N, D_{pg} and σ_g.

Saturation vapor pressure: Saturation vapor pressure (P_s) is related to particle formation since nucleation happens under supersaturated conditions (i.e., $S = P/P_s > 1$, where P is the vapor concentration). P_s is a property of the condensing vapors (SVCs); SVCs with lower P_s (at a given temperature) will result in higher vapor saturation ratios (S). P_s in our cases was evaluated to be in the range of 10^{-3} – 10^{-1} Pa, in order to match the observed steady state particle characteristics. In Figure 3.4a, as P_s decreased from 10^{-2}

Pa to 10^{-3} Pa, the steady state N increased, which is consistent with NPF rates increasing with S, (i.e., lower P_s, with R and f fixed). As NPF is favored for lower P_s, the newly formed small particles drive the size distributions toward smaller average sizes (decrease in D_{pg}) and more spread in the distribution (increase in σ_g) (Figure 3.4a). (Note that coagulation will also affect the growth process and the width of the distribution). S is related to both P_s and the concentration of condensing vapor, P, which will be related to the vapor loss rate by condensation (f) and generation rate R.

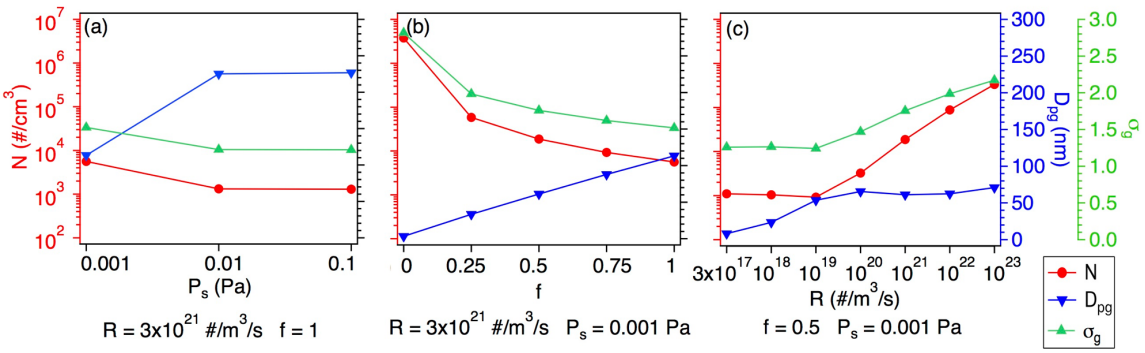

Figure 3.4 Sensitivity analysis on how particle concentrations and properties of the lognormal distribution depend on condensing vapor properties. The plots show the simulated steady state particle concentrations (N), geometric mean diameters (D_{pg}) and geometric standard deviations (σ_g) of lognormal size distributions as a function of (a) saturation vapor pressure (P_s), (b) vapor condensation factor (f) and (c) vapor generation rate (R). For every parameter evaluated, the controlled conditions are shown below the graphs.

Condensation factor: The condensation factor accounts for the possibility that multiple vapor species might be condensing onto pre-existing particles, since the identity of the SVC condensing during 3D printing is unknown. The condensation factor ranges from 0 to 1, with 0 indicating no condensation and 1 meaning that all the vapors will condense. Thus f represents the integrated property for all condensing species and a lower f favors NPF over condensation since it would lead to high vapor levels (P). Figure 3.4b

shows the simulation results for multiple f values. As f approaches 0, i.e., decreasing condensation, implying more NPF, the total particle concentration increases and the particles are smaller in size as NPF dominates. On the contrary, if more SVCs condense on existing particles (higher f), NPF rates will decrease, fewer particles will be formed and the added condensation results in larger particles (higher D_{pg}). The distribution also narrows (smaller σ_g), since condensation tends to produce more monodisperse distributions (Tsang et al. 1990).

Vapor generation rate: Vapor generation rate (R) represents the number of condensable molecules (SVCs) generated from the heated filament and is expected to be related to filament temperature. As shown in Figure 3.4c, there is an inflection point at $R = 3 \times 10^{19}$ #/m^3/s. For R below this value, an increasing R has little effect on the total number of particles produced, but once this threshold is passed, increasing R results in increasing N; indicating that the inflection point of R represents a critical SVC emission rate at which NPF begins (Figure 3.4c) (note, the inflection point is for a given f and P_s, and will change for different f and P_s combinations). At R below this point, the pre-existing particles grow in size (D_{pg} increases with R), but the distribution shape changes little (σ_g slightly decreases). The narrowing of size distributions by condensation is in some extent compensated by coagulation, which tends to make σ_g move toward a value of 1.32 (Hinds 1999), coagulation is also indicated by the slightly decrease of N in Figure 3.4c. Once R exceeds the critical value and NPF occurs, N increases, D_{pg} does not change significantly, pre-existing particles increasing in size and small particles added to the distribution, leading to fairly steady D_{pg} but larger σ_g (Figure 3.4c).

3.4.2.2 Model simulations compared to specific printer runs

Examples of model-predicted parameters for the best solutions (smallest average error) for the four printer runs are now compared. The comparisons are: 1) Same ABS filament run at different extruder tip temperatures, comparing effect of extruder temperature. 2) A high particle emitting ABS filament vs. a regular emitting ABS filament at the same extruder temperature, comparing filament manufacturer brands (or the effect of unknown additives). 3) ABS vs. nylon filament at the same extruder temperature, comparing bulk filament material. The measured particle steady state conditions (N, D_{pg}, σ_g) and model parameters (P_s, R, and f) for these comparisons are summarized in Table 3.2 and Figure 3.5.

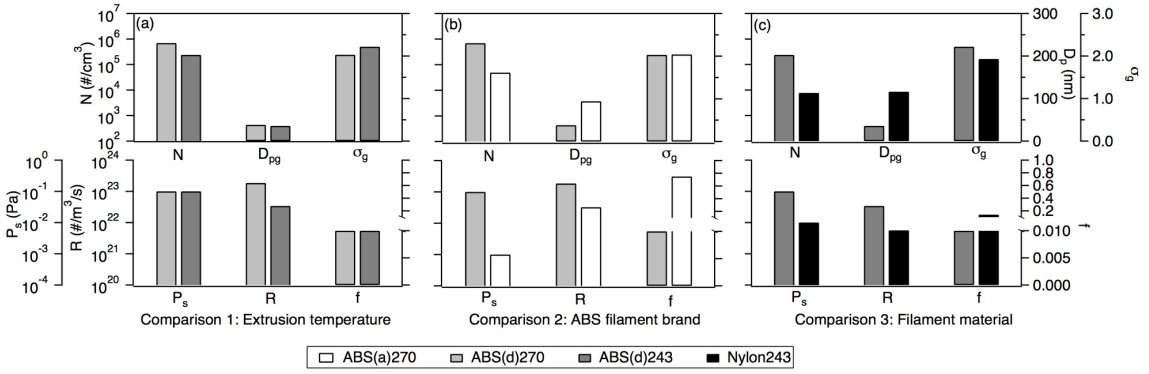

Figure 3.5 Observed steady state particle size characteristics (N, D_{pg}, σ_g in upper panel) and model simulated condensing vapor properties (P_s, R, f in lower panel), grouped by 3 sets of comparisons. (a) compares extrusion temperature of the same filament; (b) compares ABS filament brands run at the same condition; (c) compares ABS and nylon materials run at the same condition.

Comparison 1. Extruder tip temperature: For the same filament operated at different extrusion temperatures, the main difference was that the higher temperature produced more particles (larger N), but the size distribution was similar (differences of D_{pg} and σ_g within 10% whereas N was about 3 times higher) (Table 3.2 and Figure 3.5a). The main effect of a higher filament temperature was a higher emission rate of the

condensing vapors (R) (~ 5 times higher). Since the same filament was used, the properties of the condensing vapors should be similar, as was found for the model parameters; P_s and f were similar in both cases (Figure 3.5a).

Comparison 2. High vs. regular emitting ABS brands: The high emitting ABS (brand *d*) produced more particles of smaller sizes than the regular ABS (brand *a*), but with similar spread in the distribution (σ_g) (Table 3.2 and Figure 3.5b). These differences could be reproduced in the model by the high emitting ABS having a higher saturation vapor pressure (P_s), higher vapor generation rate (R) and lower condensation factor (f) (Figure 3.5b and Table 3.2). Higher P_s for the high emitting ABS is somewhat surprising since this lowers the saturation ratio ($S = P/P_s$), the driving force for NPF and condensation. One would expect S to be higher for the high emitting ABS filament since it produces a greater number of particles. However, the higher vapor emission rate (R) could compensate for this by leading to higher vapor concentrations (P), which increases S. A lower f also means that the vapor condensation route onto pre-existing particles is slower for the high emitting ABS, implying that P and S could reach higher levels since the condensational sink was impeded, which would increase the NPF rate (NPF is very sensitive to S). This would result in more particles of smaller sizes, as observed. Difference in P_s between these two ABS filament brands implies that the compounds forming the particles differ, consistent with the view that some unknown additives in the filament are responsible for the different particle emissions observed.

Comparison 3. ABS vs. nylon material: Similar to the above comparison, ABS produced substantially more particles than nylon filament, but particle mean size was smaller and the distribution broader. Relative differences in model-predicted vapor

properties were also similar to the above comparison (i.e., compare Figure 3.5b and c). Both R and P_s for ABS were higher. Thus as above, high saturation levels ($S = P/P_s$) could be driven by the higher vapor concentrations (P), which were offset to some extent by high saturation vapor pressures (P_s). Again a lower condensation factor can enhance NPF and impede particle growth, leading to smaller mean particle sizes.

Overall, the model results indicate that known aerosol dynamic processes occurring very near the extruder nozzle can reasonably explain the observed steady state aerosol emissions produced by an FDM 3D printer, though the interplay between the variables is complex. In the above analysis we only compared model solution that gave the minimum errors. Comparing other solutions that gave larger average errors than the best fits tends to show that P_s plays a less distinct role than the SVC emission rate (R), i.e., the NPF process is largely driven by vapor concentration than saturation vapor pressure. The condensation factor also has effects on N and largely controls particle sizes. These results further emphasize the role of extrusion temperature on overall particle emissions.

3.5 Implications

The model simulations verified that particles can be formed from vapors emitted by the heated filaments and grow by vapor condensation and particle coagulation. The precursor vapors have very low saturation vapor pressures that can span a wide range (10^{-3} to 10^{-1} Pa). These are similar saturation vapor pressures to those found for NPF in chamber studies of secondary organic aerosols (SOA) formation, where P_s can range between 10^{-12} – 1 Pa (Tobias and Ziemann 2000; Tao and McMurry 1989) based on

model estimates and 10^{-5} – 10^{-2} Pa based on measurements (Bilde and Pandis 2001; Pankow et al. 2001; Seinfeld et al. 2001). Similar to the model results, chamber SOA P_s associated with NPF also span large ranges.

The saturation vapor pressures of the VOCs sampled in the emission test chamber are many orders of magnitude higher than those that form particles. Many of the VOCs measured in chambers are similar to components that comprise the bulk filament material. For example, styrene, the most abundant VOC detected for ABS filament (Azimi et al. 2016; Steinle 2016), has a saturation vapor pressure of ~ 10^3 Pa at 25 ºC (Chao et al. 1983) and the estimated partial pressure in the chamber was on the order of 10^{-2} Pa, conditions far from saturated ($S \sim 10^{-5}$). Other detected VOCs from ABS (e.g. ethyl benzene, methylene chloride, acetaldehyde) all have saturation vapor pressures larger than 10^3 Pa at room temperature and so would not contribute to the aerosols formed. The major VOC detected from nylon, caprolactam, has a P_s of 0.25 Pa at 25 ºC, which is the closest to what the model predicted, though at a lower temperature (U.S. EPA 1988).

Chemical analysis of the particles can provide insight on the condensing species. Measurements of 3D printer emitted particles with an Aerosol Chemical Speciation Monitor (ACSM, Ng et al. 2011) showed that the mass spectrum of particles emitted from ABS have no pattern similar to spectra expected for any ABS monomers (i.e. acrylonitrile, 1,3-butadiene and styrene), based on spectra from NIST Chemistry WebBook (Stein 2016). In addition, pyrolysis gas chromatographic mass spectral analysis showed that raw ABS filament had fragments of ABS monomers, while particles formed from a 3D printer running that ABS filament collected on a filter, and subsequently

analyzed in the same way as the filament, did not contain these fragments. This is consistent with the Raman spectra results from Vance et al. (2017). Instead, particle spectrum showed major components thought to be associated with filament additives, such as fatty acids. Therefore, for ABS, the particles are not formed from the bulk ABS material, but some unknown additives that account for a very small fraction of the filament. As noted in material safety data sheets provided by manufacturers, ABS filaments are composed of 90% – 100% of thermoplastics polymers, with the rest as N,N'-Ethylenebis stearamide, typical antioxidants and pigments. Plasticizers like phthalates have saturation vapor pressure of 10^{-7} – 10^{-2} Pa at ambient temperature (Wu et al. 2016), organic dyes such as 1-aminoanthraquinone and 4-nitro-4'-aminoazobenzene derivatives have saturation vapor pressure of 10^{-4} – 10^{-2} Pa at temperature of 120 – 165 ºC (Bradley et al. 1960), both might be potential sources of SVCs. Inorganic compounds including metals commonly used in dyes and pigments may also be a potential source of SVCs; it was found that metallic aerosols were formed from metal associated vapor precursors during combustion (Wang and Biswas 2000; Wu and Biswas 2000; Biswas et al. 1992, 1997; Sethi and Biswas 1990), and metals like Na, Al and transition metals like Fe, Cr, Ni were found in the particles emitted from ABS and PLA (Stefaniak et al. 2017b; Zontek et al. 2017; Steinle 2016).

As noted, we found that the vapor generation rate, R, was a critical parameter accounting for differences between observed steady state total particle number concentrations when contrasting filament types and brands. For example, unlike P_s (r^2 = 0.64) and f (r^2 = 0.28), a higher correlation was found between measured N and model-predicted R (r^2 = 0.96), for the four experiments discussed above. When expanding the

comparison to all model runs having solutions with average errors between model and measured N, D_{pg}, σ_g less than 10% (n = 38), only simulated N and R was correlated (r^2 = 0.90) (see Section 3.8.4.3). Since we have shown a linkage between R and extruder temperature, the model results support the view that nozzle (or filament) temperature is a critical parameter affecting total aerosol emissions. This has been noted by other investigators (Stabile et al. 2017; Zhang et al. 2017; Deng et al. 2016) and is reinforced by our modeling results.

Since 3D printing can emit large numbers of potentially toxic particles, designing printers with the aim to reduce emissions would be beneficial. One approach would be to reduce the particle formation at the source. Since particles are formed from SVCs emitted from the heated filament, and the emissions increase with extrusion temperature, a mitigation strategy is to reduce the extrusion temperature, as has been noted. However, the filament must be heated to a certain level to be extruded from the nozzle and produce a print object of sufficient quality. Identifying and removing filament additives that form particles would also be a viable approach, but would require extensive tests since the specific chemicals forming aerosols are unknown at this time.

An alternative is to remove the generated particles. A sealed enclosure with an effective filtration system can reduce overall particle emissions to some extent (Azimi et al. 2016, 2017), but has implications on the size and complexity of the printer and how it is operated. This modeling work shows that the particles are formed near the extruder nozzle and then dispersed by the extruder cooling fan. A potential mitigation method would be to collect the extremely small and highly mobile newly formed particles near the extruder nozzle before they substantially grow in size and are advected into the

surroundings. Collection of particles to a surface by diffusion and thermophoretic forces may prove to be effective. For example, the distance particles with diameters of 3 – 50 nm travel in 1 second by diffusion is in range of 1.2 mm (3 nm particles) to 0.07 mm (50 nm particles) and by thermophoresis with a temperature gradient of 247 K/0.01 m the distance is ~ 1 mm for particle less than about 50 nm (temperature gradient due to difference in nozzle and ambient air temperature, see Section 3.8.5 for details). Thermophoretic force might affect the particle tracks (Kommu et al. 2004) and previous model results showed ~ 40% increase in aerosol diffusional deposition rates onto surfaces when considering thermophoresis at high temperature (Bai and Biswas 1990). This indicates the small aerosols (e.g., < 50 nm) might be collected by a combination of diffusion and thermophoresis before they grow and are advected out of the control volume. Modification of the forced air nozzle cooling system may be necessary. In addition, the model result that all aerosol dynamic processes happen within a small area close to the extruder nozzle and extruded filament provided insight when considering exposures in an indoor environment (e.g., proximity to the printer). For example, the particle size distributions (e.g., mean size) are not expected to significantly change for different locations within a room (assuming the printer is the only source), since particles are only diluted as they disperse to the surroundings, causing a uniform decrease in concentration for particles of all sizes.

3.6 Conclusions

We used a lognormal moment model to study the aerosol dynamic processes of particles formed from a FDM 3D printer. The model was based on the theory that particles are formed from nucleation of semi-volatile vapors emitted from the heated

filament, and then grow by vapor condensation and particle coagulation, all of which occur within a small control volume near the printer extruder nozzle. These dynamic processes are interrelated and depend on a number of key properties of the condensing vapors, including vapor emission rate, saturation vapor pressure and a condensation factor. Because the specific vapors emitted by the heated filament that undergo gas-to-particle conversion are unknown, the model could not be solved in a closed form. Instead ranges of solutions of the noted variables leading to the observed steady state particle size distribution characteristics (total particle number concentration, geometric mean diameter and geometric standard deviation) were found. Operating conditions, like filament material, filament brand and extrusion temperature influenced the steady state particle characteristics and could be related to the differences in the model predicted properties. The combined effects of multiple aerosol dynamic processes, which can be represented by emission rates and properties of condensable vapors, govern the particle emissions from FDM 3D printers. Vapor emission rate from the filament was a key parameter and linked to the printer extruder (filament) temperature. Possible mitigation strategies involving removing the newly formed small particle near the extruder nozzle are also suggested by the model results.

3.7 Funding

The authors acknowledge funding from the Chemical Safety Research Program of Underwriters Laboratories Inc.

3.8 Supplemental Information

3.8.1 Model control volume

As shown in Figure 3.1, for x filament extruded on the build plate (or the surface that newly extruded filament was deposit on), the boundary layer thickness (h), defined as the distance from the build plate (or built layers) to the point where the air flow velocity is 99% of the free stream velocity was calculated using Eq. (8) based on Blasius Equation.

$$h = \frac{5}{\sqrt{Re}}x \tag{8}$$

where Re is the Reynolds number and calculated by $Re = \rho_g u x/\mu$, where ρ_g is the density of air; u is the velocity of the air calculated from the extruder cooling fan speed; μ is the viscosity of air.

Therefore, the average boundary layer height (h_{av}) was calculated by integrating h over the entire length (x) and determines the height of the control volume.

$$h_{av} = \frac{10}{3}\sqrt{\frac{\mu x}{\rho_g u}} \tag{9}$$

Once air was advected out of the control volume, only dilution was considered. The dilution ratio (DR) was determined as the ratio of the chamber overall volume to the control volume:

$$DR = \frac{1}{h_{av} b x} = \frac{3}{10b}\sqrt{\frac{\rho_g u}{\mu}}x^{-\frac{3}{2}} \tag{10}$$

The simulations were run over a time interval of t_{sim}, which was the time for vapor molecules to diffuse from the build plate (or layers) to the upper boundary layer (h_{av}):

$$t_{sim} = \frac{{h_{av}}^2}{2D} \tag{11}$$

where D is the vapor diffusion coefficient.

3.8.2 Lognormal moment model

The general dynamic equation (GDE) for aerosol processes, including new particle formation (NPF), particle growth by condensation (or shrinkage by evaporation) and coagulation is (Friedlander 2000):

$$\frac{\partial N}{\partial t} + \frac{\partial (GN)}{\partial v} - I(v^*)\delta(v - v^*) = \frac{1}{2}\int_0^v \mathrm{B}(v - \bar{v}, \bar{v}) N(v - \bar{v}) N(\bar{v}) d\bar{v} - \int_0^\infty \mathrm{B}(v, \bar{v})\, N(v)\, N(\bar{v}) d\bar{v} \tag{12}$$

The first term on the left-hand side (LHS) is the rate of change of particle number concentration for particle volume of v to $v+dv$ at time t; the second term on the LHS is the gain or loss of particles by condensation or evaporation, which is a function of the aerosol growth rate (G); the third term on the LHS represents NPF determined by the nucleation rate (I) and the critical size (volume) of the newly formed particles (v^*). The two terms on the right-hand side (RHS) represent the gain and loss of particles due to Brownian coagulation of particles having volume of v and $\bar{v}$, which are determined by the collision frequency function (B) and particle number concentrations (N).

The geometric mean volume (v_g) and geometric standard deviation (σ_g) of a lognormal particle distribution can be expressed in terms of the first three moments (M_0, M_1, M_2) of the distribution:

$$v_g = \frac{M_1^2}{M_0^{3/2} M_2^{1/2}} \tag{13}$$

$$ln^2 \sigma_g = \frac{1}{9} ln\left(\frac{M_0 M_2}{M_1^2}\right) \tag{14}$$

The kth volume moment of a particle size distribution is defined as (i.e., kth order of particle volume lognormal distribution):

$$M_k(t) = \int_0^\infty v^k N(v,t)\, dv \tag{15}$$

where $N(v, t)$ is the particle number distribution of particles having volume of v to $v+dv$ at time t.

The change rate of the kth volume moment was derived by multiplying both sides of Eq. (12) by v^k and integrating over all the particle sizes after determining G and B (Randolph and Larson 1971). In order to solve the GDE, the related parameter functions were determined based on the conditions and properties of both particles and vapors (monomers). The condensation and coagulation coefficients were the harmonic average of coefficients in the free molecular and continuum regimes (it was verified that the harmonic average approximation of coefficients matched at both free molecular and continuum regimes limits and followed the Fuchs-Sutugin approximation in the transition

regime (Pratsinis 1988)). Further, the governing equations for the lognormal moment model were written in a dimensionless form in terms of moment change rates (Pratsinis 1988).

The zeroth moment (M_0, i.e., total particle number concentration, N) is affected by nucleation and coagulation and its rate of change is:

$$\frac{dN'}{d\theta} = I' - \xi N'^2 \tag{16}$$

On the LHS, N' is the dimensionless particle number concentration ($N'=M_0/n_s$, n_s is monomer concentration at saturation); θ is the dimensionless residence time ($\theta = t/\tau$, t is the residence time; τ is the characteristic time for particle growth, and $\tau = [n_s s_1(k_B T/2\pi m_1)^{1/2}]^{-1}$, where s_1 is the monomer surface area; k_B is the Boltzmann's constant, T is the average temperature of extruder tip and ambient air in the chamber; m_1 is the monomer mass). The first term on the RHS is the dimensionless nucleation rate and $I' = I/(n_s/\tau)$, where the nucleation rate (I) is

$$I = n_s^2 s_1 (k_B T/2\pi m_1)^{1/2} S^2 (2/9\pi)^{1/3} \times \Sigma^{1/2} \exp\left(-\frac{k^* \ln S}{2}\right) \tag{17}$$

where S is the saturation ratio ($S = n_1/n_s$ or $S = P/P_s$, where n_1 is monomer concentration, P is the partial vapor pressure and n_s or P_s is the saturation monomer number concentration or vapor pressure at a given temperature); Σ is the dimensionless surface tension ($\Sigma = \gamma v_1^{2/3}/(k_B T)$, where γ is the surface energy; v_1 is monomer volume); k^* is the number of monomers in the critical size nucleus. The second RHS term in Eq. (16) represents coagulation, where ξ is the dimensionless coagulation coefficient; the

coefficients of free molecular regime (ξ_{FM}) and continuum regime (ξ_C) are listed in Table 3.3.

The first moment (M_1, particle volume concentration) is affected by nucleation and condensation, and its rate of change is

$$\frac{dV}{d\theta} = I'k^* + f\eta(S-1)N' \tag{18}$$

where V is the dimensionless aerosol volume concentration ($V = M_1/n_s v_1$); f is a condensation factor used to correct condensation coefficients for multiple-vapor effects; η is the dimensionless condensation coefficient. The coefficients for the free molecular regime (η_{FM}) and continuum regime (η_C) are in Table 3.3.

The second aerosol volume moment (M_2) is affected by nucleation, condensation and coagulation, and its rate of change is

$$\frac{dV_2}{d\theta} = I'k^{*2} + 2f\epsilon(S-1)V + 2\zeta V^2 \tag{19}$$

where V_2 is the dimensionless second aerosol volume moment, $V_2 = M_2/n_s v_1^2$; ϵ and ζ are the dimensionless condensation and coagulation coefficients, the coefficients for the free molecule regime (ϵ_{FM}, ζ_{FM}) and continuum regime (ϵ_C, ζ_C) are in Table 3.3.

In addition, a monomer balance is necessary to solve the governing equations since nucleation and condensation/evaporation are all related to the saturation conditions.

$$\frac{dS}{d\theta} = R' - I'k^* - f\eta(S-1)N' \tag{20}$$

where *R'* is the dimensionless vapor generation rate, and $R' = R/(n_s/\tau)$, where R is the vapor generation rate and assumed to be constant.

Table 3.3 Dimensionless coagulation and condensation coefficients in free molecular and continuum regimes.

Parameter	Free molecular regime	Continuum regime
Coagulation coefficient for 0^{th} moment	$\xi_{FM} = r_g'^{1/2} b_0 \left[\exp\left(\frac{25}{8}\ln^2\sigma_g\right) + 2\exp\left(\frac{5}{8}\ln^2\sigma_g\right) + \exp\left(\frac{1}{8}\ln^2\sigma_g\right)\right]$ (21)	$\xi_C = K\left[1 + \exp\left(\ln^2\sigma_g\right) + 1.257\left(Kn_1/r_g'\right)\times \exp\left(\frac{1}{2}\ln^2\sigma_g\right)\left(1 + \exp\left(2\ln^2\sigma_g\right)\right)\right]$ (22)
	r_g' is dimensionless particle geometric mean radius, $r_g' = r_g/r_1$, where r_1 is monomer radius; $b_0 = 0.633 + 0.092\sigma_g^2 - 0.022\sigma_g^3$ (Lee et al. 1984).	K is coagulation coefficient and $K = 2k_B T n_s \tau/3\mu$, where Kn_1 is monomer Knudsen number and $Kn_1 = \lambda/r_1$, where λ is mean free path.
Condensation coefficient for 1^{st} moment	$\eta_{FM} = v_g'^{2/3}\exp\left(2\ln^2\sigma_g\right)$ (23)	$\eta_C = \frac{4Kn_1}{3} v_g'^{1/3}\exp\left(\frac{1}{2}\ln^2\sigma_g\right)$ (24)
	v_g' is dimensionless particle geometric mean volume, $v_g' = v_g/v_1$.	
Condensation coefficient for 2^{nd} moment	$\eta_{FM} = v_g'^{2/3}\exp\left(2\ln^2\sigma_g\right)$ (25)	$\epsilon_C = \frac{4Kn_1}{3} v_g'^{1/3}\exp\left(\frac{7}{2}\ln^2\sigma_g\right)$ (26)
Coagulation coefficient for 2^{nd} moment	$\zeta_{FM} = r_g'^{1/2} b_2 \exp\left(\frac{3}{2}\ln^2\sigma_g\right)\left[\exp\left(\frac{25}{8}\ln^2\sigma_g\right) + 2\exp\left(\frac{5}{8}\ln^2\sigma_g\right) + \exp\left(\frac{1}{8}\ln^2\sigma_g\right)\right]$ (27)	$\zeta_C = K\left[1 + exp\left(ln^2\sigma_g\right) + 1.257\left(Kn_1/r_g'\right)\times exp\left(-\frac{1}{2}ln^2\sigma_g\right)\left(1 + exp\left(-2ln^2\sigma_g\right)\right)\right]$ (28)
	$b_2 = 0.39 + 0.5\sigma_g - 0.214\sigma_g^2 + 0.029\sigma_g^3$ (Lee et al. 1984).	

3.8.3 PLA particle concentrations

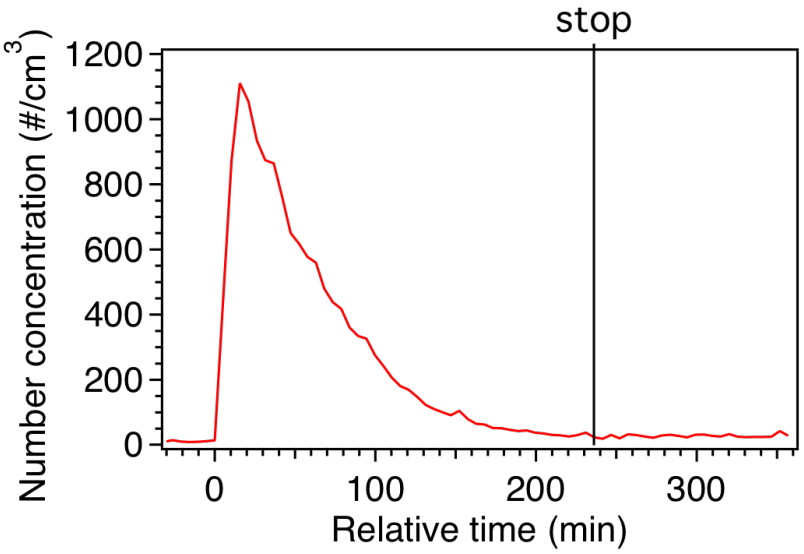

Figure 3.6 An example of PLA particle number concentration time series in chamber experiment, the extruder nozzle temperature was 210 °C, the build plate was not heated. Time zero on the x-axis indicates the beginning of the print run (filament extrusion), the vertical line indicates the time when printing stopped; the print time is ~ 4 hr.

3.8.4 Model results

3.8.4.1 The best fits of model results to the observation data

For each set of model inputs (R, f, P_s, x, T) there was a set of outputs (N, D_{pg} and σ_g). The best model solution (best fit of the model) was determined by comparing these model outputs with the observed steady state data. Errors were calculated as (model – observation)/observation × 100%, then the average errors were calculated as (|error N|+|error D_{pg}|+|error σ_g|)/3. The best fit was the solution with the minimum average error. The average errors as functions of the three vapor properties, for each of the four printer runs simulated, are shown in Figure 3.7. In general, there was one clear best solution for each of the three ABS printer runs, indicated by the average error reaching a minimum

for one simulation result, and this solution was associated with the minimum average error for each of the three parameters (P_s, R, f). However for nylon, there were two solutions that showed similar average errors, with the values of vapor properties parameters differ substantially. Here we only select the one with the minimum average error as the best fit and discuss in the main text, but the overall findings are similar using either solutions. In this case, a noteworthy feature was that although P_s and f values for the two solutions differed by 10 (one increased by a factor of 10, the other decreased by factor of 10), R was relatively the same, suggesting that R was a critical parameter in explaining the differences between different printer runs (i.e., extruder temperature).

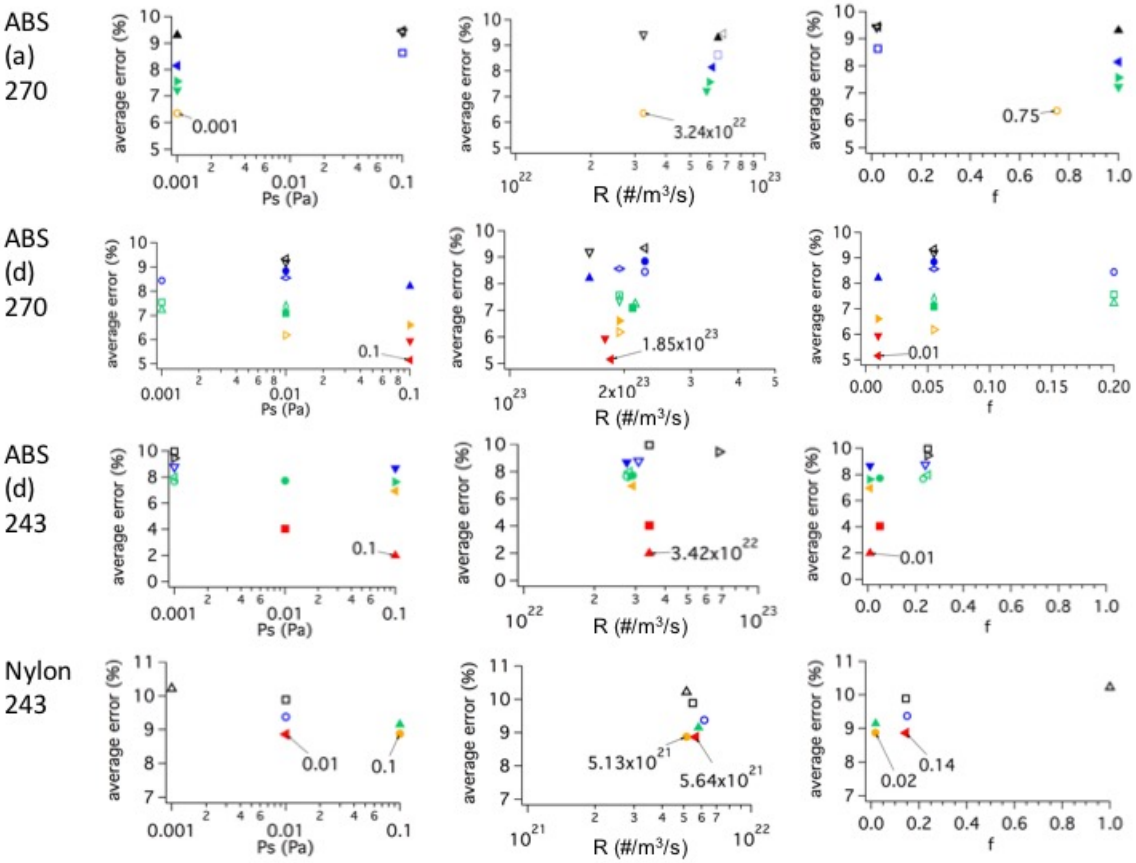

Figure 3.7 The average errors of model simulated and observed steady state particle characteristics, as functions of vapor properties parameters (P_s, R and f). Each row indicates the average errors for the specific print run; the notation is filament material (*filament brand*) extrusion temperature. Each marker indicates the average error calculated for one model solution to the observation. The best fits are noted with arrows and values. Only the average errors below normally 10% are shown.

3.8.4.2 Sensitivity analysis results

T = 405 K, x = 50 cm

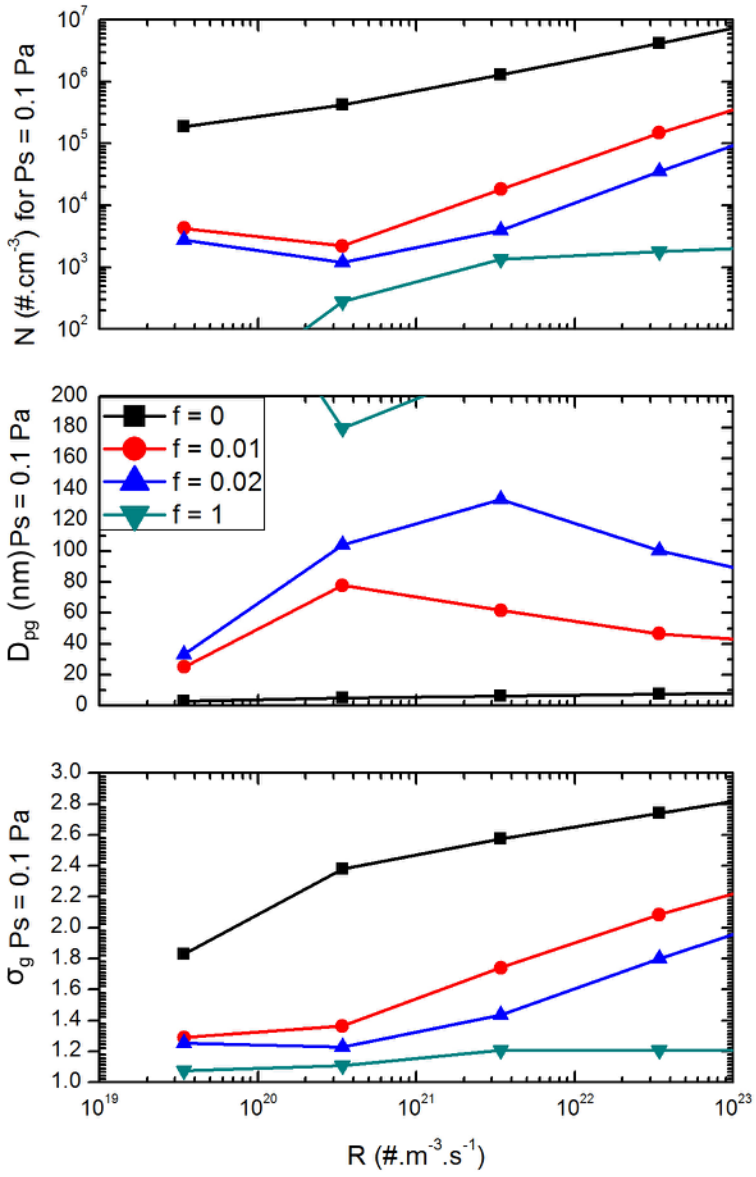

Figure 3.8 Steady state particle number concentration (*N*), geometric mean size (D_{pg}) and geometric standard deviation (σ_g) as a function of vapor generation rate (*R*) and condensation factor (*f*) respectively, when saturation vapor pressure (P_s) was 0.1 Pa, temperature (*T*) was 405 K and effective length (*x*) was 50 cm.

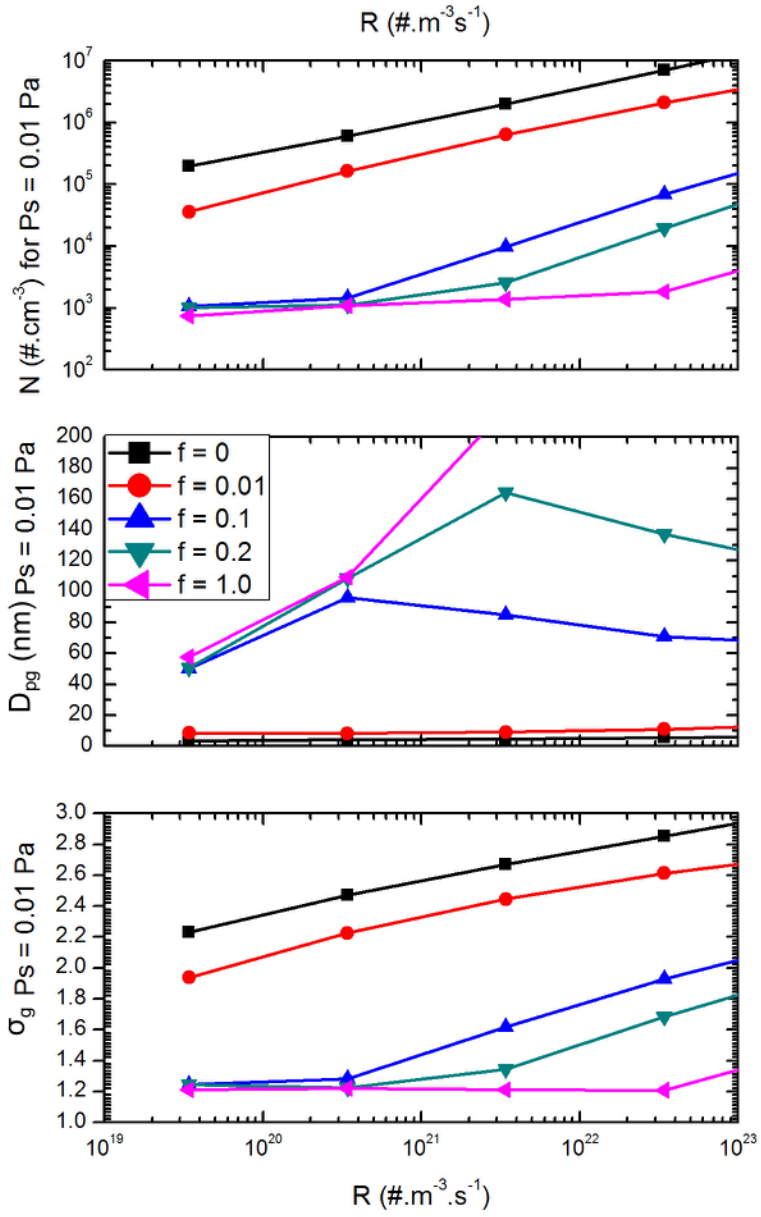

Figure 3.9 Steady state particle number concentration (*N*), geometric mean size (D_{pg}) and geometric standard deviation (σ_g) as a function of vapor generation rate (*R*) and condensation factor (*f*) respectively, when saturation vapor pressure (P_s) was 0.01 Pa, temperature (*T*) was 405 K and effective length (*x*) was 50 cm.

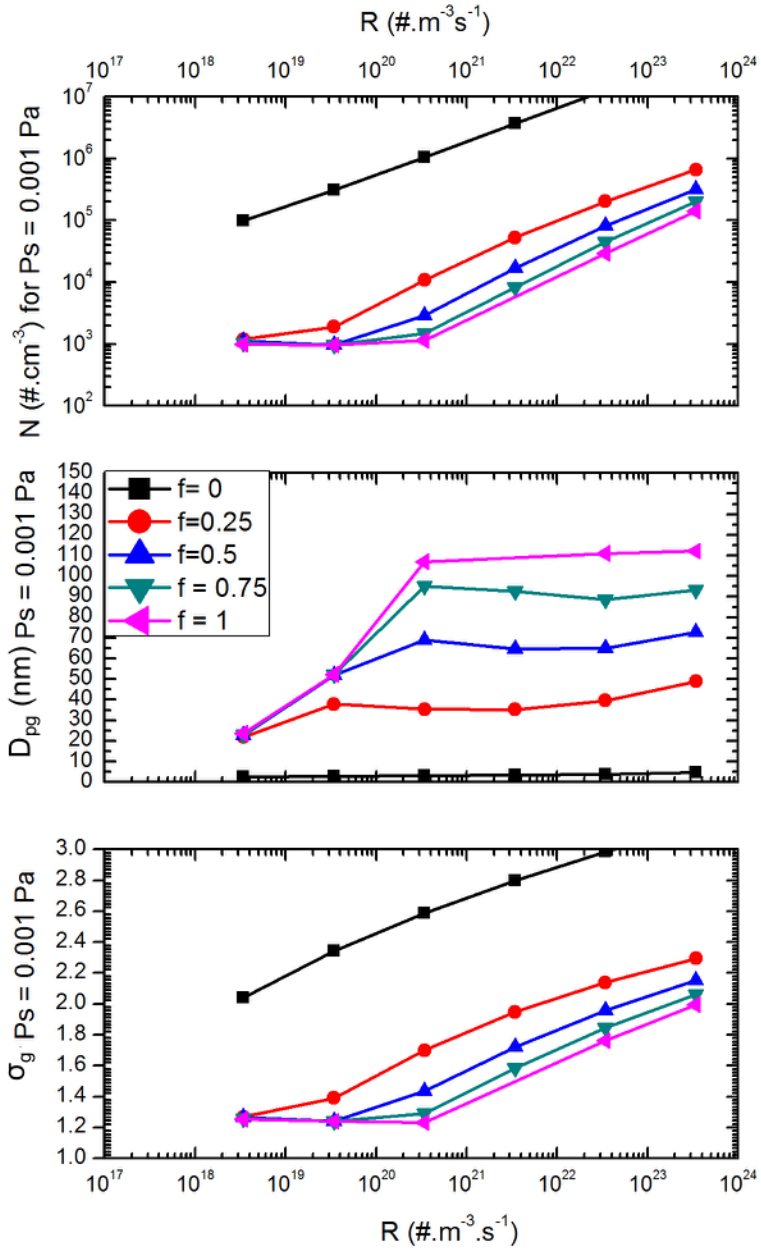

Figure 3.10 Steady state particle number concentration (*N*), geometric mean size (D_{pg}) and geometric standard deviation (σ_g) as a function of vapor generation rate (*R*) and condensation factor (*f*) respectively, when saturation vapor pressure (P_s) was 0.001 Pa, temperature (*T*) was 405 K and effective length (*x*) was 50 cm.

T = 420 K, x = 50 cm

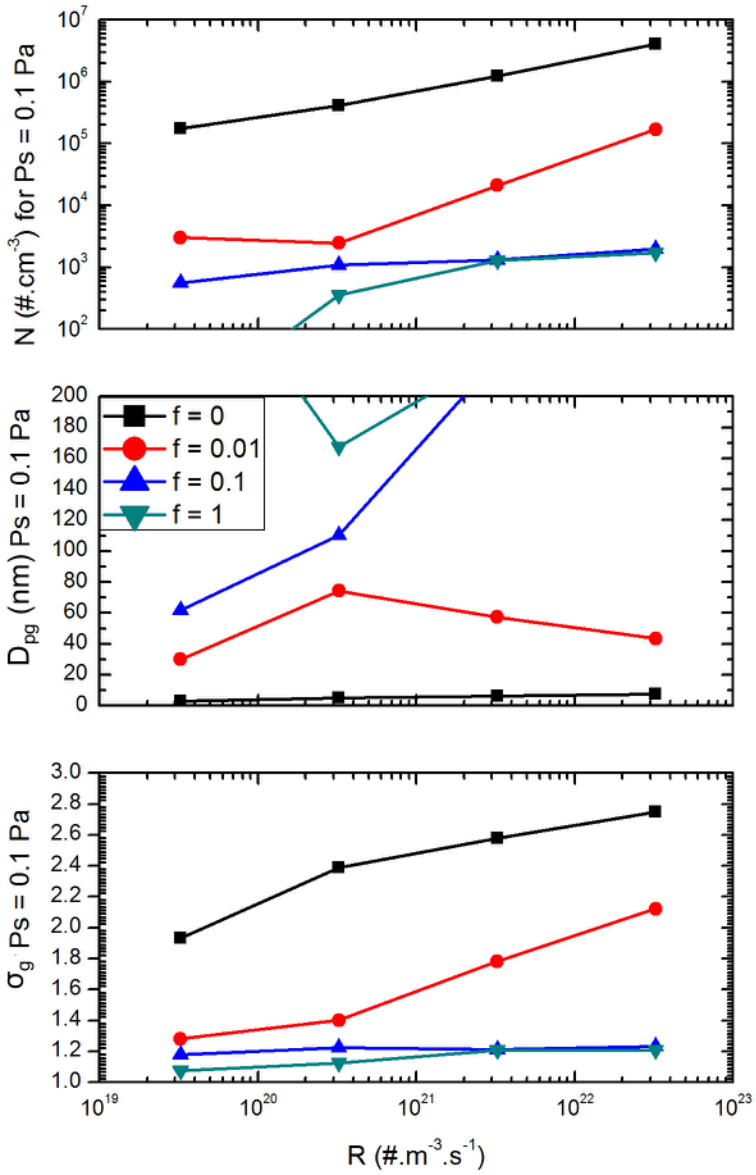

Figure 3.11 Steady state particle number concentration (*N*), geometric mean size (D_{pg}) and geometric standard deviation (σ_g) as a function of vapor generation rate (*R*) and condensation factor (*f*) respectively, when saturation vapor pressure (P_s) was 0.1 Pa, temperature (*T*) was 420 K and effective length (*x*) was 50 cm.

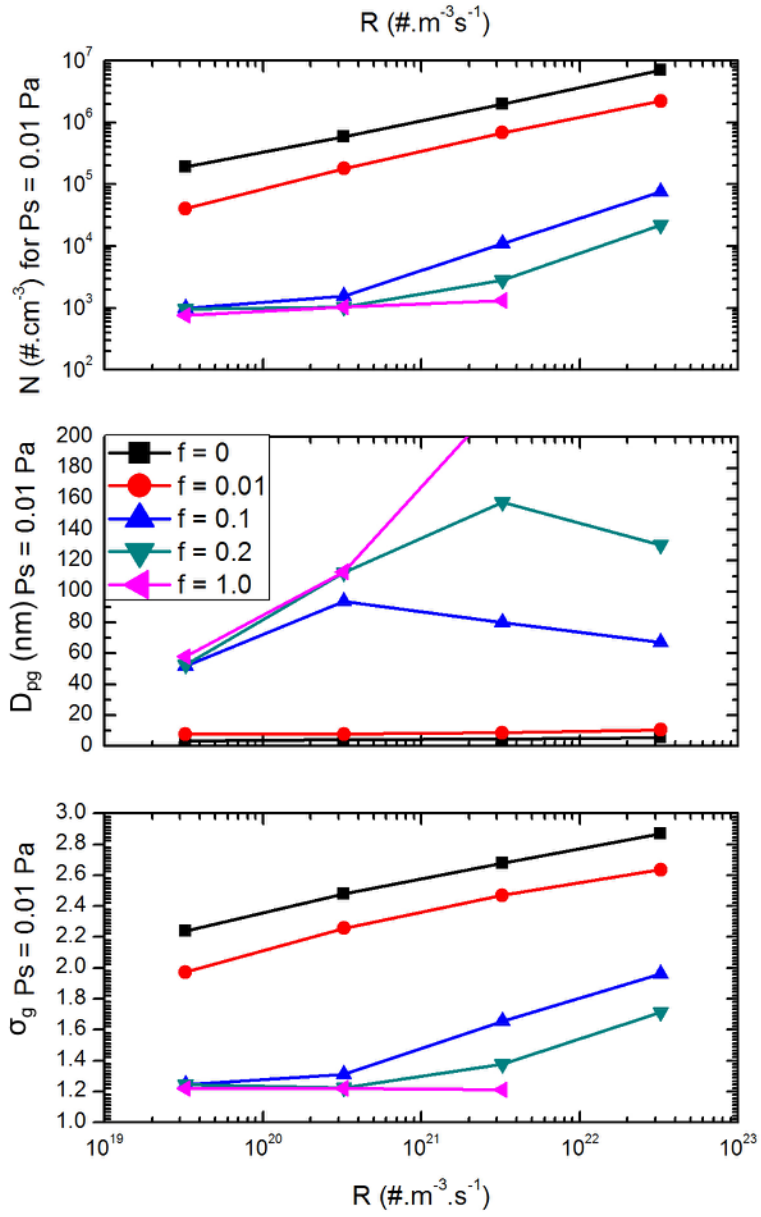

Figure 3.12 Steady state particle number concentration (*N*), geometric mean size (D_{pg}) and geometric standard deviation (σ_g) as a function of vapor generation rate (*R*) and condensation factor (*f*) respectively, when saturation vapor pressure (P_s) was 0.01 Pa, temperature (*T*) was 420 K and effective length (*x*) was 50 cm.

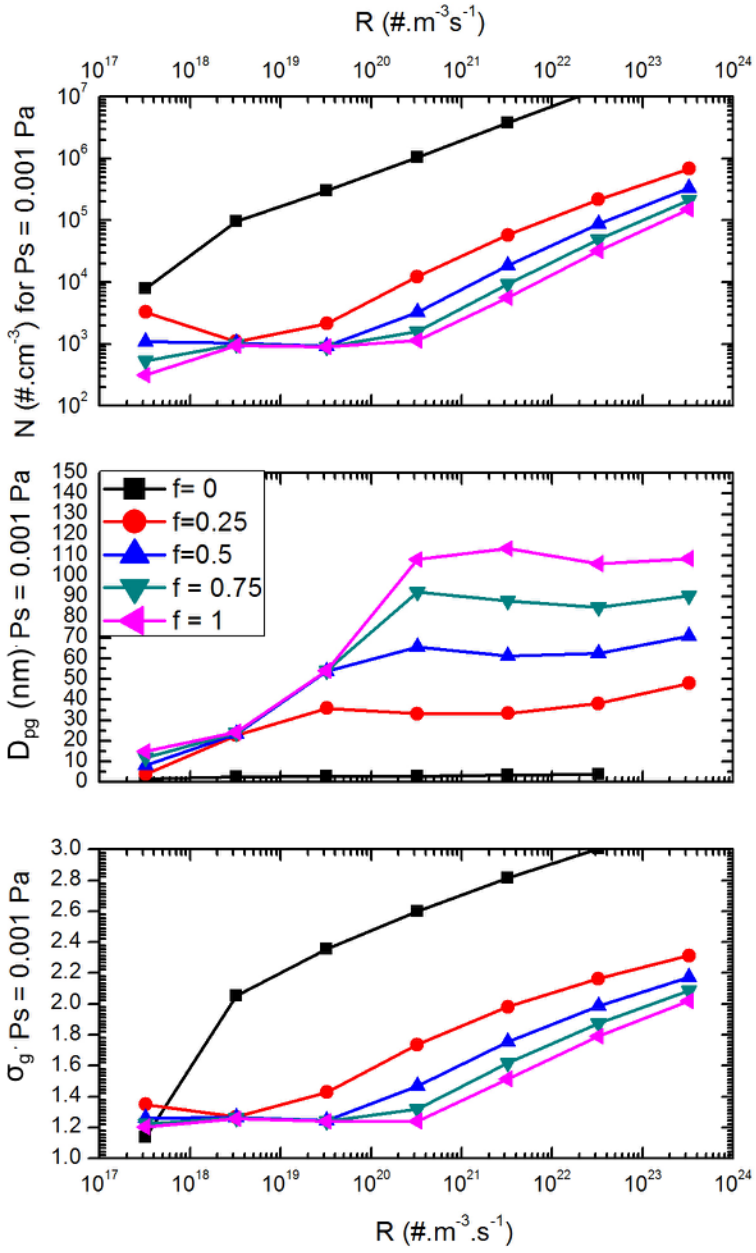

Figure 3.13 Steady state particle number concentration (*N*), geometric mean size (D_{pg}) and geometric standard deviation (σ_g) as a function of vapor generation rate (*R*) and condensation factor (*f*) respectively, when saturation vapor pressure (P_s) was 0.001 Pa, temperature (*T*) was 420 K and effective length (*x*) was 50 cm.

3.8.4.3 Relationship between steady state number concentration and model simulated vapor parameters

Considering only the best solutions for the four different printer runs, observed steady state number concentration and modeled vapor generation rate was correlated and generally linear (Figure 3.14a). Lower correlation was found for saturation vapor pressure, and even less for the condensation factor (Figure 3.14b, c). However, this analysis is limited by the number of data points (i.e., model solutions in good agreement with the observations). To expand the number of comparisons we look at the correlations between modeled number concentration and the vapor parameters when the model average errors were less than 10%. Similar trends were found (Figure 3.14d to f), supporting the conclusion that R is a critical parameter in the model that predicts steady state number concentrations. Note that the three vapor parameters are interrelated accounting for some of the variability in each plot (Figure 3.14d, e, f).

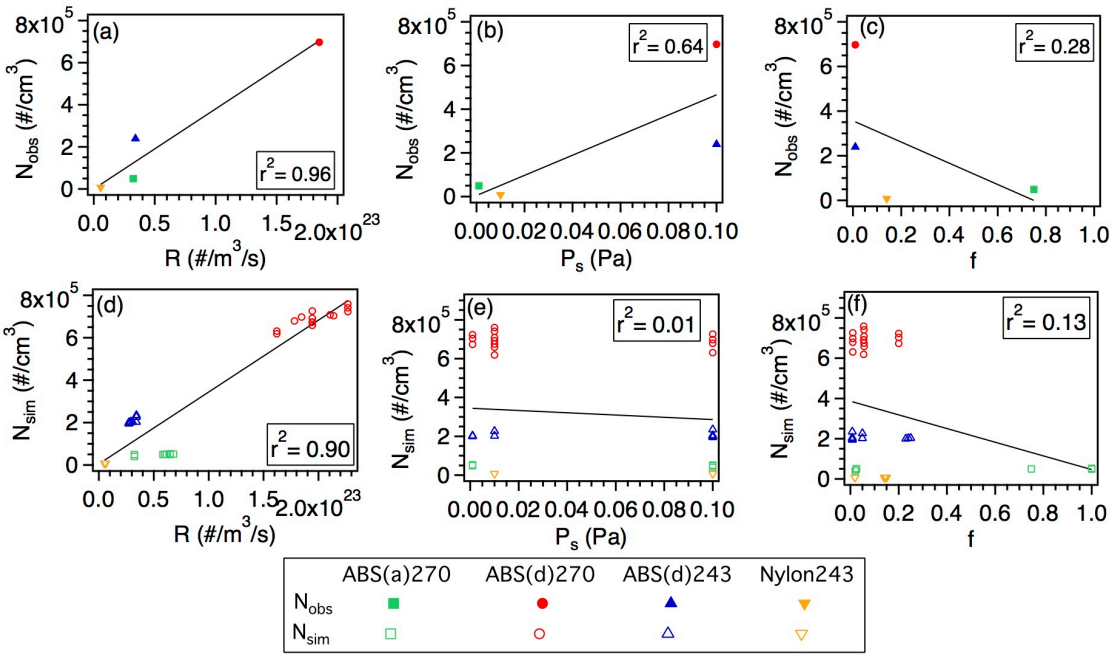

Figure 3.14 Plots a, b and c show the least squares fit for observed steady state particle number concentration (N_{obs}) vs. model simulated vapor parameters (R, P_s and f). Plots d, e and f show the simulated number concentration (N_{sim}) vs. vapor parameters for model solutions with average errors below 10%.

3.8.5 Particle thermophoresis and diffusion calculation

For particles smaller than gas mean free path (λ = 68 nm), the velocity due to thermophoresis is independent of particle size and proportional to the temperature gradient (Hinds 1999):

$$v_{th} = \frac{-0.55\mu\nabla T}{\rho_g T_p} \tag{29}$$

where μ is the viscosity of air calculated using Sutherland's formula ($\mu = \mu_0 \frac{T_0+C}{T_g+C}\left(\frac{T_g}{T_0}\right)^{3/2}$, where μ_0 is the reference viscosity at reference temperature T_0, i.e., 1.72 × 10^{-5} Pa•s at 273 K, C is the Sutherland's constant and is 110 K, T_g is the temperature of air and is 420

K, (Sutherland 1893); ∇T is the temperature gradient, which is estimated as 247 K/0.01 m (temperature gradient is the difference between extruder nozzle and chamber temperature for a distance of 1 cm, i.e., (270 °C – 23 °C)/1 cm); ρ_g is the density of air calculated by $\rho_g = \frac{p}{R_{specific} T_g}$ (where p is the pressure of air, $R_{specifc}$ is the specific gas constant for dry air); T_p is the temperature of the particle and is 420 K.

Thus the distance that a particle of size smaller than 68 nm travels in 1 second is 0.91 mm and independent of particle size.

Particle movement by diffusion can be calculated by:

$$x_{diff} = \sqrt{2D't} \tag{30}$$

where D' is the diffusion coefficient for particle calculated using Stokes-Einstein equation ($D' = \frac{k_B T_p C_c}{3\pi\mu D_p}$, where k_B is Boltzmann's constant, D_p is particle diameter, C_c is the slip correction factor and $C_c = 1 + \frac{\lambda}{D_p}\left[2.34 + 1.05exp\left(-0.39\frac{\lambda}{D_p}\right)\right]$ for particles smaller than 0.1 μm in size.) (Hinds 1999).

Since diffusion coefficient is related to particle size, for a 3 nm diameter particle, the distance it travel in 1 second due to diffusion is 1.2 mm, for particle diameter of 4 – 50 nm, the distance travels in 1 second is in range of 0.07 – 0.87 mm. Calculation examples are shown in Table 3.4.

Table 3.4 Distance a particle travels in 1 second due to diffusion (x_d) and thermophoresis (x_{th}).

D_p (nm)	C_c	D' (m^2/s)	x_d (m)	v_{th} (m/s)	x_{th} (m)
3	77.43	6.712×10^{-7}	1.16×10^{-3}	-9.11×10^{-4}	9.11×10^{-4}
5	46.70	2.429×10^{-7}	6.97×10^{-4}	-9.11×10^{-4}	9.11×10^{-4}
10	23.65	6.151×10^{-8}	3.51×10^{-4}	-9.11×10^{-4}	9.11×10^{-4}
30	8.308	7.202×10^{-9}	1.20×10^{-4}	-9.11×10^{-4}	9.11×10^{-4}
50	5.254	2.733×10^{-9}	7.39×10^{-5}	-9.11×10^{-4}	9.11×10^{-4}

CHAPTER 4. CHEMICAL COMPOSITION AND TOXICITY OF PARTICLES EMITTED FROM A CONSUMER-LEVEL 3D PRINTER USING VARIOUS MATERIALS

Qian Zhang, Michal Pardo, Yinon Rudich, Ifat Kaplan-Ashiri, Jenny P. S. Wong, Aika Y. Davis, Marilyn S. Black, Rodney J. Weber

Environ. Sci. Technol.

Under review

4.1 Abstract

Consumer-level 3D printers are found to emit high levels of ultrafine and fine particles, though little is known about their chemical composition or potential toxicity when inhaled. We report on chemical characteristics of the particles in comparison to printer filaments, and preliminary assessments of particle toxicity. Particles emitted from polylactic acid (PLA) appeared to be largely composed of the bulk filament material with mass spectra similar to the PLA monomer spectra. Acrylonitrile butadiene styrene (ABS) emitted vastly more particles and they differed from that of the bulk filament, suggesting trace additives controlled particle formation. *In vitro* cellular assays showed a decrease in cell survival rate and generation of intracellular reactive oxygen species for both rat macrophages and human epithelial cells when exposed to 3D printer-generated particles. Acellular measurement confirmed particle oxidative potential. Additionally, mice intratracheal exposure showed inflammatory response. For all tests, PLA-emitted

particles elicited similar response levels as ABS-emitted particles, despite much lower exposure concentrations, implying that PLA-emitted particles were more toxic. However, particle emissions from ABS filaments are potentially more detrimental when considering overall exposure due to much higher emissions. Our results suggest 3D printer particle emissions are not benign and exposures should be minimized.

4.2 Introduction

Three dimensional (3D) printing is an emerging technology in industrial applications, but also popular for domestic usage (Horvath 2014). Fused deposition modeling (FDM) 3D printing heats a thermoplastic material and deposits it by layers to build an object. Among a wide range of materials, acrylonitrile butadiene styrene (ABS) and polylactic acid (PLA) are commonly used. ABS is characterized by high strength, stiffness, and resistance to chemicals. It also requires higher extruder nozzle and build plate temperatures than PLA (Kreiger and Pearce 2013). PLA is bio-degradable, thermally unstable, and more brittle compared to other plastics (Kreiger and Pearce 2013). Numerous studies show that 3D printing emits both particles and volatile organic compounds (VOCs). These emissions can depend on many factors, such as printer brand, filament material, filament brand and color, extrusion temperature, and filament feed rate (Floyd et al. 2017; Stabile et al. 2017; Zhang et al. 2017; Azimi et al. 2016; Deng et al. 2016; Yi et al. 2016; Kim et al. 2015). Previous studies on laser printers and thermal processing of plastics showed potential exposure to gases and particles (Pirela et al. 2014; Unwin et al. 2013), suggesting that 3D printer emissions may also be of concern (Stefaniak et al. 2017a). While it was shown that 3D printers emit potentially harmful VOCs like styrene, butanol, cyclohexanone, ethylbenzene, and others (Stefaniak et al.

2017b; Wojtyła et al. 2017; Azimi et al. 2016), the chemical species that the particles are comprised of are not well characterized, and their toxicity is also uncertain. Most of the particle composition measurements reported have focused on carbonyl compounds and metals (Vance et al. 2017; Stefaniak et al. 2017b; Zontek et al. 2017; Steinle 2016).

The average particle emission rates during 3D printing ranged from 2×10^{8} to 2×10^{12} particles/min (Stabile et al. 2017; Zhang et al. 2017; Zontek et al. 2017; Azimi et al. 2016; Deng et al. 2016; Steinle 2016; Yi et al. 2016; Kim et al. 2015) and most of the emitted particles were ultrafine particles (less than 0.1 μm diameter) (Zhang et al. 2017; Kim et al. 2015). Studies have shown that exposure to ultrafine particles from different sources will directly (and indirectly) modify the immune response mechanism (Xia et al. 2016; Frampton et al. 2006). Ultrafine particles are potentially hazardous because they can deposit in the respiratory tract, enter the blood stream, translocate to remote organs, and damage mitochondria, due to their specific properties (Oberdörster et al. 2005; Li et al. 2003). A well-established mechanism associated with particle adverse biological effects, for both nanoparticles (NPs) (Hussain et al. 2009) and ambient fine particles (Abrams et al. 2017), is the generation of reactive oxygen species (ROS), the excess of which causes cellular damage and induces oxidative stress (Hussain et al. 2009; Ayres et al. 2008; Li et al. 2008). Oxidative stress can trigger redox-sensitive pathways that lead to biological responses, such as inflammation (Hussain et al. 2009), cell death (Peixoto et al. 2017), and diseases (Abrams et al. 2017; Li et al. 2008). Previous studies that exposed various cell types to NPs or particulate matter (PM) reported corresponding formation of ROS and oxidative stress or inflammation (Pardo et al. 2015; Keenan et al. 2009; Ayres et al. 2008; Li et al. 2008). One integrative measure of a particle' ability to induce

oxidative stress is the particle oxidative potential (OP), which has been measured by various acellular assays (Fang et al. 2015, 2016; Sauvain et al. 2013). The OP of ambient $PM_{2.5}$ (PM smaller than 2.5 μm in size) has been linked to adverse health effects associated with acute cardiorespiratory outcomes in a large metropolitan environment (Abrams et al. 2017).

In light of the emerging applications of consumer 3D printers and the potential increase in the exposure to the emitted particles, this study focuses on chemical composition and potential health impacts of particles emitted during 3D printing. Specifically, we analyze particle chemical composition via multiple methods and compare that with the raw filament material. We also assess particle toxicity through *in vivo* inflammatory model and *in vitro* cellular and acellular models through oxidative stress mechanisms.

4.3 Methods

4.3.1 Particle preparation and characterization

4.3.1.1 Particle sample preparation

A consumer grade 3D printer was operated in a 1 m^3 well-mixed stainless-steel emission test chamber (Zhang et al. 2017). Air removed of particles and VOCs via a high-efficiency particulate air (HEPA) filter (Pall Corporation, Port Washington, NY, USA) and an absorption column (ASTM 2013) was supplied to the chamber continuously with an air exchange rate of one volume per hour (flow rate of 16.7 L/min). The environment inside the chamber was at room temperature (23 ± 1 ºC) and relative

humidity (RH) of 3.0% ± 0.2% (Zhang et al. 2017). Three filament materials were tested; a high particle number emitting ABS filament (hereafter High ABS), an ABS filament that emitted particles of more typical ABS filaments (hereafter Regular ABS), and a PLA filament (hereafter PLA). A nylon filament was tested with only the dithiothreitol (DTT) assay (section 4.3.4). The tested printer extruder temperature was 270 ºC for ABS, 210 ºC for PLA and 243 ºC for nylon, and build plate temperature was 100 ºC for ABS and nylon, and 50 ºC for PLA. Particle concentrations in the chamber were monitored with online particle measurement instrumentation before, during and after printing. Instrumentation included a condensation particle counter (CPC 3022A, TSI Inc., Shoreview, MN, USA), a scanning mobility particle sizer (SMPS, differential mobility analyzer 3081 and CPC 3785, TSI Inc.) and an optical particle counter (OPC, AeroTrak 9306-01, TSI Inc.), collectively measuring particle number concentrations as a function of size for particles spanning nominally 7 nm to 25 μm in diameter. Surface area and mass (volume) concentrations were calculated from the measured number distributions assuming particles were spheres of unit density. These calculated values are uncertain since the particle density is not known; an estimation of the uncertainties can be found in Zhang et al. (2017). In addition, particles for offline toxicity analysis were collected on 25 mm laminated polytetrafluoroethylene (PTFE) membrane filters with 0.45 μm pore size (Sterlitech Corporation, Kent, MA, USA) throughout the printing period. The sampling time (i.e., printing period) varied slightly in order to collect sufficient mass on the filter (Table 4.1 and Table 4.2). Blank filter samples (Blank) were collected for 30 min before print started with the printer in the chamber, but not operating. Typical background number concentrations in the chamber were less than nominally 5 /cm^3.

To obtain aqueous particle suspensions for biological toxicity analyses, each filter was extracted in 11 mL of deionized water (DI) via sonication (Ultrasonic Cleaner, VWR International LLC., West Chester, PA, USA) in a sterile polypropylene centrifuge tube (VWR International LLC., Suwanee, GA, USA) for 1 hr. Then 10 mL of the extract with suspended particles was set aside for the toxicity analysis by storage at 4 ºC. The remaining 1 mL was re-aerosolized using a continuous flow ultrasonic nebulizer (U-5000AT, Cetac Technologies, Omaha, NE, USA). The nebulized aerosols were dried, neutralized and particle number distributions measured with the SMPS used in the chamber measurement. The particle concentration in the suspension was determined from the integrated mass concentration of nebulized aerosols and the efficiency of the nebulizer (see Section 4.6.1.1). More details can be found in Section 4.6.1.1, including size distributions measured in the chamber versus those of the nebulized extracts (Figure 4.4) and the calculations of liquid concentrations in all samples.

4.3.1.2 Particle chemical characterization

For Regular ABS and PLA emitted particles, submicron particle chemical composition (e.g., non-refractory organic species and inorganic species, such as sulfate, nitrate, and ammonia) was measured online from the chamber by either an Aerosol Chemical Speciation Monitor (ACSM, Aerodyne Research, Inc., Billerica, MA, USA) (Ng et al. 2011) or a time-of-flight Aerosol Mass Spectrometer (ToF-AMS, Aerodyne Research, Inc.) (DeCarlo et al. 2006; Drewnick et al. 2005) during the printing period. For High ABS, pyrolysis gas chromatography mass spectrometry (GC-MS, Agilent Technologies, Santa Clara, CA, USA) was performed on both the filament and the emitted particles collected on a quartz filter. Although this method is not optimal for

aerosol composition measurements due to limitations with filter sampling and sample alteration during pyrolysis, the goal was to contrast the composition of filament and particles generated from that filament with the same instrument.

4.3.1.3 Scanning electron microscope (SEM)

SEM imaging was applied to assess the solubility of particles (i.e., whether they remained solid in liquid), and to roughly compare particle properties in liquid to those *in situ*. The filters and particle suspensions were prepared in the same way as for toxicity analysis. The samples were coated with 8 nm thick carbon using the Safematic CCO-010 HV high vacuum coater, and analyzed by Zeiss Ultra55 high resolution SEM. The landing voltage was 3 – 5 kV and images were recorded using the In-Lens detector (high resolution topography contrast).

4.3.2 In vitro exposures

4.3.2.1 Cell culture

Rat alveolar macrophages (NR8383, CRL 2192) and human tumorigenic lung epithelial cells (A549), which represent the interaction with particles in lungs, were used to assess cytotoxicity of the particles, and to compare the potential different responses due to their specific properties and functions. NR8383 cells were grown in Hams F12K medium (Biological Industries, Beit-Haeemek, Israel) supplemented with 15% (w/v) fetal calf serum, 1% (w/v) glutamine and 1% (w/v) penicillin-streptomycin. A549 cells were grown in RPMI-1640 supplemented with 10% (w/v) fetal calf serum and 1% (w/v)

penicillin-streptomycin. Both cultures were incubated at 37 °C in a humidified atmosphere consisting of 95% air and 5% CO_2.

Cells were seeded 24 hr prior to exposure. All samples were sonicated in water bath for 5 minutes and then buffered with salts glucose media (SGM, pH = 7.2) prior to use, which comprised 50 mM Hepes, 100 mM NaCl, 5 mM KCl, 2 mM $CaCl_2$ and 5 mM glucose. Exposure was done using original extracted particle suspensions for all assays; for WST-1 assay, additional 10-time diluted suspensions were also studied. The volume used for the *in vitro* cellular experiments was 500 μL, which was comprised of 50 μL SGM, 400 μL particle extract and 50 μL phosphate buffer saline (PBS). For the 10-time diluted sample, 400 μL of particle extract was replaced by 40 μL particle extract and 360 μL DI water.

4.3.2.2 WST-1 cell viability assay

Cell viability was evaluated by the WST-1 (Abcam, UK) assay 24 hours after exposure according to the manufacturer's instructions and as previously described (Pardo et al. 2014). Exposure was done using original extracted particle suspensions and 10 times diluted suspensions for 24 hr respectively. Absorbance of the samples was measured at 440 nm and 650 nm by a microplate reader (BioTek, USA). Each experiment was repeated twice in quadruplicates for each cell type.

4.3.2.3 Determination of cell death mechanism

Flow cytometry (FACSCalibur, BD, Foster City, CA, USA) analysis was used to evaluate the cell death type and cell viability after 24 hr exposure. Annexin V-FITC and

the DNA interchelating dye propidium iodide (MEBCYTO®, MBL) were used to distinguish between apoptosis and necrosis. Fluorescence was excited at 488 nm and detected at 575 nm. Data were collected from 20,000 cells. Each experiment was repeated twice in triplicates for each cell type.

4.3.2.4 Intracellular ROS measurements

The dichlorodihydrofluorescein diacetate (H_2DCF-DA) fluorescent probe was used to assess the generation of intracellular ROS after 6 hr exposure with flow cytometer as previously described (Pardo and Tirosh 2009) The excitation and emission wavelengths for DCF were 495 nm and 529 nm respectively. Hydrogen peroxide was used as a positive control and untreated cells as negative controls. Each experiment was repeated twice in triplicates for each cell type.

4.3.3 In vivo exposures

4.3.3.1 Mice and treatments

Male C57BL/6 mice (7 – 8 weeks) were housed under standard light/dark conditions and had access to food and water *ad libitum.* The mice were randomly divided into groups (minimum, n = 6), and exposed to particle samples using an intra-tracheal model as previously published (Pardo et al. 2015, 2016). Briefly, each mouse was anesthetized with ketamine/xylazin (10 mg/kg and 5 mg/kg body weight, respectively) and placed on an inclined plastic platform. A single dose of the particle suspension (50 μL) was delivered onto the vocal cords and afterwards of the mouse; the nostrils were covered, so that the mouse inspired the instilled particle suspensions. 24 hr after the

exposure, mice were anesthetized again by intraperitoneal injection of ketamine/xylazin (20 mg/kg and 10 mg/kg body weight, respectively). Whole-body perfusion with phosphate-buffered saline (PBS) was performed, the lungs and tracheas were exposed by dissection, and tracheal cannula was inserted. Lungs were washed with PBS solution twice. Cells were separated from the broncho alveolar lavage fluid (BALF) by centrifugation. Lipopolysaccharide, a major component of the outer membrane of bacteria that elicits a strong immune response, was used as a positive control.

All experiments were approved by the Animal Care and Use Committee of the Weizmann Institute of Science.

4.3.3.2 Multispectral imaging flow-cytometry (ImagestreamX) analysis

BALF cells were re-suspended with Red Blood Cell Lysis Buffer. Blocking the Fc receptor was performed using anti-mouse CD16/32 antibody. BALF cells were stained with conjugated anti-mouse antibodies (CD45-PerpCP, CD11b-PE, F4/80-APC/Cy7, PE/Cy7-CD115 and Ly6G-APC), purchased from BioLegend (San Diego, CA, USA). Multispectral imaging flow cytometry (ImageStreamX mark II flow cytometer; Amnis Corp – part of EMD Millipore) was used for the analysis as previously describe (Pardo et al. 2015). About 10^4 cells were collected from each sample and data was analyzed using the image analysis software (IDEAS 6.0; Amnis Corp). Gating for single cells was performed using the Area and Aspect ratio features, and for focused cells was performed using the Gradient RMS feature (George et al. 2006). Further gating was applied with CD45+ cells using CD45 intensity and staining area. Different monocytes sub-populations, cells were identified with gating for CD11b, F480, and Ly6G.

4.3.4 DTT (dithiothreitol) acellular assay

Oxidative potential (OP) of 3D printer emitted particles was assessed using the dithiothreitol (DTT) cell-free assay following the method in Cho et al. (2005). For the water-soluble DTT assay, the filter was extracted in 4.9 mL of DI by sonication for 1 h, the extract was filtered through a 0.45 μm PTFE syringe filter (Fisher Scientific, USA) and then analyzed using a semi-automated DTT analytical system (Fang et al. 2015). In brief, the sample was incubated with DTT at 37 °C and pH of 7.4. At five designed time points, the absorbance of the colored product from DTT reacting with 5,5'-dithiobis-(2-nitrobenzoic acid) was measured at 412 nm, which was used to determine the remaining DTT. The total (i.e., soluble + insoluble) DTT assay was similar to the water-soluble DTT assay, except the sample filter was kept in direct contact with DTT during incubation (i.e., no filtration of extract), following Gao et al. (2017). Blanks (i.e., extracts of blank filters) and positive controls (9,10-phenanthrenequinone) were also carried out in the same manner. DTT concentrations were quantified based on a pre-determined absorbance calibration curve using standard DTT solutions. For each sample, the DTT consumption rate was obtained by a linear fitting of the 5 points of remaining DTT. OP can be expressed as DTT consumption (corrected by blank) normalized by particle mass (OP^{DTT}_{m}) (Fang et al. 2015). Three replicates were done for each sample. A measurement was considered above the detection limit when the signal was larger than three times the standard deviation of the blanks. Particle concentration in the extract for total DTT analysis was based on particle mass collected on the filter and the volume of the extraction liquid, since the filter with particles that could not be extracted and the

extracted particles were all in the reaction vial with the DTT (see Section 4.6.1.2 for details).

4.3.5 Statistical analysis

The differences between treatment groups were analyzed by one-way analysis of variance, and considered significant at $p < 0.05$ using the Fisher protected least-significant difference method. The *t* tests were used to compare the results of two different groups at a *p*-value of 0.05.

4.4 Results and Discussion

4.4.1 Characterization of 3D printer particles

4.4.1.1 Particle emission

Detailed descriptions of emissions and contrasts between particle numbers and sizes for these (and many other) filaments can be found in Zhang et al. (2017). In general, particles emitted from all filaments were lognormally distributed (Figure 4.5). Time series of total particle number, surface and volume (mass) concentrations are given in Figure 4.6. Particle number emission yields (total particle number emissions per mass of object printed) for the filaments tested were as follows: High ABS 1.42×10^{11} g^{-1}, Regular ABS 1.52×10^{10} g^{-1}, PLA 1.35×10^{9} g^{-1} and nylon 1.58×10^{9} g^{-1}. Particle surface area and volume (mass) yields and mean particle sizes can be found in Table 4.3.

4.4.1.2 Particle chemical composition

The ACSM results showed the particles emitted from Regular ABS and PLA filaments were largely organic in composition; inorganic species were below limit of detection (LOD). Other trace species such as metals, may be present (Zontek et al. 2017), but were not measured in this study. ACSM data also showed that the mass spectra of Regular ABS and PLA emitted particles were different, indicating their compositions differed, as expected (Figure 4.1). Furthermore, the mass spectra of Regular ABS emitted particles were different from those of the raw filament material monomers (i.e., acrylonitrile, 1,3-butadiene, styrene) (Stein 2016), while the mass spectra of PLA emitted particles were mostly similar to those of the PLA monomers (i.e., lactic acid, lactide) (Figure 4.1). This is consistent with Vance et al. (2017) where the Raman spectra of ABS emitted particles lacked the peaks corresponding to ABS monomers seen in the spectra of ABS filament. Additionally, for Regular ABS emitted particles, no significant change in the mass spectra (measured by the AMS) was observed throughout the print time (Figure 4.7), suggesting that these particles were not subjected to additional processing following their emission (i.e., evaporation of semi-volatile components, reactions with oxidants). However, for PLA emitted particles, the fraction of small organic fragments (mass to charge (m/z) < 30) increased throughout print time (Figure 4.7). While we cannot identify the chemical species leading to the observed changes, due to the similarity in the mass spectral pattern of this group of small m/z fragments to lactic acid (Figure 4.1), we speculate that the increasing contribution of lactic acid to particle composition is due to the increasing total particle surface area throughout the print time, which increases the partitioning of semi-volatile organic gases (e.g., lactic acid) emitted from PLA. Since the ACSM/AMS does not allow for the analysis of filament composition, pyrolysis GC-MS

provided a more direct comparison of composition between filament material and the particles formed. The evolved gas analysis of High ABS emitted particles showed substantially different spectra from that of the ABS raw filament (Figure 4.8). This indicated that the ABS particles are not formed directly from the bulk ABS material, but potentially from some additives, such as fatty acids detected by pyrolysis GC-MS (Figure 4.8).

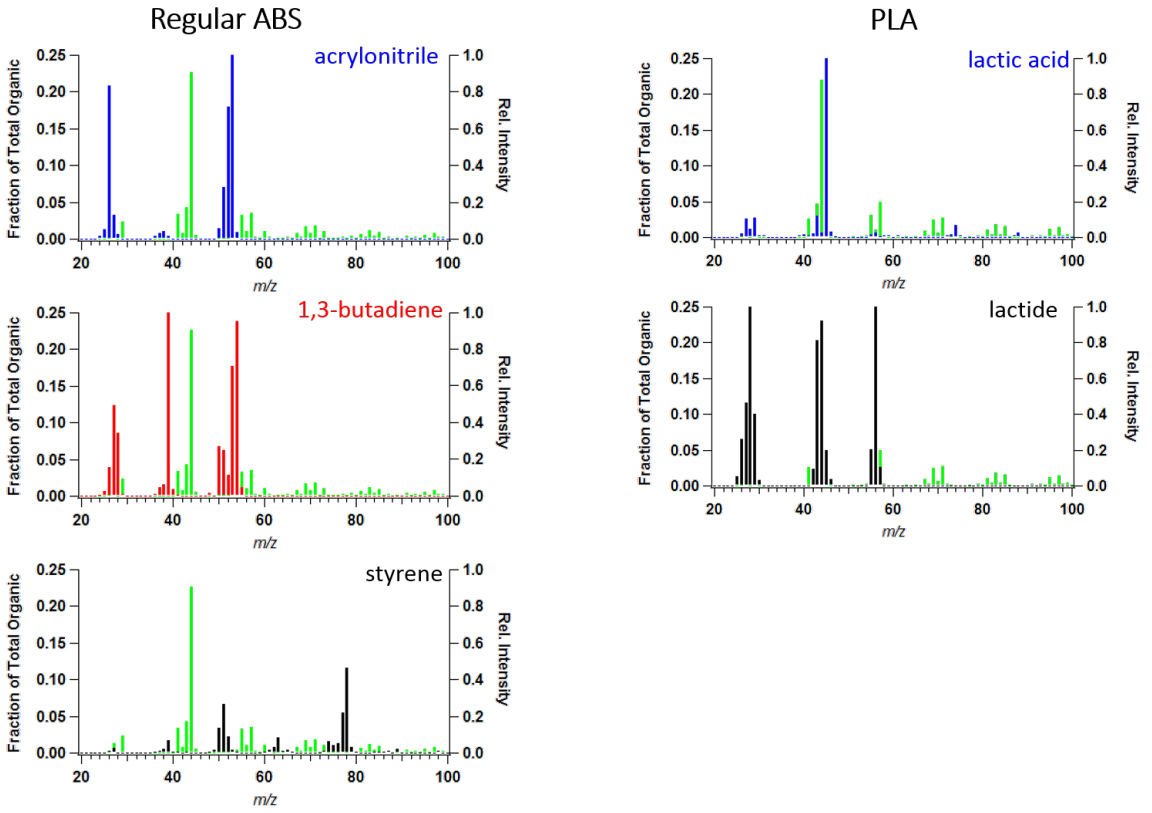

Figure 4.1 Online chemical composition measurements (with an ACSM) of particles emitted from Regular ABS and PLA. Particle mass spectra are shown in green. Reference spectra of monomers corresponding to the raw filament materials for ABS (acrylonitrile, blue; 1,3-butadiene, red; styrene, black) and PLA (lactic acid, blue; lactide, black) are included for comparison (NIST webbook, Stein 2016). Particles from a printer running PLA filament have spectra similar to PLA monomers, whereas for ABS the particle spectra are different from monomer spectra.

To some degree, the chemical analysis can help explain contrasts in emissions from the two ABS filaments tested and differences between PLA and ABS in general. For ABS, apparently a minor unknown filament additive accounts for the particle formation, which was consistent with previous model results (Zhang et al. 2018). Different additives may be used by different filament manufacturers, for example, High ABS that had much higher particle emissions contained 5% – 10% more additives than Regular ABS according to the Safety Data Sheets from the manufacture. PLA is printed

at a much lower temperature, and so in general may be less susceptible to volatilization of typical additives, leading to only the bulk material contributing to the particle formation and much lower particle emissions. (Note, there is data showing PLA filaments with specialized properties, which contain unknown additives, can also be much higher aerosol emitters than regular PLA filaments (Zhang et al. 2017)). Our findings on the particle chemistry imply that the toxicity of particles emitted from 3D printers could vary widely amongst filaments on the market, and may not be directly related to the toxicity of the bulk filament materials.

4.4.1.3 Particle imaging analysis

SEM images of dried particle suspensions (Figure 4.9) provided information on particle shape, size, and morphology. Particle diameters estimated roughly from SEM images were 71 ± 20 nm (mean ± standard deviation) for High ABS, 106 ± 20 nm for Regular ABS, and 14 ± 25 nm for PLA. (Sizes were estimated from the images by analysis of 15 particles for PLA and 50 particles for both ABS. Due to the much smaller size of PLA, this method of sizing was highly uncertain). The SEM analysis showed the particle sizes in the aqueous samples were approximately comparable to those measured in the chamber during filter sampling (Table 4.3, mean sizes for the number distributions were 49 nm, 123 nm and 51 nm for High ABS, Regular ABS and PLA, respectively). Imaging also indicated that the particles were not highly water-soluble as they were in solution for an extended period of time (over 30 days) prior to SEM analysis.

4.4.2 Cytotoxicity of particles

Human tumorigenic bronchial epithelial cells (A549) represent respiratory cells which could be affected by inhalation exposure. Rat alveolar macrophages (NR8383) are one of the first cell lines defending against invasion to lungs. The effects of 3D printer emitted particles on cell viability of these two cell types after 24 h exposure measured by the WST-1 assay are shown in Figure 4.2A. All three types of particles induced statistically significant decreases in cell survival rates for A549 and NR8383 compared to the blanks at the indicated concentrations, while no significant differences were found between cell lines or among different particle types. A 10 times diluted solution was less toxic to both cell types (Figure 4.10).

Total cell death increased significantly after 24 h exposure to all three types of particles compared to the blanks for NR8383, but not A549 cells (Figure 4.2B). The alveolar macrophages were apparently more sensitive to exposures than epithelial cells, as they exhibited an increased cell death with exposure to the blank (Figure 4.11). It was also found that cell death involved both apoptosis and necrosis (Figure 4.11), particularly late apoptosis/necrosis. Apoptosis (programmed cell death) is an organized process that includes cell shrinkage, blebbing, chromatin condensation, and cell fragmentation (Peixoto et al. 2017); it is reported as a consequence following exposure to PM for various cells (Peixoto et al. 2017; Deng et al. 2014). Necrosis is characterized by membrane potential loss that leads to swelling and rupture of the plasma membrane (Peixoto et al. 2017), and is found to be associated with exposure to metal NP and smoke (Peixoto et al. 2017; Moschini et al. 2013; Foldbjerg et al. 2011).

High ABS and PLA emitted particles increased intracellular ROS generation by 13% – 24% compared to the blanks for both cell types with no statistical differences

between the two cell lines (Figure 4.2C). These observations were in agreement with studies showing that PM or NP can increase ROS and oxidative stress, and thereby may contribute to the adverse health effects (Hussain et al. 2009; Keenan et al. 2009; Li et al. 2003, 2008).

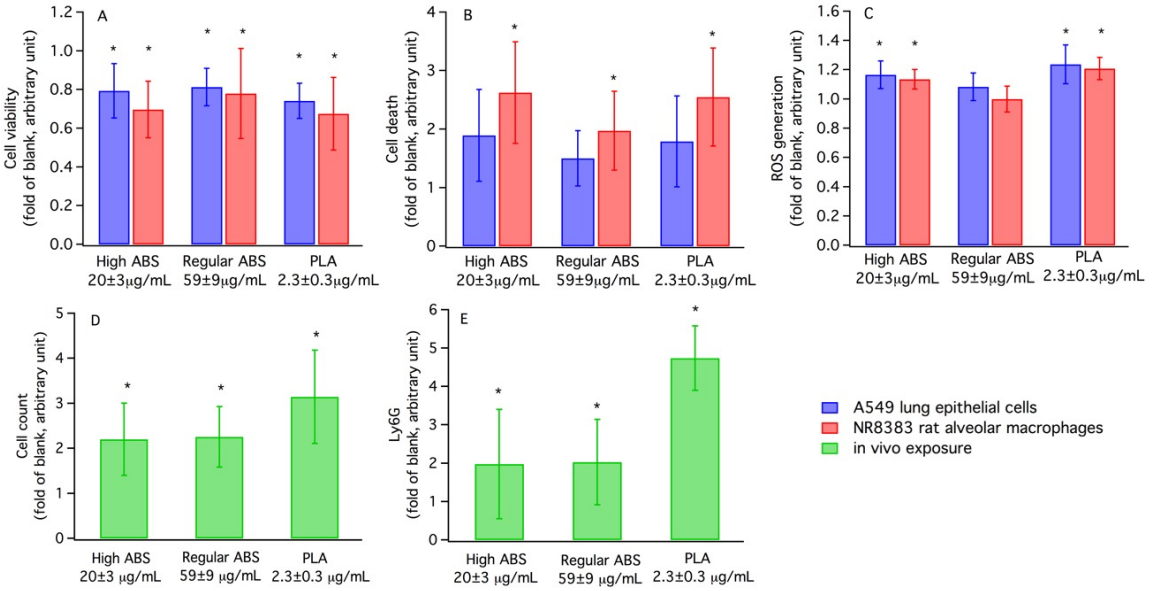

Figure 4.2 Biological toxicity responses for *in vitro* (A. cell viability, B. cell death, and C. cell ROS generation) and *in vivo* (D. cell count, E. neutrophils) analyses. Data expressed as fold change compared to blank filter extracts (blank). For the *in vitro* assays, error bar represents standard deviation, and for the *in vivo* standard error of the mean. Asterisks indicate significantly ($p < 0.05$) different from the blanks. Note that the estimated doses (shown in the plots) were different for the three different particle types, e.g., the dose for PLA-generated particles is much lower.

4.4.3 Inflammatory responses in mice lungs

For all the 3D printer emitted particles tested, a single intratracheal dose increased the total cell numbers significantly in the broncho alveolar lavage fluid (BALF) of mice after 24 h (Figure 4.2D), which was also found in the positive control group (fold change ~ 1.6). This is consistent with previous studies showing increases in BALF cell numbers

following exposure to polystyrene nanoparticles (Thorley et al. 2014) or PM (Pardo et al. 2015, 2016; Happo et al. 2010). The defense mechanism against intrusion of inhalable particles or PM is associated with mucociliary clearance and the activity of alveolar macrophages, and the latter leads to a sequence of events resulting in cell recruitment to the inflammatory site and activation in lungs (Harbeck 1998). Recruitment of neutrophils into lungs is an important feature of lung injury, as neutrophils increase inflammatory cytokines and chemokines that attract other neutrophils and other cell types (e.g., monocytes, macrophages, lymphocytes), indicating chronic inflammation (Pardo et al. 2015, 2016; Grommes and Soehnlein 2011). All tested particles produced a strong inflammatory response compared to the blank as indicated by the increase of neutrophils number (Figure 4.2E). The PLA-emitted particles produced the strongest inflammatory response, followed by Regular ABS and High ABS. In addition, the increase of neutrophils was the highest among all inflammatory cells (macrophages and monocytes) tested, suggesting their central role (not shown). This inflammatory response in mice lungs showed potential adverse health effects of 3D printer emitted particles, consistent with other studies that showed asthma development (House et al. 2017), or increased rates of respiratory symptoms (Chan et al. 2017) for human exposed to 3D printer emissions.

4.4.4 Oxidative stress induced by particles, cellular and acellular results

The cell-free DTT assay showed that the water-soluble OP^{DTT}_{m} was below LOD, while the total particle OP^{DTT}_{m} was above LOD (Figure 4.12), for all the particles tested (High ABS, Regular ABS, PLA and nylon). This was also consistent with the SEM result that particles were normally water insoluble (Figure 4.9), indicating that the surface

properties or adsorbed compounds on the particle surfaces were producing the observed OP^{DTT}_{m}.

Comparison among the biological toxicity responses to different particles is limited since the doses administered varied, as a result of widely differing particle emission rates for different filaments. However, some general conclusions can be made. A consistency of various biological responses showed PLA emitted particles induced similar levels of responses as ABS emitted particles, but at much lower doses (Figure 4.2), indicating PLA emitted particles are potentially more toxic on a particle mass basis. However, biological toxicity response also depends on properties other than dose (e.g., particle size and its ability to penetrate cells and tissues, cell lines and interaction mechanism) (Peixoto et al. 2017; Perrone et al. 2013; Grass et al. 2010). For example, nanoparticles were found to be more toxic than larger-sized particles of the same material and dose (Oberdörster et al. 1994), causing inflammation and oxidative stress (Nel et al. 2006). PLA emitted particles were the smallest in average size, which indicates they are potentially easier to be transported into cells, and further causing cell damages. Differences in toxicity are also consistent with differences in particle chemical composition, as noted above.

Direct application of our results with health studies is not possible, but comparisons of OP^{DTT}_{m} with ambient aerosols (i.e., $PM_{2.5}$) and emissions from various sources are possible, since significant OP^{DTT}_{m} data sets are available (Shiraiwa et al. 2017; Fang et al. 2015; Verma et al. 2015). Figure 4.3 shows a comparison summary of selected studies. Ambient $PM_{2.5}$ aerosol OP^{DTT}_{m} varies from about 20 to 60 pmol/min/μg, based on data from a range of sites; OP^{DTT}_{m} of emissions from incomplete combustion (e.g.,

diesel engine exhaust and biomass burning) is 50 – 150 pmol/min/μg (Shiraiwa et al. 2017). Only PLA has OP^{DTT}_m comparable to ambient levels and combustion emissions (Figure 4.3). Furthermore, in Atlanta, large population epidemiological studies have suggested links between DTT assay measured OP and adverse cardiorespiratory effects (Abrams et al. 2017; Bates et al. 2015), and the average OP^{DTT}_m levels were about 30 pmol/min/μg (Fang et al. 2015). In this study, OP^{DTT}_m for nylon and ABS were factors of 4 to 30 lower than that value, while OP^{DTT}_m for PLA was about a factor of 3 higher (Figure 4.3).

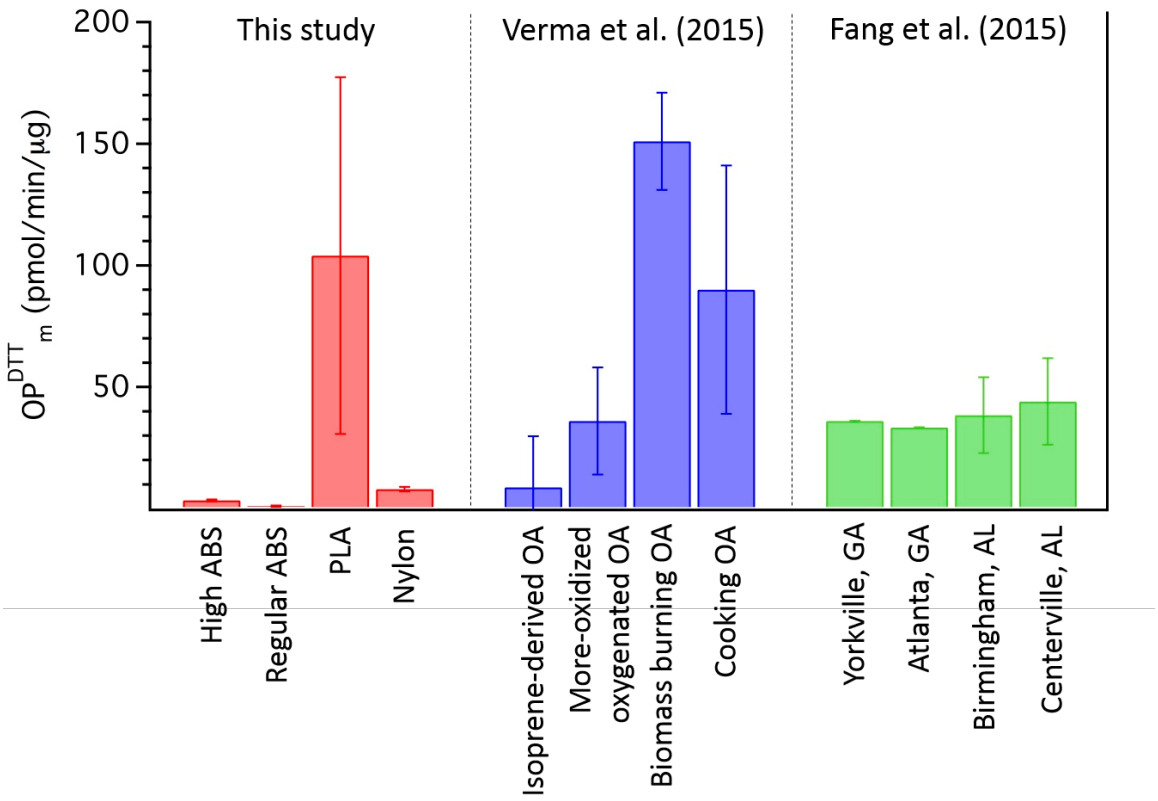

Figure 4.3 OP^{DTT}_m measured in this study (High ABS, Regular ABS, PLA, Nylon), compared to previous ambient studies on specific sources of organic aerosol (OA) (Verma et al. 2015) and $PM_{2.5}$ at various locations (Fang et al. 2015). Each error bar is the standard deviation of data in each group. An extensive tabulation of OP^{DTT}_m has been reported elsewhere (Shiraiwa et al. 2017).

Although OP^{DTT}_m provides some indication of the aerosol toxicity, potential adverse health effects depend on actual exposures, which are associated with particle emissions during printing (Table 4.3). To consider exposures, measures of toxicity (e.g., OP^{DTT}_m) can be multiplied with particle emissions from the corresponding filaments (e.g., mass yield, which is the mass of emitted particles per mass of object printed) (Zhang et al. 2017). The product is the assay response per mass of the object printed (i.e., $OP^{DTT}_m \times$ [mass yield] = OP^{DTT}/object mass, referred to here as OP^{DTT}_{om}). By this analysis, ABS filaments are potentially much greater health concerns since their emissions are orders of

magnitude higher than PLA (Gümperlein et al. 2018), resulting in OP^{DTT}_{om} of ABS factors of 5 – 10 higher than that of PLA.

Overall, this study suggests that particles emitted from 3D printers have the potential to produce adverse health impacts that depend on filament materials used. Our observed increases in cell death, oxidative stress, and inflammation are mechanisms that negatively affect lung function, which may increase the risk of respiratory disorders and complications. However, in this study, actual exposures have not been assessed, which will determine the severity, if any, of the responses. Exposure concentrations depend on many factors that need to be considered, including the conditions under which the printer operates (e.g., size of space, heating, ventilation and air conditioning specifications), a person's proximity to the printer, and the duration of exposure.

4.5 Acknowledgement

This work was funded by the Chemical Safety Research Program of Underwriters Laboratories Inc. The SEM analysis was conducted at the Irving and Cherna Moskowitz Center for Nano and BioNano Imaging (Weizmann Institute). Yinon Rudich acknowledges support by Astrachan Olga Klein.

4.6 Supplemental Information

4.6.1 Estimation of particle concentrations in extracts

4.6.1.1 Samples for biological analysis

The filter was extracted in 11 mL of deionized water (DI) via sonication (Ultrasonic Cleaner, VWR International LLC., West Chester, PA, USA) in a sterile polypropylene centrifuge tube (VWR International LLC., Suwanee, GA, USA) for 1 h. 10 mL of the liquid with suspended particles was used for the toxicity analysis and the remaining 1 mL was re-aerosolized using a continuous flow ultrasonic nebulizer (U-5000AT, Cetac Technologies, Omaha, NE, USA). The nebulized aerosols were dried, neutralized and particle number distributions measured with the SMPS (scan mobility particle sizer) used in the chamber measurements. Particle mass distributions were calculated from the number distributions assuming spherical particles of unit density. Comparison of the size distribution measured in the chamber to the size distribution following extraction and re-aerosolization (nebulizer output) are shown in Figure 4.4. The upper size limit of 0.3 μm for the SMPS we used was sufficient to capture the mass distribution from the nebulizer.

The mass concentration of the aerosols in the liquid sample (m_{liq}) was determined by the nebulized aerosol concentration and the nebulizer efficiency:

$$m_{liq} = \frac{\frac{nebulized\ aerosol\ mass\ in\ gas\ flow}{volume\ of\ liquid\ into\ nebulizer}}{\eta_{neb}} = \frac{\sum(m_i) \times Q_g}{Q_l \times \eta_{neb}} \qquad (31)$$

m_i is the total mass concentration for i^{th} particle size in the gas flow, sum over all sizes gives the total mass concentration of the nebulized aerosol (unit μg/m^3 gas); Q_g is nitrogen gas flow rate supplied to the nebulizer; Q_l is the flow rate of the liquid sample pumped to the nebulizer and η_{neb} is the nebulizer efficiency.

The reported efficiency for the nebulizer we used is between 10% to 15% (Cetac Technologies 2018). This is within the range determined from other studies. For example, 8% ± 2% for sulfate aerosol quantified with an aerosol mass spectrometer (AMS) (Xu et al. 2017) and 11.4% ± 0.8% for black carbon (Ohata et al. 2011). Therefore, here we assumed an average nebulization efficiency of 13%. We also assumed the uncertainty of nebulization efficiency to be 10%, combining with an estimated 10% uncertainty in mass measurement with the SMPS due to missing larger particles, the overall uncertainty was estimated at ~ 15%. Therefore, the estimated particle mass concentrations in liquid samples for High ABS, Regular ABS and PLA were 20 ± 3 µg/mL, 59 ± 9 µg/mL and 2.3 ± 0.3 µg/mL (details in Table 4.1).

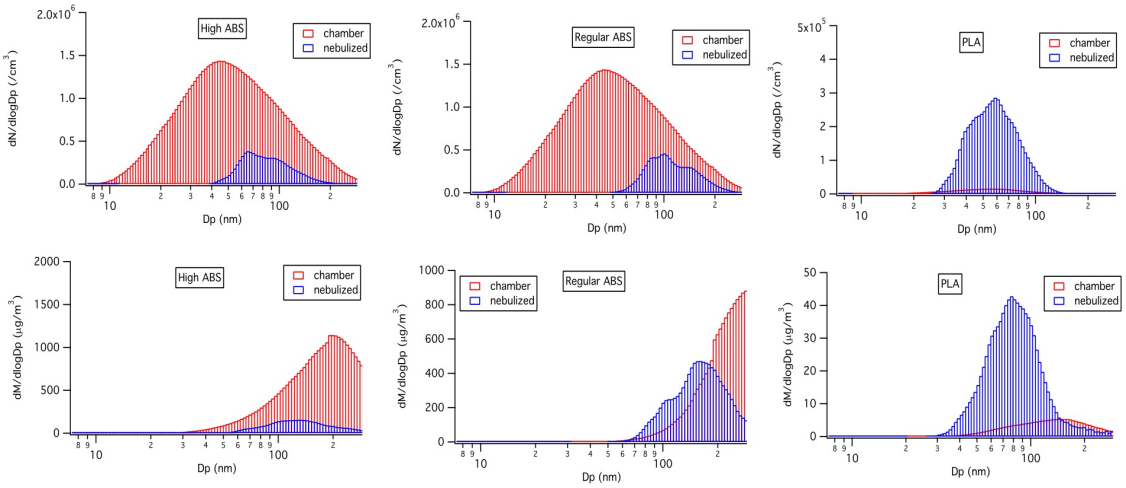

Figure 4.4 The number and mass distributions for particles in the chamber and nebulized for the three samples. (The plots are to contrast the shape of the size distributions; concentrations are not directly comparable.)

Table 4.1 Particle concentrations in extracted liquid samples used in biological analysis.

	High ABS	Regular ABS	PLA
Concentration in nebulizer outflow			
N (#/mL)	2.29×10^{9}	3.68×10^{9}	1.36×10^{9}
S (cm^2/mL)	1.22	3.00	0.22
V (cm^3/mL)	2.63×10^{-6}	7.63×10^{-6}	2.91×10^{-7}
M (μg/mL)	2.64	7.64	0.30
Concentration in liquid sample calculated using nebulizer efficiency			
N (#/mL)	$(1.76\pm0.26)\times10^{10}$	$(2.83\pm0.42)\times10^{10}$	$(1.05\pm0.16)\times10^{10}$
S (cm^2/mL)	9.40±1.41	23.09±3.46	1.71±0.26
V (cm^3/mL)	$(3.29\pm0.49)\times10^{-5}$	$(9.54\pm1.43)\times10^{-5}$	$(3.64\pm0.54)\times10^{-6}$
M (μg/mL)	20.29±3.04	58.75±8.81	2.28±0.34
Print time (h)	7.20	7.16	8.96

4.6.1.2 Samples for total DTT analysis

The filter was extracted in 4.9 mL DI and 1.4 mL potassium phosphate buffer via sonication for 1 h. 0.7 mL of DTT solution was added for reaction, resulting a total liquid volume (V_l) of 7 mL. For the total DTT analysis, since the filter remained in the liquid, allowing particles that haven't been extracted into liquid phase to react as well, the concentration of particles for total DTT analysis (m_{DTT}) can be calculated as:

$$m_{DTT} = \frac{M_{ch}}{V_l} \tag{32}$$

where M_{ch} is the mass collected on the filter calculated using the measured chamber concentration; V_l is the volume of liquid in the vial. Since particles were not water-soluble, particle surface area may also be important. The particles collected on filters

(M_{ch}) and the estimated concentrations for particles used in the total DTT analysis (m_{DTT}) are shown in Table 4.2.

Table 4.2 Particle concentrations in samples used for total DTT analysis (3 samples for each filament).

	High ABS	Regular ABS	PLA	Nylon
M_{ch}: Particles collected on filters calculated from chamber measurements				
N (#)	$(1.90\pm0.74)\times10^{12}$	$(3.48\pm0.15)\times10^{11}$	$(1.56\pm0.97)\times10^{11}$	$(7.44\pm2.92)\times10^{10}$
S (cm^2)	359.17±124.41	413.71±43.47	16.47±10.86	60.57 ±10.53
V (cm^3)	$(8.32\pm2.67)\times10^{-4}$	$(3.23\pm0.93)\times10^{-3}$	$(2.55\pm1.67)\times10^{-5}$	$(2.74\pm0.36)\times10^{-4}$
M (μg)	832.34±266.78	3233.18±932.07	25.40±16.81	273.87±36.41
m_{DTT}: Paricle concentrations in liquid samples				
N (#/mL)	$(2.71\pm1.05)\times10^{11}$	$(4.97\pm0.22)\times10^{10}$	$(2.23\pm1.38)\times10^{10}$	$(1.06\pm0.42)\times10^{10}$
S (cm^2/mL)	51.31±17.77	59.10±6.21	2.35±1.55	8.65 ±1.50
V (cm^3/mL)	$(1.19\pm0.38)\times10^{-4}$	$(4.62\pm1.33)\times10^{-4}$	$(3.64\pm2.39)\times10^{-6}$	$(3.91\pm0.52)\times10^{-5}$
M (μg/mL)	118.90±38.11	461.88±133.15	3.63±2.40	39.12±5.20
Print time (h)	4.86±2.27	7.10±0.30	17.71±4.28*	7.17±0.40

* extended sample time to collect enough mass on filters to get detectable signal. Note that the total DTT analysis differs from the biological tests in that the filter with collected particles remains in the reaction vial in contact with the DTT. Thus in this case, the mass concentrations of the aerosols are calculated differently than for the biological samples.

4.6.2 Particle characterization

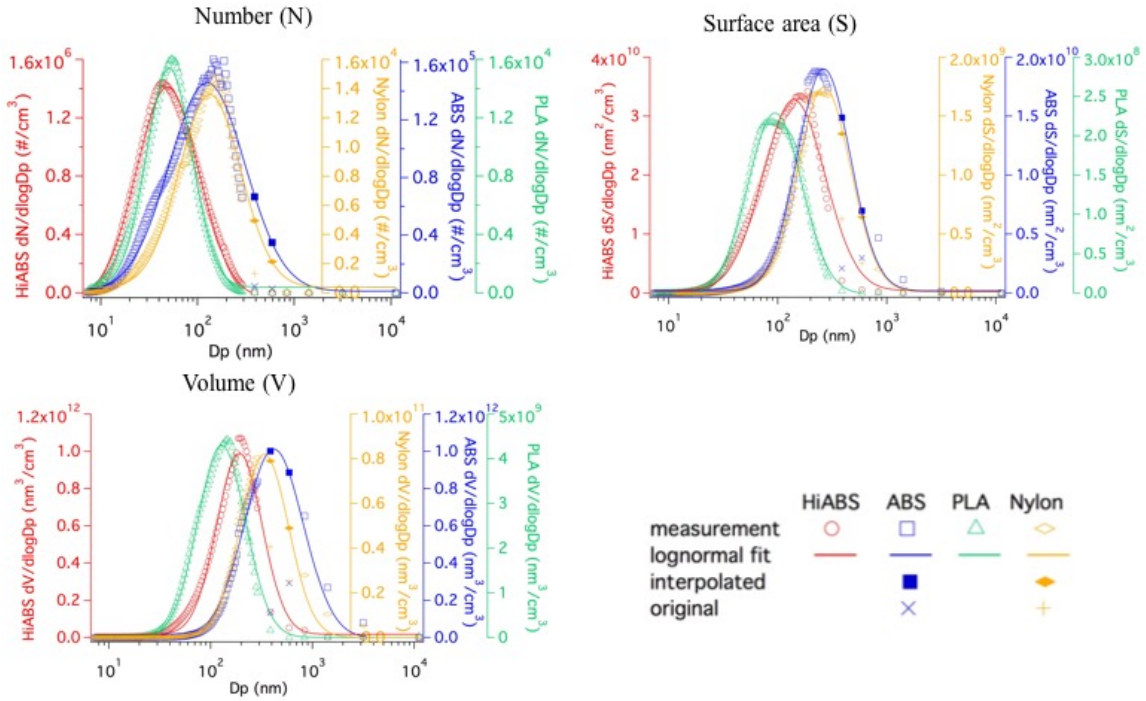

Figure 4.5 Average particle size distributions (Number, Surface Area and Volume) in the chamber measured during filter sampling interval with the corresponding lognormal fitting. The smallest two channels of OPC for ABS and nylon were not accurate due to instrumental noise and were replaced by interpolations from the fitting curves.

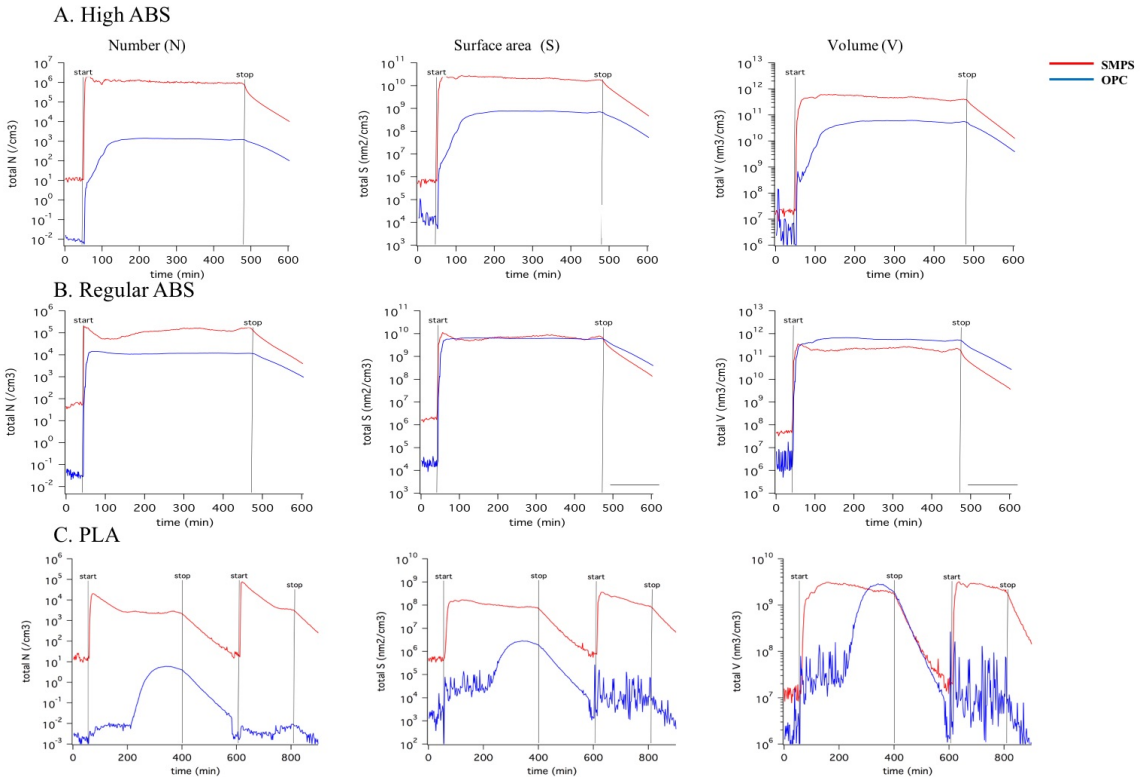

Figure 4.6 Particle concentration time series plots (size distribution integrals) measured in the chamber during filter sampling. Start and stop represent the time when extrusion started and stopped.

Table 4.3 Geometric mean diameter (D_{pg}, nm) and geometric standard deviation (σ_g) from lognormal distribution fit for average particle distributions in the chamber during sampling period (distributions shown in Figure 4.5); corresponding emission yields (emissions per mass of object printed) are also shown.

	High ABS		Regular ABS		PLA		Nylon	
Size	D_{pg}	σ_g	D_{pg}	σ_g	D_{pg}	σ_g	D_{pg}	σ_g
Number (N)	49.03	1.04	123.49	1.25	50.91	0.77	134.27	1.04
Surface area (S)	140.74	0.93	271.02	0.82	94.29	0.80	266.00	0.79
Volume (V)	191.74	0.73	417.88	0.94	128.35	0.76	337.95	0.77
Number yield (g^{-1})	1.42×10^{11}		1.52×10^{10}		1.35×10^{9}		1.58×10^{9}	
Surface area yield (cm^2/g)	25.24		10.64		0.24		1.33	
Volume yield (cm^3/g)	5.78×10^{-5}		5.93×10^{-5}		4.15×10^{-7}		6.18×10^{-6}	
Mass yield (μg/g)	57.79		59.33		0.42		6.18	

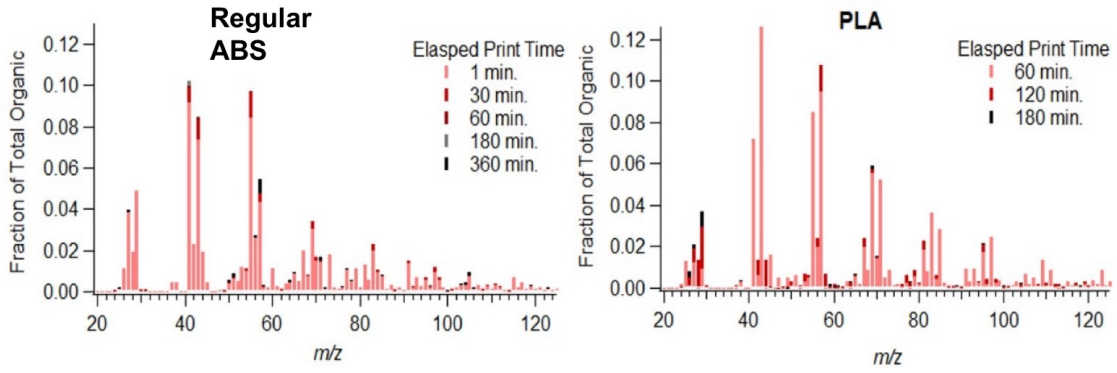

Figure 4.7 Mass spectra of the organic component of emitted particles for Regular ABS and PLA filaments throughout the print time, as measured by the aerosol mass spectrometer (AMS).

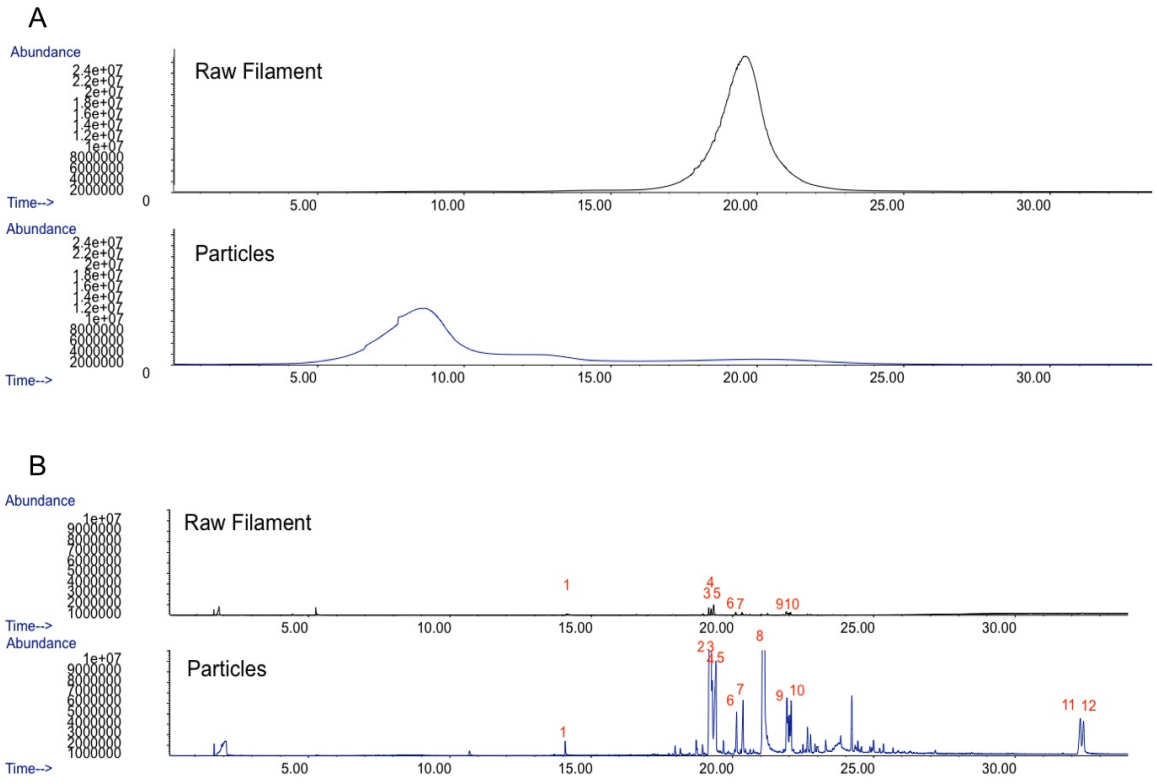

Figure 4.8 Chemical composition analysis of raw High ABS filament and the particles emitted from that filament measured by pyrolysis gas chromatography-mass spectrometry; A shows the evolved gas analysis results; B shows the thermal desorption/pyrolysis results. The peaks number correspond to the following compounds, 1: 2-Naphthalene carbonitrile; 2: n-Hexadecanoic acid; 3, 4, 5, 6, 7: Isomer of 2-[1-(4-Cyano-1,2,3,4-tetrahydronaphthyl)] propanenitrile; 8: Octadecanoic acid; 11: Irganox 1076; 9, 10, 12: unknown.

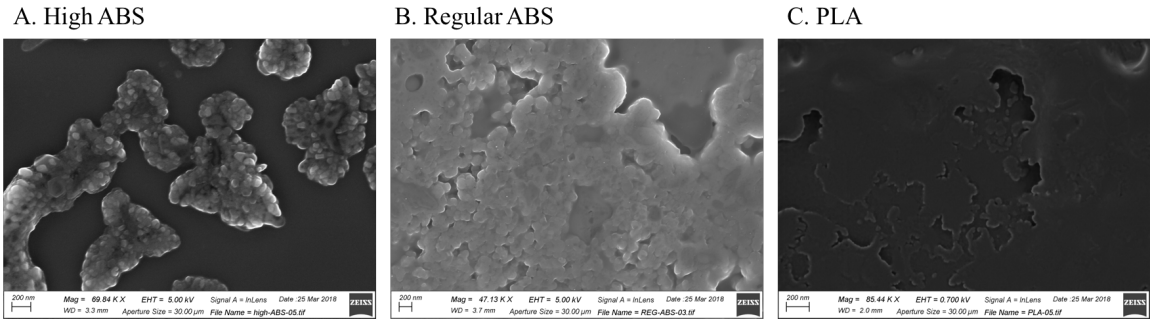

Figure 4.9 SEM images of (A) High ABS, (B) Regular ABS and (C) PLA emitted particles collected on filters and then extracted in water to produce aqueous suspensions for subsequent toxicity tests. The images are of the aqueous suspensions that have been dried for the SEM measurements, which caused the particle to agglomerate, as seen.

4.6.3 Toxicity of 3D printer emitted particles

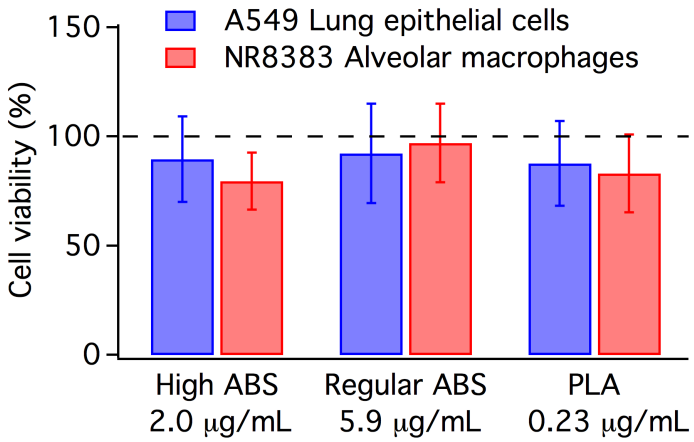

Figure 4.10 Cytotoxicity of 3D printer particles. Cells were exposed to the indicated concentration of three particle samples (High ABS, Regular ABS and PLA) and blank filter extract (Blank) for 24 hr. Untreated cells (not shown) were similar to the blank. Data represent fold change from blank in mean ± standard deviation.

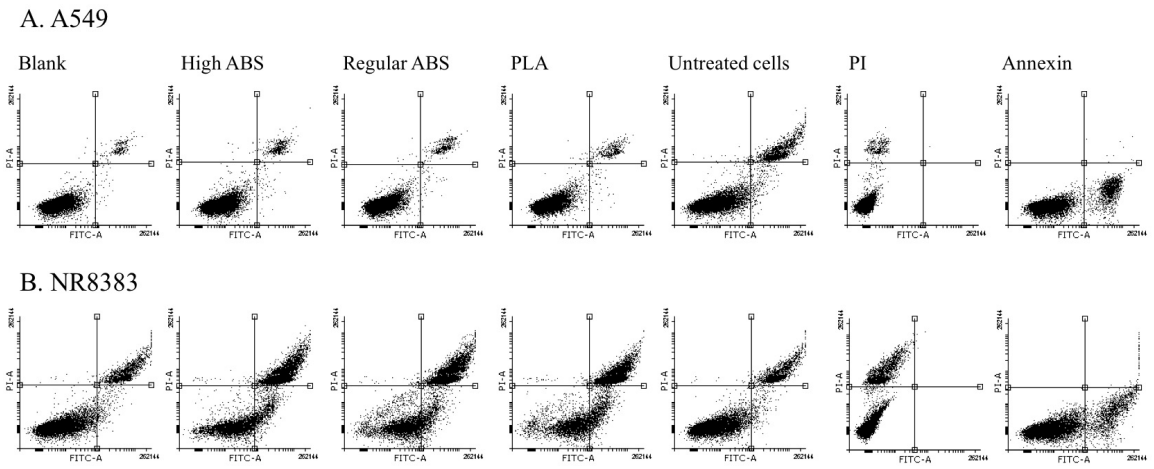

Figure 4.11 Total cell death of A549 and NR8383 after exposure to 3D printer emitted particles for 24 hr, assessed by MEBCYTO Apoptosis Kit (Annexin V-FITC kit), where necrotic cells are stained with propidium iodide (PI) and Annexin V (right top quadrant) while apoptotic cells are stained with only Annexin V (right bottom quadrant). Untreated cells, cells stained only with PI and cells stained only with Annexin V were used as controls.

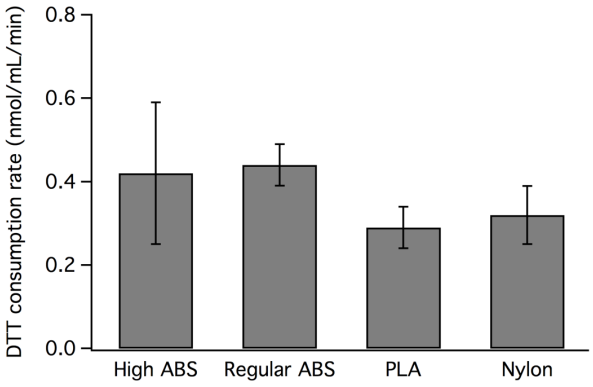

Figure 4.12 Total DTT assay results for 3D printer emitted particles (High ABS, Regular ABS, PLA and Nylon). Particle concentrations in the samples can be found in Table 4.2. The data are corrected by blanks (blank filter extract). Error bars are standard deviation (n = 3).

CHAPTER 5. FUTURE WORK

This thesis investigated particle emissions from consumer level FDM 3D printers. First, we characterized particle emissions in a chamber using a standard emission test method, under various print conditions. We found filament material, extrusion temperature and filament brand were the most important factors. Second, we discussed the particle formation mechanism and dynamics using a method of moments lognormal aerosol dynamic model. The measurements indicated that particles are formed from the process of new particle formation of the semi-volatile compounds emitted when heating the filament, thus particle emissions can be linked to the properties of precursors, which also explained the different effects of printing conditions on emissions. Last, we analyzed particle chemical composition and assessed the potential toxicity of particles. ABS emitted particles were not like ABS monomers in chemical composition, while PLA emitted particles showed similarity to PLA monomers. For particle toxicity, PLA emitted particles were consistently found to be more toxic than ABS emitted particles on a particle mass basis, via different assessing methods. Overall, we have found the particle emissions from 3D printing are significant, not benign, and exposure should be avoided.

Many research groups have done characterization of particle emissions from 3D printers, however, the results are not actually comparable due to different methods applied. The characterizations of particle (and VOC) emissions should follow a standardized testing protocol, which should include guidance for experimental setup, operation procedure, and data analysis method. In that way, emissions from more 3D printers running different materials can be tested in the same manner by different groups,

and a large data set of 3D printer emissions can be built. This will help the 3D printing market to set a standard for emissions and further encourage manufacturers to produce printers and filaments that generate less emissions.

Given the complexity of different operating conditions (i.e., printer and filament combinations), a test method for only the filaments (i.e., without printing an object with a printer) may be needed. This test method, if available, will largely reduce the workload of testing different printer and filament combinations. A way to develop this method can be to heat a portion of filament to print temperature and measure the particle emissions, and then relate a particle emission parameter (e.g., yield) of only heating the filament to that tested with a printer. This filament test procedure should imitate the particle emission process from printing as much as possible, i.e., without changing the particle formation mechanism or environmental conditions. One way is to have an extruder in a small chamber and extrude filament at the desired temperature and a constant rate, and monitor particle concentrations at the same time. Our preliminary results showed there was no clear relationship between the particle emissions from extruding the filament with an extruder only and those from printing with a printer under the same extrusion temperature. This indicated that the printer design may also play an important role on affecting particle emissions. For example, the build plate beneath the extruder and the fan attached to the extruder are potentially changing the parameters involved in new particle formation process and the dynamics of emitted particles. Another way to characterize filament may be printing different filaments using the same printer and the same setting.

As we have found the particles are potentially formed from additives (e.g., pigments) in filaments, it is important to understand the composition of raw filaments,

especially additives with low saturation vapor pressures. Determining the precursor species of particle formation is important for minimizing particle emissions, however, this work may be complex that involves filament composition analysis and measurement of semi-volatile compounds. Manufacturers providing accurate details of composition of raw material may help targeting potential precursors. An aerosol dynamic model simulating particle dynamic processes may also be helpful by providing estimated properties of potential precursors. We also found extrusion temperature to be important for particle emissions. Therefore, printer and filament manufacturers should encourage customers to run the printer at the lowest extrusion temperature as possible, and instead of setting a fixed relative high extruder temperature for all the filaments, it may be beneficial for users if they can adjust extrusion temperature, in order to reduce emissions. In addition to eliminate particle emissions from formation, techniques removing formed particles can also be effective. For example, printer manufacturers may design printer enclosures with air purifying systems, as it is found that a sealed enclosure with high-efficiency gas and particle filtration is capable of reducing particle and gas exposures (Azimi et al. 2017; Yi et al. 2016). Another suggestion for mitigating particle emissions is by thermophoresis; our calculations showed its potential to remove newly formed small particles, while modified printer extruders need to be tested for further application.

Particle properties (e.g., size, chemical composition) are related to its toxicity. For example, metals in particles are found to be associated with toxic responses (Salvi and Holgate 1999), however metals in 3D printer emitted particles have not been systematically analyzed. Metallic composition in particles need to be analyzed by measurements with high sensitivity, and may be further related to toxicity assessments. In

addition, 3D printer emitted particles are reported to be mainly organic compounds, however the detailed compositions have not been specified. Knowing the composition of particles will help understanding not only particle formation mechanism, but also their potential toxicity.

Our preliminary toxicity assessment showed adverse effects of 3D printer emitted particles to mice and different cell lines, however, the experiments were not carried out using the same dose, which is technically difficult due to the large variations of emissions from different print jobs and uncertainties associated with particle sample preparation. More *in vivo* and *in vitro* cellular experiments may be needed to obtain dose-response curves, from which the toxic response can be calculated for different doses and approximately be compared between particles emitted from different filaments. Other assays based on ROS mechanism or assays based on other mechanisms may also be useful in exploring the toxicity of 3D printer emitted particles, however, many of the cellular and acellular assays require transferring particles from air to an aqueous media, which is potentially varying particle properties and causing uncertainties. Therefore, exposing 3D printer emissions to subjects (e.g., animals, cells or humans) directly is a more straightforward way of studying exposure toxicity if applicable.

APPENDIX A. EXPERIMENTAL SETUP

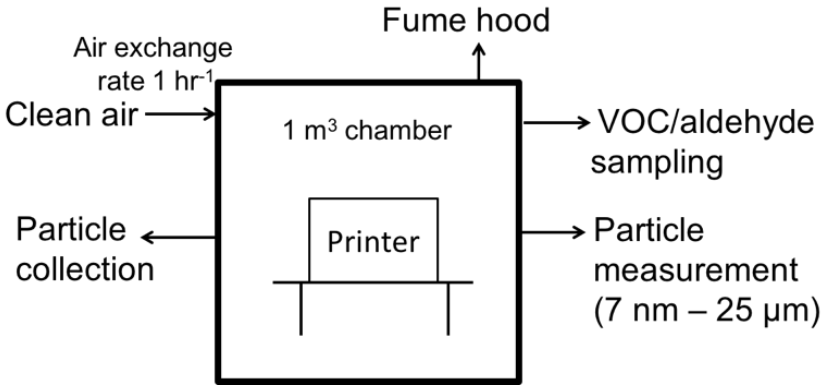

Figure A.1 Schematic diagram of experimental chamber system.

APPENDIX B. SYMBOLS IN AEROSOL DYNAMIC MODEL

h	Boundary layer thickness
b	Width of control volume, 1 mm
D	Diffusion coefficient of vapor
DR	Dilution ratio
f	Condensation factor
G	Aerosol growth rate
h	Boundary layer thickness
h_{av}	Height of control volume
I	Nucleation rate
I’	Dimensionless nucleation rate
K	Coagulation coefficient
k	Order of moment
k^*	Number of monomers in the critical size nucleus
k_B	Boltzmann’s constant
Kn_1	Monomer Knudsen number
M	Moment of particle distribution
M_0	0^{th} moment of particle distribution, particle number concentration
M_1	1^{st} moment of particle distribution, particle volume concentration
M_2	2^{nd} moment of particle distribution
N	Particle number concentration
N’	Dimensionless particle number concentration
n_1	Monomer concentration

n_s	Monomer concertation at saturation
P	Partial vapor pressure
P_s	Saturation vapor pressure
R	Vapor generation rate
R’	Dimensionless vapor generation rate
Re	Reynolds number
r_1	Monomer radius
r_g	Geometric mean radius
r_g’	Dimensionless geometric mean radius
S	Saturation ratio
s_1	Monomer surface area
t	Residence time
T	Temperature of vapor
t_{sim}	Simulation time
u	Velocity of air
V	Dimensionless particle volume concentration
V_2	Dimensionless 2nd particle volume moment
v, $\bar{v}$	Particle volume
v^*	Critical volume of the newly formed particle
v_1	Monomer volume
v_g	Particle geometric mean volume
x	Length of control volume, the effective length of extruded filament
B	Collision frequency function
γ	Surface energy
ϵ	Dimensionless condensation coefficient for 2nd moment

ϵ_C	Dimensionless condensation coefficient for 2nd moment in continuum regime
ϵ_{FM}	Dimensionless condensation coefficient for 2nd moment in free molecular regime
ζ	Dimensionless coagulation coefficient for 2nd moment
ζ_C	Dimensionless coagulation coefficient for 2nd moment in continuum regime
ζ_{FM}	Dimensionless coagulation coefficient for 2nd moment in free molecular regime
η	Dimensionless condensation coefficient for 1st moment
η_C	Dimensionless condensation coefficient for 1st moment in continuum regime
η_{FM}	Dimensionless condensation coefficient for 1st moment in free molecular regime
θ	Dimensionless residence time
λ	Mean free path
μ	Viscosity of air
ξ	Dimensionless coagulation coefficient for 0th moment
ξ_C	Dimensionless coagulation coefficient for 0th moment in continuum regime
ξ_{FM}	Dimensionless coagulation coefficient for 0th moment in free molecular regime
ρ_g	Density of air
Σ	Dimensionless surface tension
σ_g	Particle geometric standard deviation
τ	Characteristic time for particle growth

REFERENCES

Abrams, J.Y., Weber, R.J., Klein, M., Samat, S.E., Chang, H.H., Strickland, M.J., Verma, V., Fang, T., Bates, J.T., Mulholland, J.A., Russell, A.G., and Tolbert, P.E. (2017). Associations between Ambient Fine Particulate Oxidative Potential and Cardiorespiratory Emergency Department Visits. *Environ Health Persp,* 125(10).

Adams, K., Bankston, J., Barlow, A., Holdren, M.W., Meyer, J., and Marchesani, V.J. (1999). Development of Emission Factors for Polypropylene Processing. *J Air & Waste Manag Assoc,* 49(1):49–56.

Alto, P. (2015). Global 3D printing market to reach $20.2 billion in 2019 | Canalys. Available at http://www.canalys.com/newsroom/global-3d-printing-market-reach-202-billion-2019 (Accessed 15 June 2016).

Asbach, C., Fissan, H., Stahlmecke, B., Kuhlbusch, T.A.J., and Pui, D.Y.H. (2009). Conceptual limitations and extensions of lung-deposited Nanoparticle Surface Area Monitor (NSAM). *J Nanopart Res,* 11(1):101–109.

ASTM (2013). ASTM D6670-13, Standard Practice for Full-Scale Chamber Determination of Volatile Organic Emissions from Indoor Materials/Products. West Conshohocken, PA: American Society for Testing and Materials International.

Ayres, J.G., Borm, P., Cassee, F.R., Castranova, V., Donaldson, K., Ghio, A., Harrison, R.M., Hider, R., Kelly, F., Kooter, I.M., Marano, F., Maynard, R.L., Mudway, I., Nel, A., Sioutas, C., Smith, S., Baeza-Squiban, A., Cho, A., Duggan, S., and Froines, J. (2008). Evaluating the Toxicity of Airborne Particulate Matter and Nanoparticles by Measuring Oxidative Stress Potential–A Workshop Report and Consensus Statement. *Inhal Toxicol,* 20(1):75–99.

Azimi, P., Fazli, T., and Stephens, B. (2017). Predicting Concentrations of Ultrafine Particles and Volatile Organic Compounds Resulting from Desktop 3D Printer Operation and the Impact of Potential Control Strategies. *J Ind Ecol,* 21(S1):S107–S119.

Azimi, P., Zhao, D., Pouzet, C., Crain, N.E., and Stephens, B. (2016). Emissions of Ultrafine Particles and Volatile Organic Compounds from Commercially

Available Desktop Three-Dimensional Printers with Multiple Filaments. *Environ Sci Technol,* 50(3):1260–1268.

Bai, H. and Biswas, P. (1990). Deposition of lognormally distributed aerosols accounting for simultaneous diffusion, thermophoresis and coagulation. *J Aerosol Sci,* 21(5):629–640.

BAM, Federal Institute for Materials Research and Testing. (2012). Test Method for the Determination of Emissions from Hardcopy Devices within the Award of the Blue Angel Ecolabel for Equipment with Printing Function according to RAL-UZ-171. St. Augustin, Germany: BAM.

Bandyopadhyay, A., Gualtieri, T. PL., Bose, S. (2015). Global Engineering and Additive Manufacturing, in *Additive Manufacturing*. Bandyopadhyay, A. and Bose, S., eds, Boca Raton, FL: CRC Press.

Barrett, J.C. and Webb, N.A. (1998). A comparison of some approximate methods for solving the aerosol general dynamic equation. *J Aerosol Sci,* 29(1–2):31–39.

Bates, J.T., Weber, R.J., Abrams, J., Verma, V., Fang, T., Klein, M., Strickland, M.J., Sarnat, S.E., Chang, H.H., Mulholland, J.A., Tolbert, P.E., and Russell, A.G. (2015). Reactive Oxygen Species Generation Linked to Sources of Atmospheric Particulate Matter and Cardiorespiratory Effects. *Environ Sci Technol,* 49(22):13605–13612.

Bekö, G., Weschler, C.J., Wierzbicka, A., Karottki, D.G., Toftum, J., Loft, S., and Clausen, G. (2013). Ultrafine Particles: Exposure and Source Apportionment in 56 Danish Homes. *Environ Sci Technol, 47*, 10240–10248.

Berman, B. (2012). 3-D printing: The new industrial revolution. *Business Horizons,* 55(2):155–162.

Bilde, M. and Pandis, S.N. (2001). Evaporation Rates and Vapor Pressures of Individual Aerosol Species Formed in the Atmospheric Oxidation of α- and β-Pinene. *Environ Sci Technol,* 35(16):3344–3349.

Biswas, P., Li, X. M., and Pratsinis, S.E. (1989). Optical wave-guide preform fabrication silica formation and growth in a high-temperature aerosol reactor. *J Appl Phys*, *65*:2445-2450.

Biswas, P., Lin, W.Y., and Wu, C.Y. (1992). Formation and emission of metallic aerosols from incinerators. *J Appl Phys,* 23:273–276.

Biswas, P., Wu, C.Y., Zachariah, M.R., and McMillin, B. (1997). Characterization of iron oxide-silica nanocomposites in flames: Part II. Comparison of discrete-sectional model predictions to experimental data. *J Mater Res,* 12(03):714–723.

Bradley, R.S., Bird, C.L., and Jones, F. (1960). The vapour pressures and heats of sublimation of some disperse dyes. *Trans Faraday Soc,* 56:23–28.

Brock, J.R. and Oates, J. (1987). Moment simulation of aerosol evaporation. *J Aerosol Sci,* 18(1):59–64.

Brook, R.D., Rajagopalan, S., Pope, C.A., Brook, J.R., Bhatnagar, A., Diez-Roux, A.V., Holguin, F., Hong, Y., Luepker, R.V., Mittleman, M.A., Peters, A., Siscovick, D., Smith, S.C., Whitsel, L., Kaufman, J.D., and on behalf of the American Heart Association Council on Epidemiology and Prevention, Council on the Kidney in Cardiovascular Disease, and Council on Nutrition, Physical Activity and Metabolism (2010). Particulate Matter Air Pollution and Cardiovascular Disease: An Update to the Scientific Statement From the American Heart Association. *Circulation,* 121(21):2331–2378.

Brown, D.P., Kauppinen, E.I., Jokiniemi, J.K., Rubin, S.G., and Biswas, P. (2006). A method of moments based CFD model for polydisperse aerosol flows with strong interphase mass and heat transfer. *Comput Fluids,* 35(7):762–780.

Byeon, J.H. and Kim, J.-W. (2012). Particle emission from laser printers with different printing speeds. *Atmos Environ,* 54:272–276.

Cetac Technologies. U5000AT+ ultrasonic nebulizer datasheet. (retrieved January 20, 2018).

Chan, F., Rajaram, N., House, R., Kudla, I., Lipszyc, J., Tarlo, S.M. (2017). Potential Respiratory Effects From 3-D Printing. Presented at the American Thoracic Society, Washington, DC.

Chao, J., Lin, C.T., and Chung, T.H. (1983). Vapor Pressure of Coal Chemicals. *Journal of Physical and Chemical Reference Data,* 12(4):1033–1063.

Charvet, A., Bau, S., Bémer, D., and Thomas, D. (2015). On the Importance of Density in ELPI Data Post-Treatment. *Aerosol Sci Tech,* 49(12):1263–1270.

Cho, A.K., Sioutas, C., Miguel, A.H., Kumagai, Y., Schmitz, D.A., Singh, M., Eiguren-Fernandez, A., and Froines, J.R. (2005). Redox activity of airborne particulate matter at different sites in the Los Angeles Basin. *Environ Res,* 99(1):40–47.

Collaborators (2016). Global, regional, and national comparative risk assessment of 79 behavioural, environmental and occupational, and metabolic risks or clusters of risks, 1990–2015: a systematic analysis for the Global Burden of Disease Study 2015. *Lancet,* 388(10053):1659–1724.

Costa, S., Ferreira, J., Silveira, C., Costa, C., Lopes, D., Relvas, H., Borrego, C., Roebeling, P., Miranda, A.I., and Paulo Teixeira, J. (2014). Integrating Health on Air Quality Assessment—Review Report on Health Risks of Two Major European Outdoor Air Pollutants: PM and NO_2. *J Toxicol Env Heal B,* 17(6):307–340.

Curtius, J. (2006). Nucleation of atmospheric aerosol particles. *Comptes Rendus Physique,* 7(9–10):1027–1045.

DeCarlo, P.F., Kimmel, J.R., Trimborn, A., Northway, M.J., Jayne, J.T., Aiken, A.C., Gonin, M., Fuhrer, K., Horvath, T., Docherty, K.S., Worsnop, D.R., and Jimenez, J.L. (2006). Field-Deployable, High-Resolution, Time-of-Flight Aerosol Mass Spectrometer. *Anal Chem,* 78(24):8281–8289.

Deng, X., Zhang, F., Wang, L., Rui, W., Long, F., Zhao, Y., Chen, D., and Ding, W. (2014). Airborne fine particulate matter induces multiple cell death pathways in human lung epithelial cells. *Apoptosis,* 19(7):1099–1112.

Deng, Y., Cao, S.-J., Chen, A., and Guo, Y. (2016). The impact of manufacturing parameters on submicron particle emissions from a desktop 3D printer in the perspective of emission reduction. *Build Environ,* 104:311–319.

Donaldson, K., Li, X.Y., and MacNee, W. (1998). Ultrafine (nanometre) particle mediated lung injury. *J Aerosol Sci,* 29(5):553–560.

Drewnick, F., Hings, S.S., DeCarlo, P., Jayne, J.T., Gonin, M., Fuhrer, K., Weimer, S., Jimenez, J.L., Demerjian, K.L., Borrmann, S., and Worsnop, D.R. (2005). A New

Time-of-Flight Aerosol Mass Spectrometer (TOF-AMS)—Instrument Description and First Field Deployment. *Aerosol Sci Tech,* 39(7):637–658.

ECMA International. (2015). ECMA-328 Standard 7th Edition, Determination of Chemical Emission Rates from Electronic Equipment. ECMA International, Geneva. www.ecma-international.org.

Fang, T., Verma, V., Bates, J.T., Abrams, J., Klein, M., Strickland, M.J., Sarnat, S.E., Chang, H.H., Mulholland, J.A., Tolbert, P.E., Russell, A.G., and Weber, R.J. (2016). Oxidative potential of ambient water-soluble $PM_{2.5}$; in the southeastern United States: contrasts in sources and health associations between ascorbic acid (AA) and dithiothreitol (DTT) assays. *Atmos Chem Phys,* 16(6):3865–3879.

Fang, T., Verma, V., Guo, H., King, L.E., Edgerton, E.S., and Weber, R.J. (2015). A semi-automated system for quantifying the oxidative potential of ambient particles in aqueous extracts using the dithiothreitol (DTT) assay: results from the Southeastern Center for Air Pollution and Epidemiology (SCAPE). *Atmos Meas Tech,* 8(1):471–482.

Ferdinand, J.-P., Flämig, H., Petschow, U., Steinfeldt, M., and Worobei, A. (2016). Assessing the Environmental Impact of Decentralized Value-Chain Patterns Involving 3D Printing Technologies—A Comparative Case Study*., in The Decentralized and Networked Future of Value Creation, J.-P. Ferdinand, U. Petschow, S. Dickel, eds,* Springer International Publishing, Cham, pp. 205–235.

Floyd, E.L., Wang, J., and Regens, J.L. (2017). Fume emissions from a low-cost 3-D printer with various filaments. *J Occup Environ Hyg,* 14(7):523–533.

Foldbjerg, R., Dang, D.A., and Autrup, H. (2011). Cytotoxicity and genotoxicity of silver nanoparticles in the human lung cancer cell line, A549. *Arch Toxicol,* 85(7):743–750.

Frampton, M.W., Stewart, J.C., Oberdörster, G., Morrow, P.E., Chalupa, D., Pietropaoli, A.P., Frasier, L.M., Speers, D.M., Cox, C., Huang, L.S., and Utell, M.J. (2006). Inhalation of ultrafine particles alters blood leukocyte expression of adhesion molecules in humans. *Environ Health Perspect,* 114:51–58.

Frenklach, M. and Harris, S.J. (1986). Aerosol dynamics modeling using the method of moments. *J Colloid Interf Sci,* 118(1):252–261.

Friedlander, S.K. (2000). Smoke, Dust and Haze: Fundamentals of Aerosol Dynamics. Oxford University Press, New York, New York.

Fromme, H. (2012). Particles in the Indoor Environment. INTECH Open Access Publisher. http://www.intechopen.com/source/pdfs/30050/InTech-Particles_in_the_indoor_environment.pdf.

Gao, D., Fang, T., Verma, V., Zeng, L., and Weber, R.J. (2017). A method for measuring total aerosol oxidative potential (OP) with the dithiothreitol (DTT) assay and comparisons between an urban and roadside site of water-soluble and total OP. *Atmos Meas Tech,* 10(8):2821–2835.

Géhin, E., Ramalho, O., and Kirchner, S. (2008). Size distribution and emission rate measurement of fine and ultrafine particle from indoor human activities. *Atmos Environ,* 42(35):8341–8352.

George, T.C., Fanning, S.L., Fitzgeral-Bocarsly, P., Medeiros, R.B., Highfill, S., Shimizu, Y., Hall, B.E., Frost, K., Basiji, D., Ortyn, W.E., Morrissey, P.J., and Lynch, D.H. (2006). Quantitative measurement of nuclear translocation events using similarity analysis of multispectral cellular images obtained in flow. *J Immunol Methods,* 311(1–2):117–129.

Gibson, I., Rosen, D.W., and Stucker, B. (2010). Additive Manufacturing Technologies. Springer US, Boston, MA.

Godish, T. (2001). Aldehydes, in *Indoor Air Quality Handbook*, J. D. Spengler, J. M. Samet, and J. F. McCarthy, eds, McGRAW-HILL, AccessEngineering.

Grass, R.N., Limbach, L.K., Athanassiou, E.K., and Stark, W.J. (2010). Exposure of aerosols and nanoparticle dispersions to in vitro cell cultures: A review on the dose relevance of size, mass, surface and concentration. *J Aerosol Sci,* 41(12):1123–1142.

Grommes, J. and Soehnlein, O. (2011). Contribution of Neutrophils to Acute Lung Injury. *Mol Med,* 17(3–4):293–307.

Gümperlein, I., Fischer, E., Dietrich-Gümperlein, G., Karrasch, S., Nowak, D., Jörres, R.A., and Schierl, R. (2018). Acute health effects of desktop 3D printing (FDM) using ABS and PLA materials: an experimental exposure study in human volunteers. *Indoor Air*.

Guo, H., Lee, S.., Chan, L.., and Li, W. (2004). Risk assessment of exposure to volatile organic compounds in different indoor environments. *Environ Res,* 94(1):57–66.

Happo, M.S., Salonen, R.O., Hälinen, A.I., Jalava, P.I., Pennanen, A.S., Dormans, J.A.M.A., Gerlofs-Nijland, M.E., Cassee, F.R., Kosma, V.-M., Sillanpää, M., Hillamo, R., and Hirvonen, M.-R. (2010). Inflammation and tissue damage in mouse lung by single and repeated dosing of urban air coarse and fine particles collected from six European cities. *Inhal Toxicol,* 22(5):402–416.

Harbeck, R.J. (1998). Immunophenotyping of Bronchoalveolar Lavage Lymphocytes. *Clin Diagn Lab Immunol,* 5(3):271–277.

Harrop, J. (2015). Applications of 3D Printing 2014-2024: Forecasts, Markets, Players: IDTechEx. Available at http://www.idtechex.com/research/reports/applications-of-3d-printing-2014-2024-forecasts-markets-players-000385.asp (Accessed 15 June 2016).

He, C., Morawska, L., and Taplin, L. (2007). Particle Emission Characteristics of Office Printers. *Environ Sci Technol,* 41(17):6039–6045.

Hedge, A. (2009). Indoor Air Quality, Health and Productivity, in *Indoor Work and Living Environments*, R. G. Harris and D. P. Moore, eds, Nova Science Publishers, Inc., 247–262.

Hinds, W.C. (1999). Aerosol technology: properties, behavior, and measurement of airborne particles, 2nd ed. ed. John Wiley & Sons, New York.

Horvath, J. (2014). A Brief History of 3D Printing*., in Mastering 3D Printing,* Apress, Berkeley, CA, pp. 3–10.

House, R., Rajaram, N., and Tarlo, S.M. (2017). Case report of asthma associated with 3D printing. *Occup Med (Lond),* 67(8):652–654.

Hulburt, H.M. and Katz, S. (1964). Some problems in particle technology: A statistical mechanical formulation. *Chem Eng Sci,* 19(8):555–574.

Hussain, S., Boland, S., Baeza-Squiban, A., Hamel, R., Thomassen, L.C.J., Martens, J.A., Billon-Galland, M.A., Fleury-Feith, J., Moisan, F., Pairon, J.-C., and Marano, F. (2009). Oxidative stress and proinflammatory effects of carbon black and titanium

dioxide nanoparticles: Role of particle surface area and internalized amount. *Toxicology,* 260(1–3):142–149.

Izdebska, J. and Thomas, S. (2016). Printing on Polymers: Theory and Practice*., in Printing on Polymers: Fundamentals and Applications,* William Andrew, Waltham, MA.

Jamshidian, M., Tehrany, E.A., Imran, M., Jacquot, M., and Desobry, S. (2010). Poly-lactic acid: Production, applications, nanocomposites, and release studies. *Compr Rev Food Sci Food Saf,* 9:552–571.

Johnston, H.J., Hutchison, G., Christensen, F.M., Peters, S., Hankin, S., and Stone, V. (2010a). A review of the in vivo and in vitro toxicity of silver and gold particulates: Particle attributes and biological mechanisms responsible for the observed toxicity. *Crit Rev Toxicol,* 40(4):328–346.

Johnston, H.J., Hutchison, G.R., Christensen, F.M., Peters, S., Hankin, S., Aschberger, K., and Stone, V. (2010b). A critical review of the biological mechanisms underlying the *in vivo* and *in vitro* toxicity of carbon nanotubes: The contribution of physico-chemical characteristics. *Nanotoxicology,* 4(2):207–246.

Karrasch, S., Simon, M., Herbig, B., Langner, J., Seeger, S., Kronseder, A., Peters, S., Dietrich-Gümperlein, G., Schierl, R., Nowak, D., and Jörres, R.A. (2017). Health effects of laser printer emissions: a controlled exposure study. *Indoor Air,* 753–765.

Keenan, C.R., Goth-Goldstein, R., Lucas, D., and Sedlak, D.L. (2009). Oxidative stress induced by zero-valent iron nanoparticles and Fe(II) in human bronchial epithelial cells. *Environ Sci Technol,* 43:4555–4560.

Khatri, M., Bello, D., Gaines, P., Martin, J., Pal, A.K., Gore, R., and Woskie, S. (2013a). Nanoparticles from photocopiers induce oxidative stress and upper respiratory tract inflammation in healthy volunteers. *Nanotoxicology,* 7(5):1014–1027.

Khatri, M., Bello, D., Pal, A.K., Woskie, S., Gassert, T.H., Demokritou, P., and Gaines, P. (2013b). Toxicological effects of $PM_{0.25–2.0}$ particles collected from a photocopy center in three human cell lines. *Inhal Toxicol,* 25(11):621–632.

Kim, Y., Yoon, C., Ham, S., Park, J., Kim, S., Kwon, O., and Tsai, P.-J. (2015). Emissions of Nanoparticles and Gaseous Material from 3D Printer Operation. *Environ Sci Technol,* 49(20):12044–12053.

Klepeis, N.E., Nelson, W.C., Ott, W.R., Robinson, J.P., Tsang, A.M., Switzer, P., Behar, J.V., Hern, S.C., and Engelmann, W.H. (2001). The National Human Activity Pattern Survey (NHAPS): a resource for assessing exposure to environmental pollutants. *J Expo Sci Environ Epidemiol,* 11(3):231–252.

Koivisto, A.J., Hussein, T., Niemelä, R., Tuomi, T., and Hämeri, K. (2010). Impact of particle emissions of new laser printers on modeled office room. *Atmos Environ,* 44(17):2140–2146.

Kommu, S., Khomami, B., and Biswas, P. (2004). Simulation of aerosol dynamics and transport in chemically reacting particulate matter laden flows. Part II: Application to CVD reactors. *Chem Eng Sci,* 59(2):359–371.

Kreiger, M. and Pearce, J.M. (2013). Environmental Impacts of Distributed Manufacturing from 3-D Printing of Polymer Components and Products. *MRS Proceedings,* 1492.

Kroll, A., Pillukat, M.H., Hahn, D., and Schnekenburger, J. (2009). Current in vitro methods in nanoparticle risk assessment: Limitations and challenges. *Eur J Pharm Biopharm,* 72(2):370–377.

Ku, B.K. and Maynard, A.D. (2005). Comparing aerosol surface-area measurements of monodisperse ultrafine silver agglomerates by mobility analysis, transmission electron microscopy and diffusion charging. *J Aerosol Sci,* 36(9):1108–1124.

Lee, B.-J., Kim, B., and Lee, K. (2014). Air Pollution Exposure and Cardiovascular Disease. *Toxicol Res,* 30(2):71–75.

Lee, K.P. and Seidel, W.C. (1991). Pulmonary response to perfluoropolymer fume and particles generated under various exposure conditions. *Fund Appl Toxicol,* 17(2):254–269.

Li, N., Georas, S., Alexis, N., Fritz, P., Xia, T., Williams, M.A., Horner, E., and Nel, A. (2016). A work group report on ultrafine particles (American Academy of Allergy, Asthma & Immunology): Why ambient ultrafine and engineered nanoparticles

should receive special attention for possible adverse health outcomes in human subjects. *J Allergy Clin Immunol,* 138(2):386–396.

Li, N., Sioutas, C., Cho, A., Schmitz, D., Misra, C., Sempf, J., Wang, M., Oberley, T., Froines, J., and Nel, A. (2003). Ultrafine particulate pollutants induce oxidative stress and mitochondrial damage. *Environ Health Perspect,* 111(4):455–460.

Li, N., Xia, T., and Nel, A.E. (2008). The role of oxidative stress in ambient particulate matter-induced lung diseases and its implications in the toxicity of engineered nanoparticles. *Free Radical Bio Med,* 44(9):1689–1699.

Li, R., Kou, X., Geng, H., Xie, J., Yang, Z., Zhang, Y., Cai, Z., and Dong, C. (2015). Effect of Ambient PM $_{2.5}$ on Lung Mitochondrial Damage and Fusion/Fission Gene Expression in Rats. *Chemical Research in Toxicology,* 28(3):408–418.

MatterHackers (2015). 3D Printer Filament Comparison. Available at https://www.matterhackers.com/3d-printer-filament-compare (Accessed 17 June 2016).

McGraw, R. (1997). Description of Aerosol Dynamics by the Quadrature Method of Moments. *Aerosol Sci Tech,* 27(2):255–265.

Moschini, E., Gualtieri, M., Colombo, M., Fascio, U., Camatini, M., and Mantecca, P. (2013). The modality of cell–particle interactions drives the toxicity of nanosized CuO and TiO2 in human alveolar epithelial cells. *Toxicol Lett,* 222(2):102–116.

Nel, A., Xia, T., Mädler, L., and Li, N. (2006). Toxic potential of materials at the nanolevel. *Science,* 311(5761):622–627.

Ng, N.L., Herndon, S.C., Trimborn, A., Canagaratna, M.R., Croteau, P.L., Onasch, T.B., Sueper, D., Worsnop, D.R., Zhang, Q., Sun, Y.L., and Jayne, J.T. (2011). An Aerosol Chemical Speciation Monitor (ACSM) for Routine Monitoring of the Composition and Mass Concentrations of Ambient Aerosol. *Aerosol Sci Tech,* 45(7):780–794.

Ntziachristos, L., Polidori, A., Phuleria, H., Geller, M.D., and Sioutas, C. (2007). Application of a Diffusion Charger for the Measurement of Particle Surface Concentration in Different Environments. *Aerosol Sci Tech,* 41(6):571–580.

Oberdörster, G., Ferin, J., and Lehnert, B.E. (1994). Correlation between particle size, in vivo particle persistence, and lung injury. *Environ Health Perspect,* 102(Suppl 5):173–179.

Oberdörster, G., Finkelstein, J.N., Johnston, C., Gelein, R., Cox, C., Baggs, R., and Elder, A.C. (2000). Acute pulmonary effects of ultrafine particles in rats and mice. *Res Rep Health Eff Inst,* (96):5–74; disc. 75–86.

Oberdörster, G., Oberdörster, E., and Oberdörster, J. (2005). Nanotoxicology: An Emerging Discipline Evolving from Studies of Ultrafine Particles. *Environ Health Persp,* 113(7):823–839.

Ohata, S., Moteki, N., and Kondo, Y. (2011). Evaluation of a Method for Measurement of the Concentration and Size Distribution of Black Carbon Particles Suspended in Rainwater. *Aerosol Sci Tech,* 45(11):1326–1336.

Pankow, J.F., Seinfeld, J.H., Asher, W.E., and Erdakos, G.B. (2001). Modeling the Formation of Secondary Organic Aerosol. 1. Application of Theoretical Principles to Measurements Obtained in the α-Pinene/, β-Pinene/, Sabinene/, Δ^3 -Carene/, and Cyclohexene/Ozone Systems. *Environ Sci Technol,* 35(6):1164–1172.

Pardo, M., Porat, Z., Rudich, A., Schauer, J.J., and Rudich, Y. (2016). Repeated exposures to roadside particulate matter extracts suppresses pulmonary defense mechanisms, resulting in lipid and protein oxidative damage. *Environ Pollut,* 210:227–237.

Pardo, M., Shafer, M.M., Rudich, A., Schauer, J.J., and Rudich, Y. (2015). Single Exposure to near Roadway Particulate Matter Leads to Confined Inflammatory and Defense Responses: Possible Role of Metals. *Environ Sci Technol,* 49(14):8777–8785.

Pardo, M., Shuster-Meiseles, T., Levin-Zaidman, S., Rudich, A., and Rudich, Y. (2014). Low Cytotoxicity of Inorganic Nanotubes and Fullerene-Like Nanostructures in Human Bronchial Epithelial Cells: Relation to Inflammatory Gene Induction and Antioxidant Response. *Environ Sci Technol,* 48(6):3457–3466.

Pardo, M. and Tirosh, O. (2009). Protective signalling effect of manganese superoxide dismutase in hypoxia-reoxygenation of hepatocytes. *Free Radical Res,* 43(12):1225–1239.

Peixoto, M.S., de Oliveira Galvão, M.F., and Batistuzzo de Medeiros, S.R. (2017). Cell death pathways of particulate matter toxicity. *Chemosphere,* 188:32–48.

Perrone, M.G., Gualtieri, M., Consonni, V., Ferrero, L., Sangiorgi, G., Longhin, E., Ballabio, D., Bolzacchini, E., and Camatini, M. (2013). Particle size, chemical composition, seasons of the year and urban, rural or remote site origins as determinants of biological effects of particulate matter on pulmonary cells. *Environ Pollut,* 176:215–227.

Pirela, S., Molina, R., Watson, C., Cohen, J., Bello, D., Demokritou, P., and Brain, J. (2013). Effects of copy center particles on the lungs: A toxicological characterization using a Balb/c mice model. *Inhal Toxicol,* 25(9):498–508.

Pirela, S.V., Miousse, I.R., Lu, X., Castranova, V., Thomas, T., Qian, Y., Bello, D., Kobzik, L., Koturbash, I., and Demokritou, P. (2016). Effects of Laser Printer–Emitted Engineered Nanoparticles on Cytotoxicity, Chemokine Expression, Reactive Oxygen Species, DNA Methylation, and DNA Damage: A Comprehensive in Vitro Analysis in Human Small Airway Epithelial Cells, Macrophages, and Lymphoblasts. *Environ Health Persp,* 124(2):210–219.

Pirela, S.V., Pyrgiotakis, G., Bello, D., Thomas, T., Castranova, V., and Demokritou, P. (2014). Development and characterization of an exposure platform suitable for physico-chemical, morphological and toxicological characterization of printer-emitted particles (PEPs). *Inhal Toxicol,* 26(7):400–408.

Pratsinis, S.E. (1988). Simultaneous Nucleation, Condensation, and Coagulation in Aerosol Reactors. *J Colloid Interf Sci,* 124(2):416–427.

Pratsinis, S.E., Kodas, T.T., Dudukovic, M.P., and Friedlander, S.K. (1986). Aerosol Reactor Design: Effect of Reactor Type and Process Parameters on Product Aerosol Characteristics. *Ind Eng Chem Proc DD,* 25(3):634–642.

Ragan, S. (2013). Plastics for 3D Printing. *MAKE: Ultimate Guide to 3D Printing,* 22.

Randolph, A.D. and Larson, M.A. (1971). Theory of Particulate Processes. Academic Press, New York, New York.

Rumchev, K. (2004). Association of domestic exposure to volatile organic compounds with asthma in young children. *Thorax,* 59(9):746–751.

Rutkowski, J.V. and Levin, B.C. (1986). Acrylonitrile–butadiene–styrene copolymers (ABS): Pyrolysis and combustion products and their toxicity—a review of the literature. *Fire Mater,* 10(3–4):93–105.

Salthammer, T., Schripp, T., Uhde, E., and Wensing, M. (2012). Aerosols generated by hardcopy devices and other electrical appliances. *Environ Pollut,* 169:167–174.

Salvi and Holgate (1999). Mechanisms of particulate matter toxicity. *Clin Exp Allergy,* 29(9):1187–1194.

Sauvain, J.-J., Rossi, M.J., and Riediker, M. (2013). Comparison of Three Acellular Tests for Assessing the Oxidation Potential of Nanomaterials. *Aerosol Sci Tech,* 47(2):218–227.

Sayes, C.M., Reed, K.L., and Warheit, D.B. (2007). Assessing Toxicity of Fine and Nanoparticles: Comparing In Vitro Measurements to In Vivo Pulmonary Toxicity Profiles. *Toxicol Sci,* 97(1):163–180.

Schripp, T., Wensing, M., Uhde, E., Salthammer, T., He, C., and Morawska, L. (2008). Evaluation of Ultrafine Particle Emissions from Laser Printers Using Emission Test Chambers. *Environ Sci Technol,* 42(12):4338–4343.

Schweizer, C., Edwards, R.D., Bayer-Oglesby, L., Gauderman, W.J., Ilacqua, V., Juhani Jantunen, M., Lai, H.K., Nieuwenhuijsen, M., and Künzli, N. (2007). Indoor time–microenvironment–activity patterns in seven regions of Europe. *J Expo Sci Environ Epidemiol,* 17(2):170–181.

Scungio, M., Vitanza, T., Stabile, L., Buonanno, G., and Morawska, L. (2017). Characterization of particle emission from laser printers. *Sci Total Environ,* 586:623–630.

Seeger, S., Brodner, D., Jacobi, T., Rasch, F., Rothhardt, M., and Wilke, O. (2018). Emissions of fine and ultrafine particles and volatile organic compounds from different filament materials operated on a low-cost 3D printer. *Gefahrstoffe Reinhaltung der Luft*, 3:79–87.

Seidel, W.C., Scherer Jr, K.V., Cline Jr, D., Olson, A.H., Bonesteel, J.K., Church, D.F., Nuggehalli, S., and Pryor, W.A. (1991). Chemical, physical, and toxicological characterization of fumes produced by heating tetrafluoroethene homopolymer

and its copolymers with hexafluoropropene and perfluoro (propyl vinyl ether). *Chem Res Toxicol,* 4(2):229–236.

Seigneur, C., Hudischewskyj, A.B., Seinfeld, J.H., Whitby, K.T., Whitby, E.R., Brock, J.R., and Barnes, H.M. (1986). Simulation of Aerosol Dynamics: A Comparative Review of Mathematical Models. *Aerosol Sci Tech,* 5(2):205–222.

Seinfeld, J.H., Erdakos, G.B., Asher, W.E., and Pankow, J.F. (2001). Modeling the formation of secondary organic aerosol (SOA). 2. The predicted effects of relative humidity on aerosol formation in the α-pinene-, β-pinene-, sabinene-, Δ3-carene-, and cyclohexene-ozone systems. *Environ Sci Technol,* 35(9):1806–1817.

Sethi, V. and Biswas, P. (1990). Modeling of Particle Formation and Dynamics in a Flame Incinerator. *J Air Waste Manage Assoc,* 40(1):42–46.

Shi, J.P., Harrison, R.M., and Brear, F. (1999). Particle size distribution from a modern heavy duty diesel engine. *Sci Total Environ,* 235(1–3):305–317.

Shiraiwa, M., Ueda, K., Pozzer, A., Lammel, G., Kampf, C.J., Fushimi, A., Enami, S., Arangio, A.M., Fröhlich-Nowoisky, J., Fujitani, Y., Furuyama, A., Lakey, P.S.J., Lelieveld, J., Lucas, K., Morino, Y., Pöschl, U., Takahama, S., Takami, A., Tong, H., Weber, B., Yoshino, A., and Sato, K. (2017). Aerosol Health Effects from Molecular to Global Scales. *Environ Sci Technol,* 51(23):13545–13567.

Stabile, L., Scungio, M., Buonanno, G., Arpino, F., and Ficco, G. (2017). Airborne particle emission of a commercial 3D printer: the effect of filament material and printing temperature. *Indoor Air,* 27(2):398–408.

Stefaniak, A.B., LeBouf, R.F., Duling, M.G., Yi, J., Abukabda, A.B., McBride, C.R., and Nurkiewicz, T.R. (2017a). Inhalation exposure to three-dimensional printer emissions stimulates acute hypertension and microvascular dysfunction. *Toxicol Appl Pharmacol,* 335:1–5.

Stefaniak, A.B., LeBouf, R.F., Yi, J., Ham, J., Nurkewicz, T., Schwegler-Berry, D.E., Chen, B.T., Wells, J.R., Duling, M.G., Lawrence, R.B., Martin, S.B., Johnson, A.R., and Virji, M.A. (2017b). Characterization of chemical contaminants generated by a desktop fused deposition modeling 3-dimensional Printer. *J Occup Environ Hyg,* 14(7):540–550.

Stein, S. E. "Mass Spectra" in *NIST Chemistry WebBook*, NIST Standard Reference Database Number 69, Eds. P. J. Linstrom and W. G. Mallard, Gaithersburg, MD 20899: National Institute of Standards and Technology. doi:10.18434/T4D303, (retrieved January 15, 2016).

Steinle, P. (2016). Characterization of emissions from a desktop 3D printer and indoor air measurements in office settings. *J Occup Environ Hyg,* 13(2):121–132.

Stephens, B., Azimi, P., El Orch, Z., and Ramos, T. (2013). Ultrafine particle emissions from desktop 3D printers. *Atmos Environ,* 79:334–339.

Sutherland, W. (1893). LII. *The viscosity of gases and molecular force*. *Philos Mag Series 5,* 36(223):507–531.

Tao, Y. and McMurry, P.H. (1989). Vapor pressures and surface free energies of C14-C18 monocarboxylic acids and C5 and C6 dicarboxylic acids. *Environ Sci Technol,* 23(12):1519–1523.

Thorley, A.J., Ruenraroengsak, P., Potter, T.E., and Tetley, T.D. (2014). Critical Determinants of Uptake and Translocation of Nanoparticles by the Human Pulmonary Alveolar Epithelium. *ACS Nano,* 8(11):11778–11789.

Tobias, H.J. and Ziemann, P.J. (2000). Thermal Desorption Mass Spectrometric Analysis of Organic Aerosol Formed from Reactions of 1-Tetradecene and O_3 in the Presence of Alcohols and Carboxylic Acids. *Environ Sci Technol,* 34(11):2105–2115.

Tsang, T.H., Cook, S.M., and Marra, M.E. (1990). Dynamic Behavior of Condensation and Evaporation of Polydisperse Volatile Aerosols. *Aerosol Sci Tech,* 12(2):386–398.

Tucker, W.G. (2001). Volatile Organic Compounds, in *Indoor Air Quality Handbook*, J. D. Spengler, J. M. Samet, and J. F. McCarthy, eds, McGRAW-HILL, AccessEngineering.

Uhde, E., He, C., and Wensing, M. (2006). Characterization of ultra-fine particle emission from a laser printer*., in Proc. Int. Conf. Healthy Building,* Citeseer, pp. 479–482.

UL. (2014). UL 2823, UL GREENGUARD Certification Program Method for Measuring and Evaluating Chemical and Particle Emissions from Electronic Equipment Using Dynamic Environmental Chambers. Northbrook, IL: Underwriters Laboratories.

Unwin, J., Coldwell, M.R., Keen, C., and McAlinden, J.J. (2013). Airborne Emissions of Carcinogens and Respiratory Sensitizers during Thermal Processing of Plastics. *Annals of Occup Hyg,* 57(3):399–406.

U. S. EPA. (2000). National Air Toxics Program: The Integrated Urban Strategy, Report to Congress. Office of Air Quality Planning and Standards. Research Triangle Park, NC: U. S. Environmental Protection Agency.

U. S. EPA. (1988). Health and Environmental Effects Profile for Caprolactam. ECAO-CIN-G018. Environmental Criteria and Assessment Office, Office of Health and Environmental Assessment, Office of Research and Development. Cincinnati, OH: U. S. Environmental Protection Agency.

Vance, M. E., Pegues, V., Van Montfrans, S., Leng, W., and Marr, L.C. (2017). Aerosol Emissions from Fuse-Deposition Modeling 3D Printers in a Chamber and in Real Indoor Environments. *Environ Sci Technol,* 51(17):9516–9523.

Verma, V., Fang, T., Xu, L., Peltier, R.E., Russell, A.G., Ng, N.L., and Weber, R.J. (2015). Organic Aerosols Associated with the Generation of Reactive Oxygen Species (ROS) by Water-Soluble $PM_{2.5}$. *Environ Sci Technol,* 49(7):4646–4656.

Wallace, L.A. (2001). Assessing Human Exposure to Volatile Organic Compounds, in *Indoor Air Quality Handbook*, J. D. Spengler, J. M. Samet, and J. F. McCarthy, eds, McGRAW-HILL, AccessEngineering.

Wang, Z.-M. and Biswas, P. (2000). Nickel Speciation and Aerosol Formation During Combustion of Kerosene Doped with Nickel Nitrate Aerosol in a Premixed Burner. *Aerosol Sci Tech,* 33(6):525–535.

Warheit, D.B., Seidel, W.C., Carakostas, M.C., and Hartsky, M.A. (1990). Attenuation of perfluoropolymer fume pulmonary toxicity: Effect of filters, combustion method, and aerosol age. *Exp Mol Pathol,* 52(3):309–329.

Warren, D.R. and Seinfeld, J.H. (1984). Nucleation and Growth of Aerosol From a Continuously Reinforced Vapor. *Aerosol Sci Tech,* 3(2):135–153.

Wensing, M., Schripp, T., Uhde, E., and Salthammer, T. (2008). Ultra-fine particles release from hardcopy devices: Sources, real-room measurements and efficiency of filter accessories. *Sci Total Environ,* 407(1):418–427.

Whitby, E.R. and McMurry, P.H. (1997). Modal Aerosol Dynamics Modeling. *Aerosol Sci Tech,* 27(6):673–688.

Wojtyła, S., Klama, P., and Baran, T. (2017). Is 3D printing safe? Analysis of the thermal treatment of thermoplastics: ABS, PLA, PET, and nylon. *J Occup Environ Hyg,* 14(6):D80–D85.

Wu, C.-Y. and Biswas, P. (2000). Lead species aerosol formation and growth in multicomponent high-temperature environments. *Environ Eng Sci,* 17(1):41–60.

Wu, Y., Eichler, C.M.A., Chen, S., and Little, J.C. (2016). Simple Method To Measure the Vapor Pressure of Phthalates and Their Alternatives. *Environ Sci Technol,* 50(18):10082–10088.

Xia, T., Zhu, Y., Mu, L., Zhang, Z.-F., and Liu, S. (2016). Pulmonary diseases induced by ambient ultrafine and engineered nanoparticles in twenty-first century. *Natl Sci Rev,* 3:416–429.

Xu, L., Guo, H., Weber, R.J., and Ng, N.L. (2017). Chemical Characterization of Water-Soluble Organic Aerosol in Contrasting Rural and Urban Environments in the Southeastern United States. *Environ Sci Technol,* 51(1):78–88.

Yi, J., LeBouf, R.F., Duling, M.G., Nurkiewicz, T., Chen, B.T., Schwegler-Berry, D., Virji, M.A., and Stefaniak, A.B. (2016). Emission of particulate matter from a desktop three-dimensional (3D) printer. *J Toxicol Environ Health Part A,* 79(11):453–465.

Yoon, H.I., Hong, Y.-C., Cho, S.-H., Kim, H., Kim, Y.H., Sohn, J.R., Kwon, M., Park, S.-H., Cho, M.-H., and Cheong, H.-K. (2010). Exposure to volatile organic compounds and loss of pulmonary function in the elderly. *Eur Respir J,* 36(6):1270–1276.

Yu, M., Lin, J., and Chan, T. (2008). A New Moment Method for Solving the Coagulation Equation for Particles in Brownian Motion. *Aerosol Sci Tech,* 42(9):705–713.

Yu, M. and Liu, Y. (2016). Methods of Moments for Resolving Aerosol Dynamics*., in Aerosols - Science and Case Studies, K. Volkov, ed,* InTech.

Zelenyuk, A., Cai, Y., and Imre, D. (2006). From Agglomerates of Spheres to Irregularly Shaped Particles: Determination of Dynamic Shape Factors from Measurements of Mobility and Vacuum Aerodynamic Diameters. *Aerosol Sci Tech,* 40(3):197–217.

Zhang, Q., Kusaka, Y., Zhu, X., Sato, K., Mo, Y., Kluz, T., and Donaldson, K. (2003). Comparative Toxicity of Standard Nickel and Ultrafine Nickel in Lung after Intratracheal Instillation. *J Occup Health,* 45:23–30.

Zhang, Q., Sharma, G., Wong, J.P.S., Davis, A.Y., Black, M.S., Biswas, P., and Weber, R.J. (2018). Investigating particle emissions and aerosol dynamics from a consumer fused deposition modeling 3D printer with a lognormal moment aerosol model. *Aerosol Sci Tech*.

Zhang, Q., Wong, J.P.S., Davis, A.Y., Black, M.S., and Weber, R.J. (2017). Characterization of particle emissions from consumer fused deposition modeling 3D printers. *Aerosol Sci Tech,* 51(11):1275–1286.

Zhou, Y., Kong, X., Chen, A., and Cao, S. (2015). Investigation of Ultrafine Particle Emissions of Desktop 3D Printers in the Clean Room. *Procedia Engineering,* 121:506–512.

Zontek, T.L., Ogle, B.R., Jankovic, J.T., and Hollenbeck, S.M. (2017). An exposure assessment of desktop 3D printing. *J Chem Health Saf,* 24(2):15–25.

Zukas, V. and Zukas, J.A. (2015). An Introduction to 3D Printing. First Edition Design Publishing, Sarasota, FL.